Development of a Heat Transfer Model of a Simplified Build Environment in Electron Beam Additive Manufacturing

by

Farhad Rahimi

B.Sc., Iran University of Science and Technology, 2014

A THESIS SUBMITTED IN PARTIAL FULFILLMENT OF

THE REQUIREMENTS FOR THE DEGREE OF

MASTER OF APPLIED SCIENCE

in

THE FACULTY OF GRADUATE AND POSTDOCTORAL STUDIES

(Materials Engineering)

THE UNIVERSITY OF BRITISH COLUMBIA

(Vancouver)

April 2022

The following individuals certify that they have read, and recommend to the Faculty of Graduate and Postdoctoral Studies for acceptance, the thesis entitled:

Development of a Heat Transfer Model of a Simplified Build Environment in Electron Beam Additive Manufacturing

submitted by Farhad Rahimi in partial fulfillment of the requirements for

the degree of Master of Applied Science

in Materials Engineering

Examining Committee:

Steve Cockcroft, Professor, Materials Engineering, UBC

Supervisor

Farzaneh Farhang Mehr, Director of Additive Manufacturing, Materials Engineering, UBC

Supervisory Committee Member

Daan Maijer, Professor, Materials Engineering, UBC

Supervisory Committee Member

Warren Poole, Professor, Materials Engineering, UBC

Supervisory Committee Member

Abstract

In this research, a 3D heat transfer model incorporating cavity radiation was developed in ABAQUS version 2017 to approximate the thermal field within the build environment in an Electron Beam Powder Bed Fusion (EB-PBF) Additive Manufacturing (AM) Process. The build environment, also referred to as the "pseudo build environment, was fabricated in an Electron Beam Button Furnace (EB-BF) using an ARCAM Q20Plus heat shield (with the top section removed). The “build plate” was fabricated from a commercially pure titanium disk, which was surrounded by a stainless-steel plate. A circular beam pattern with a diameter of 50 mm was used to heat the titanium disk in the absence of powder. The experimental set-up was instrumented with type-K thermocouples to record the evolution in temperature on the heat shield walls, within the titanium disk and stainless-steel plate during the experiment. To record and store the temperature, an autonomous data acquisition system was developed for in-situ instrumentation within a vacuum environment. The model was validated with respect to the temperature data extracted from the EB-BF.

Overall, the results of the heating experiment and the numerical model suggest that the radiative heat exchange between various surfaces within the build environment is complex. The model results indicate that the portion of heat transferred via cavity radiation and absorbed by the heat shield walls was found to be a strong function of the titanium disk temperature. Additionally, four simple numerical case studies were developed to evaluate the effect of heating pattern, initial preheat, the heat absorption by the powder deposition sequence and post powder deposition preheat on the thermal behaviour in the pseudo build environment. The results of the numerical cases provide guidance into future model development, which can potentially aid in better understanding the heat transfer within the build environment leading to better AM process control.

Lay Summary

Electron Beam Powder Bed Fusion (EB-PBF) additive manufacturing systems utilize a stream of high-energy electrons to melt-sinter a source material into a near-net-shape part in a layer-by-layer fashion. It is argued that developing and validating numerical models can aid to understand the heat transfer within the build environment during the process and potentially identify a suitable set of process parameters. This research work focuses on developing and validating a numerical model aimed at predicting the evolution of the thermal field within a simplified build environment during a heating experiment. Additionally, an in-situ temperature measurement system capable of working in a vacuum environment was developed to record the evolution of temperature from the experimental set-up to provide temperature data for model validation. Overall, the results showed that the model predictions help identify the key elements in the transport of heat during a simple heating experiment. Furthermore, the developed data acquisition system has the potential to be implemented in a high-vacuum environment for in-situ measurements.

Preface

The present M.A.Sc. thesis is an original work by the author, Farhad Rahimi, which is presented in the form of two manuscripts. The first manuscript (Chapter 4) presents a simplified approach to modelling the thermal balance of a pseudo build environment in electron beam additive manufacturing. The second manuscript (Chapter 5) presents the design and development of an autonomous data acquisition system for in-situ temperature measurement within a high-vacuum environment.

In Chapter 4 (manuscript 1), I designed an experimental set-up that represents a simplified build environment of an Electron Beam Additive Manufacturing (EB-AM) machine. The set-up, referred to as the "pseudo build environment", was constructed within a lab-scale Electron Beam Button Furnace (EB-BF) by incorporating a simplified GE-ARCAM Q20plus heat shield (i.e., the heat shield without the top plate). The EB-BF system was chosen as it provides good access to the vacuum chamber for instrumentation and a basic gun control system for prescribing a simple beam trajectory (pattern) in comparison to a commercial EB-AM system. The pseudo build environment was instrumented with thermocouples to record the evolution of temperature during heating and cooling of a commercially pure titanium disk in the absence of powder. In addition, I developed a 3D heat transfer model in ABAQUS to predict the evolution of the macro thermal field within the experimental set-up. The model is validated against temperature measurements obtained from the pseudo build environment during heating and cooling.

In Chapter 5 (manuscript 2), I developed an autonomous in-situ temperature measurement system that can be implemented in a high-vacuum environment for in-situ instrumentation. For this purpose, a preliminary temperature measurement system based on the Arduino Uno development board was developed and evaluated, as discussed in great detail in Appendix A.

Identifying the limitations of the initial prototype aided in developing a modular and autonomous in-situ temperature measurement and logging system. Furthermore, a hermetic enclosure was designed to protect the electronic elements of the system from the high-vacuum environment. This is mainly related to issues with heat dissipation from the electronics in a vacuum environment and the air pressure range required by the battery to operate safely. Appendix B presents the design procedure of the hermetic enclosure in greater detail. Finally, I designed a series of experiments to evaluate the system's performance and functionality.

Throughout the course of this program, Professor Steve Cockcroft and Dr. Farzaneh Farhang Mehr, my supervisors, provided support in the form of advice and comments on all aspects of my M.A.Sc. program, including but not limited to the design and execution of experiments, data analysis, model development and the writing of publications and this dissertation. Dr. Jun Ou supported the program by providing training on the lab-scale electron beam button furnace and the experimental facility and recommendations on the temperature measurement with thermocouples.

Table of Contents

List of Tables

List of Figures

List of Symbols

Symbol	Description	Unit
a_n	Thermocouple type-dependent polynomial coefficient	-
A_{disk}	Surface area for the CP-Ti disk	m^2
A_i	Areas of facet *i*	m^2
A_j	Areas of facet *j*	m^2
A_{P_i}	Surface area for pattern P_i	m^2
c_p	Specific heat of solid Ti6Al4V	J kg^{-1} K^{-1}
E_{P_i}	Surface energy density for pattern P_i	J m^{-2}
F_{ij}	View factor	m^4 m^{-4}
G	Gain value	-
h	Powder layer thickness	m
$h_{interface}$	Interfacial heat transfer coefficient	W m^{-2} K^{-1}
H_{PD}	Enthalpy associated with powder deposition for each layer	J
n	Order of the polynomial function	-
O_{ADC}	ADC output	-
P_{EB}	Electron beam power	W
$q_{contact}$	Heat flux across the interface	W m^{-2}
$\bar{q}_{EB}$	Time-averaged Gaussian surface heat flux	W m^{-2}
q_i	Radiation flux into the facet *i* in a cavity	W m^{-2}
q_{PD}	Surface heat flux associated with powder deposition sequence	W m^{-2}
q_{PH_i}	Uniform surface heat flux associated with preheating sequence *i*	W m^{-2}
q_{rad}	Radiative heat flux	W m^{-2}
r	RTD resistance when the temperature is less than 0 °C	Ω
R	Distance from the centre of the CP-Ti disk	m
R_0	Radius of the beam trajectory pattern	m
$R5$	Reference resistor	Ω
R_d	CP-Ti disk radius	m
r_{ij}	Distance between facets *i* and *j*	m
R_{RTD0}	RTD resistance at 0 °C	Ω
Symbol	**Description**	**Unit**

R_{RTD}	RTD resistance at any temperature	Ω
R_T	Percent of relative change in the temperature	-
T	Surface temperature of the radiating object	K
T_{amb}	Ambient temperature of the vacuum chamber walls	K
$T_{A/B}$	Surface temperatures at the two sides of the interface	K
T_{BM}	Temperature data for the base model	°C
T_C	Temperature data for each sensitivity case study	°C
$\bar{T}_{disk}$	CP-Ti disk average surface temperature	K
T_i	Temperatures of facets *i*	K
T_j	Temperatures of facets *j*	K
T_{powder}	Initial powder layer temperature	K
t_{P_i}	Beam irradiation time for pattern P_i	s
t_{PD}	Duration of the powder deposition sequence	s
V_{CJ}	Thermoelectric cold junction voltage	μV
V_{TC}	Final voltage value for the thermocouple channel	μV
$V_{TC.read}$	Voltage value measured at the thermocouple channel	μV
σ	Stefan-Boltzmann constant	W m^{-2} K^{-4}
σ_{EB}	Standard deviation of the Gaussian function	m
δ_{kj}	Kronecker delta	-
ε_i	Emissivity of facet *i*	-
ε_j	Emissivity of facet *j*	-
η	Electron beam absorption factor	-
φ	Powder packing factor	-
ρ_s	Density of solid Ti6Al4V	kg m^{-3}

List of Abbreviations

AM	Additive Manufacturing
ADC	Analogue-to-Digital Convertor
AITML	Autonomous In-situ Temperature Measurement and Logging
ASTM	American Society for Testing and Materials
CAD	Computer-Aided Design
CJC	Cold Junction Compensation
CP-Ti	Commercially Pure Titanium
EB	Electron Beam
EB-AM	Electron Beam Additive Manufacturing
EB-BF	Electron Beam Button Furnace
EB-PBF	Electron Beam Powder Bed Fusion
EBW	Electron Beam Welding
FE	Finite Element
GE	General Electric
IDE	Integrated Development Environment
IHTC	Interfacial Heat Transfer Coefficient
IR	Infrared
LiPO	Lithium-ion Polymer
NIST	National Institute of Standards and Technology
PB	Powder Bed
PD	Powder Deposition
PH	Preheat
PRS	Powder Recovery System
PTMS	Preliminary Temperature Measurement System
RTC	Real-Time clock
RTD	Resistance Temperature Detector
SS	Stainless Steel
TC	Thermocouple
USB	Universal Serial Bus

Acknowledgements

I would like to thank my supervisors, Professor Steve Cockcroft and Dr. Farzaneh Farhang Mehr, for their support and invaluable insight into developing the research presented in this thesis. Their encouragement and guidance enabled me to produce this work that I am proud to present.

I am extremely grateful to Professor Daan Maijer and Professor Warren Poole, who served on my examining committee, for their valuable time and effort in reviewing this research work.

I would like to thank Dr. Jun Ou and Dr. Carl Reily for their help and support with the electron beam button furnace and their valuable advice on the experimentation. I also offer my sincere gratitude to Ralf Edinger, from Canmora Tech Inc, for valuable advice on developing the electronics and helping with CNC programming and machining of a hermetic enclosure. Especially helpful to me during this time were David Torok, Carl Ng, Wonsang Kim, who provided me with technical support. I appreciate the support I received from the office staff at the Department of Materials Engineering during my stay as a student in the department.

I would also acknowledge the Natural Sciences and Engineering Research Council of Canada (NSERC) for the funding received under the Holistic Innovation in Additive Manufacturing (HI-AM) Network Partnerships Program.

Finally, I would like to thank my parents, my brother, and my friends for their never-ending encouragement, patience, support and profound belief in my abilities.

Dedication

To my parents, my brother, my friends and all my mentors.

Chapter 1: Introduction

Wohlers Associates annual report, published in 2021, showed that the Additive Manufacturing (AM) industry grew by 7.5 percent to approximately $12.8 billion in 2020 despite the pandemic [1]. However, this growth rate is substantially lower than the average annual growth of 25.2 percent in the previous three years and 27.4 percent over the past decade [1,2]. This likely reflects a combination of factors, including the economic downturn and supply chain issues related to the Covid-19 pandemic and the transition in AM capital investment from government and universities to the private sector. This transition, sometimes referred to as the "technological death-valley", is illustrated schematically in Figure 1.1 and is often problematic for new technologies as they move into commercialization.

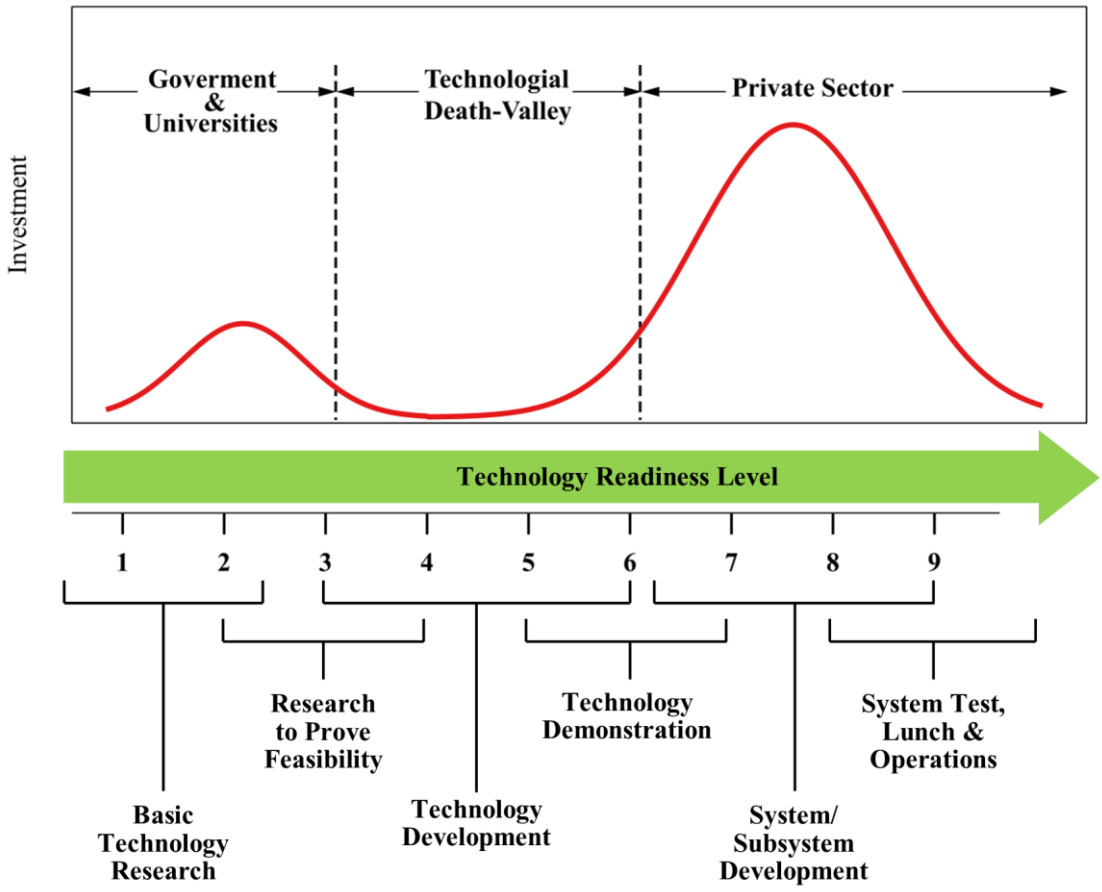

Figure 1.1. Schematic illustration of the technological death-valley for a new-developed technology [3].

While AM technologies offer several advantages over traditional manufacturing technologies, there remain a number of challenges that must be overcome for broader commercial

adoption to occur. Table 1.1 presents some of the key advantages and challenges of AM technologies, as summarized by Ford *et al.* [4]. It should be noted that the two key challenges for AM commercial adoption are cost and productivity since AM processes are slow and the fabrication costs per part are high [5].

Table 1.1. Key advantages and challenges of additive manufacturing processes [4]

Advantages	Challenges
• Small batches of customized products are economically attractive relative to traditional mass-production methods • Direct production from 3D-CAD models means that no tools and moulds are required • Designs in the form of digital files can be easily shared, facilitating the modification and customization of components and products • Novel or complex structures (e.g., free-form, enclosed structures and channels, and lattices) are achievable • low residual porosities in the final part (in electron beam AM processes)	• Production cost and speed • Development and standardization of new materials • Development of multi-material systems • Automation of AM systems and process planning to improve manufacturing efficiency • Post-processing is often required • Support structure materials cannot be recycled, so they need to be minimized • Machine-to-machine variability of process parameters

1.1 Additive Manufacturing Definition

Additive manufacturing includes several manufacturing processes that fabricate components incrementally using a layer-by-layer method [6–8]. The original idea of building parts in a layer-by-layer method was introduced by Kojima [9], and the term "additive manufacturing" has been adopted for these incremental, or layer-wise, manufacturing techniques [6]. This technology allows the manufacturing of complex parts (see Figure 1.2) without the need for extensive moulding and tooling, which facilitates rapid prototyping and more efficient design optimisation [10,11]. It is important to point out that there is typically some post-fabrication machining involved associated with removing the support structure if present. Depending on the end-use application, additional post-processing and finishing operations may also be required – e.g., such as hole drilling, surface finishing, heat treatment, etc. The need for support structure also results in a reduction in material utilization efficiency.

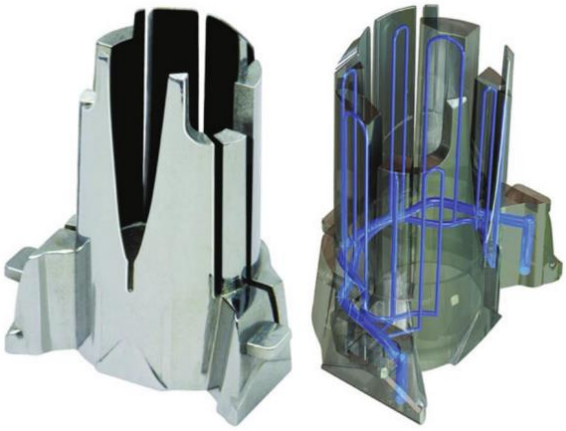

Figure 1.2. A fabricated part and a 3D model, showing complex internal cooling channels in the design [11].

1.2 Additive Manufacturing Applications

Figure 1.3 shows examples of AM industrial applications and commonly used metallic materials. Using AM technology in the industries shown in this figure hinges on economics. Examples of feasible applications are: i) unique component design elements that are difficult to manufacture with conventional methods, ii) the ability to produce prototypes, iii) limited-run parts, iv) the ability to produce replacement parts that are no longer available, and v) medical implants customized to a patient's unique anatomy [10]. The proper guidelines and recommendations for using AM processes are extensively presented in ASTM 52910 [12].

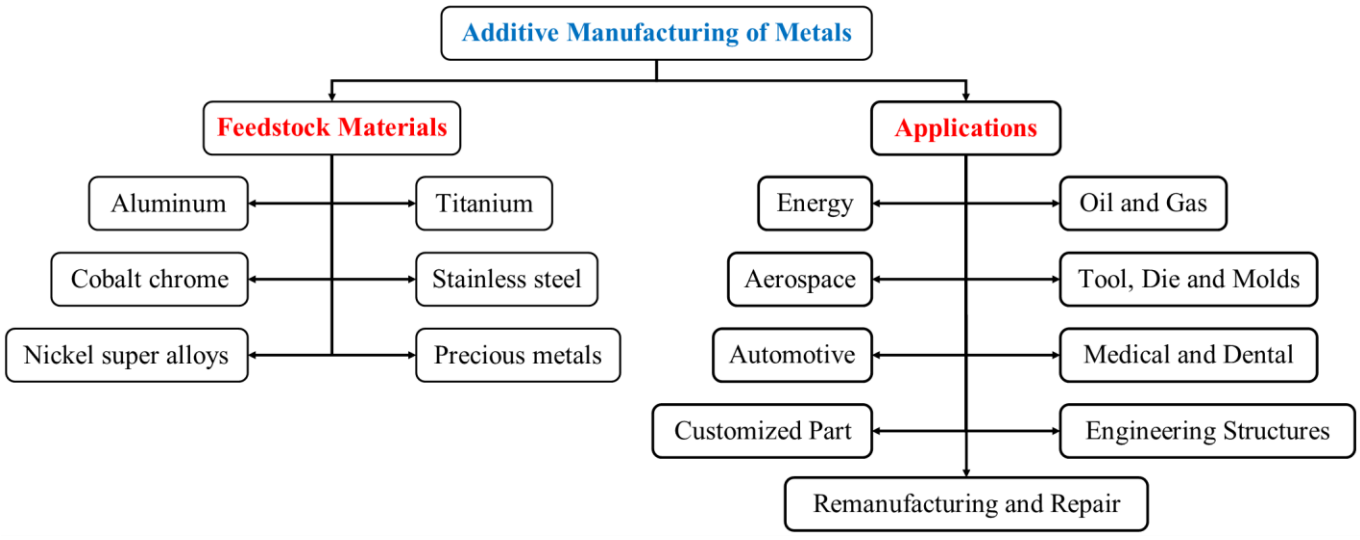

Figure 1.3. Additive manufacturing applications and commonly used metals [10,11].

1.3 Classification of Additive Manufacturing

Technological advancements (e.g., high-performance electronics, cost-effective lasers and electron beam guns, and economical powder materials) have helped to improve performance and reduce the cost of metal AM processes and systems [10]. As shown in Figure 1.4, the key metal AM technologies can be categorized into three groups [12]: i) binder jet printing, ii) directed energy deposition, and iii) powder bed fusion.

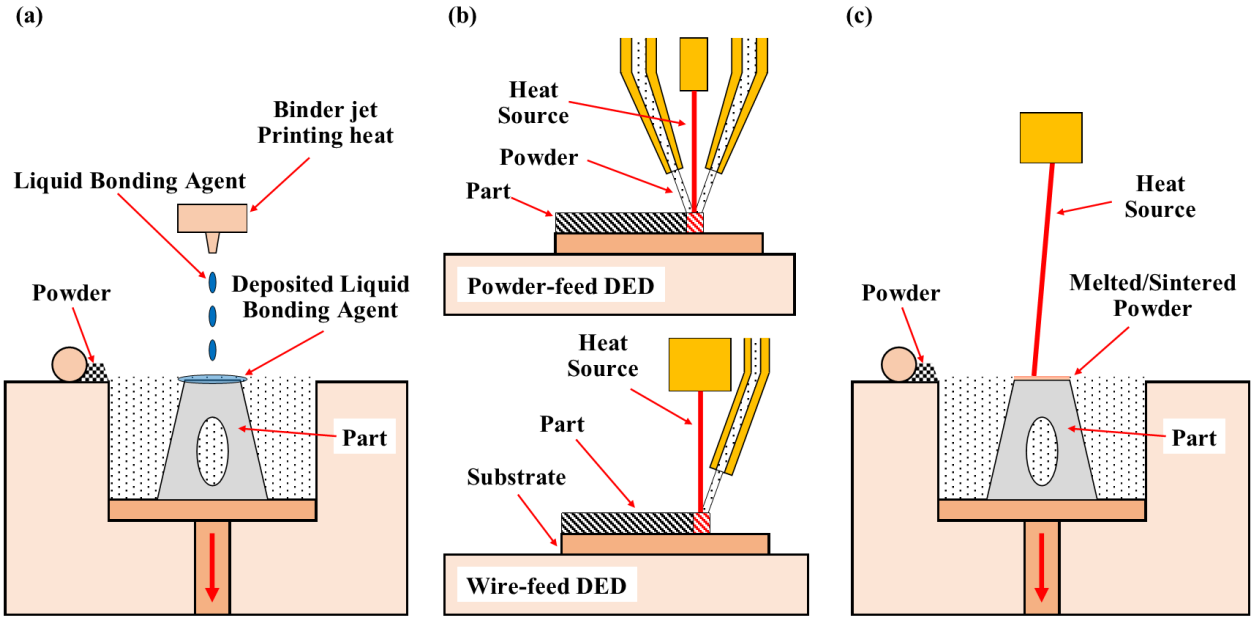

Figure 1.4. Schematics of additive manufacturing classification; (a) binder jet printing, (b) directed energy deposition, and (c) powder bed fusion.

In the direct energy deposition and powder bed fusion technologies, a high-energy-density heat source is used to melt feedstock materials to from near-net-shape parts [11]. The most commonly used heat sources are laser, plasma arc, and electron beam. *Note: other heat sources such as ultrasonic vibration and infrared radiation can be used to melt wire, powder, or even sheet materials and fabricate a component; however, they appear inefficient in industrial applications* [10,13].

Among metal AM technologies, laser and electron beam-based AM systems dominate commercially [11]. The Electron Beam Additive Manufacturing (EB-AM) systems use an electron beam as the heat source to melt-sinter feed material into a near-net-shape part under a high-vacuum environment [10]. To introduce this technology, Chapter 2 will start with a brief history on the birth of electron beam melting and present an overview of the EB-AM process. Some of the defects in the fabricated parts by this technology will also be explored. Additionally, this chapter will briefly discuss several process parameters and their influence on defect formation in a product.

Since the transport of heat in this process is complex, developing numerical models will aid to better understand the heat transfer at both the meso and macro length scales – i.e., at the scale of the melt pool and build environment, and identify the key transport processes affecting build quality. It is suggested that temperature measurements during the build process can be used to validate these numerical models. Chapter 2 will also review several studies attempting in-situ temperature measurement during the EB-AM process.

Toward this goal, Chapter 4 will present the development and validation of a numerical thermal model aimed at predicting the evolution of the macro thermal field within a simplified build environment (i.e., the environment within the heat shield and build platform) constructed within a lab-scale Electron Beam Button Furnace (EB-BF) during a heating experiment. During the experiment, the evolution of temperature is measured from multiple locations within the simplified build environment, and the model is validated with respect to these measurements. Additionally, Chapter 5 will present the development of an autonomous in-situ temperature measurement system used for in-situ temperature measurement within the EB-BF.

Chapter 2: Literature Review

As briefly mentioned in the introduction, this chapter will present a brief history on electron beam melting, an overview of the electron beam additive manufacturing, defects in the fabricated part, process parameters and research contributions toward temperature measurement and model development.

2.1 The Birth of Electron Beam Melting

The first industrial application of Electron Beams (EB) was found by Marcello Pirani [14] in 1907 during a melting experiment with a refractory metal powder. In 1948, Steigerwald [15] developed the basis of Electron Beam Welding (EBW) by melting a sample while adjusting the settings of an electron microscope. His observation led to the birth of keyhole welding technology after ten years.

Since then, EBW machines have been used in various industries, such as aviation and aerospace, automotive, medical, marine, and nuclear [16–18]. Despite the high costs of this process, the development of flexible high-power energy sources, the benefit of minimal oxidation and entrapped gas porosity during welding, and advances in process automation have helped EBW grow as a joining technology for exotic materials and high-value parts [16].

More recent applications of electron beams as a heat source has led to the development of the ARCAM and Sciaky Electron Beam Additive Manufacturing (EB-AM) machines [19,20]. The ARCAM system utilizes a powder bed as the source material, whereas the Sciaky system uses wire fed into the melt pool [21,22].

2.2 Electron Beam Additive Manufacturing

Electron Beam Additive Manufacturing (EB-AM) systems utilize an electron beam to melt feedstock material into a near-net-shape part in a layer-by-layer fashion under a high vacuum environment [10]. An electron beam is able to melt the material by focusing a stream of

high-energy electrons onto a target area. In brief, the electrons are emitted from a cathode and accelerated by applying a high-voltage difference – e.g., 1 kV to 150 kV [23] – between a cathode and anode. A series of electro-magnetic lenses are used to focus or defocus the high-energy electrons to a beam [16]. Additionally, other electro-magnets, referred to as the "scanning coils", are used to move the beam to the desired location on the target surface.

Once the electrons strike the target metal, they rapidly decelerate, converting their kinetic energy to heat. Figure 2.1 shows schematically the interaction between an EB and the surface of a target material. Heat is typically released in the target metal within a few microns of the surface, depending on the speed of the electrons (accelerating voltage). Additionally, the bombardment of the electrons onto the target area and the interactions with the material's free electrons cause emissions of: i) Auger electrons, ii) secondary electrons; iii) backscattered electrons, and iv) X-rays [16].

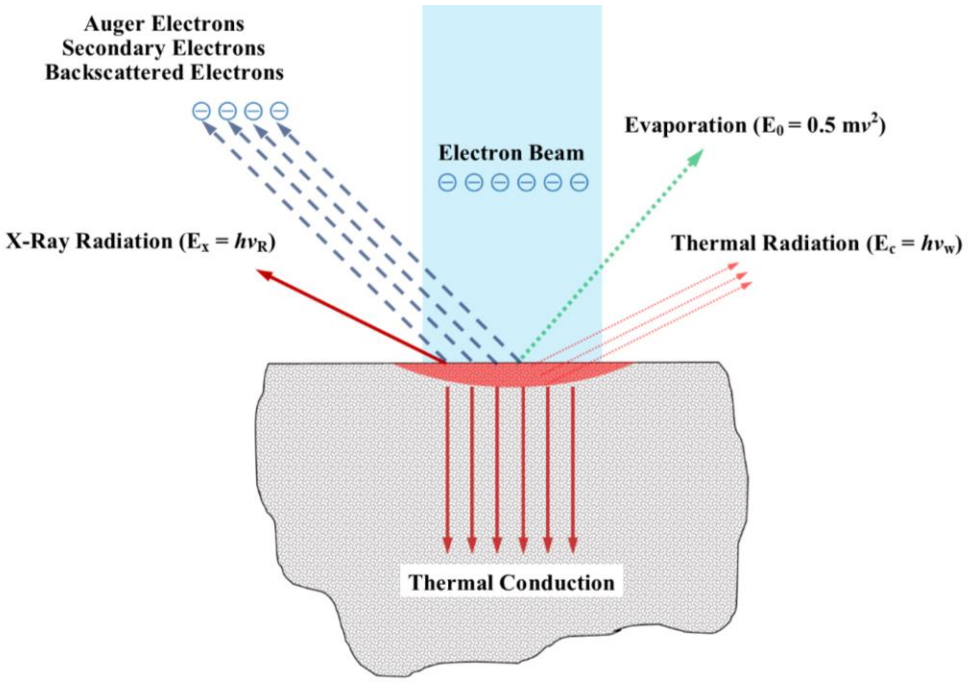

Figure 2.1. Schematic illustration of the interaction between the electron beam and the surface of a solid workpiece [16].

2.3 Software and Hardware Workflow in Electron Beam Additive Manufacturing

To begin, a 3D CAD design of a part is loaded into a software package where several process parameters are defined. For instance, these parameters would include part location within the build tank, part build orientation, the design of support structures, and heating themes. This step is represents a key element in manufacturing high-quality parts [24]. Finally, the build project file is transferred to the EB-PBF machine's controller/computer to begin the fabrication process.

As schematically shown in Figure 2.2, a commercial EB-PBF machine consists of five main elements: i) electron beam unit, ii) vacuum chamber, iii) vacuum system, iv) control system, and v) camera system.

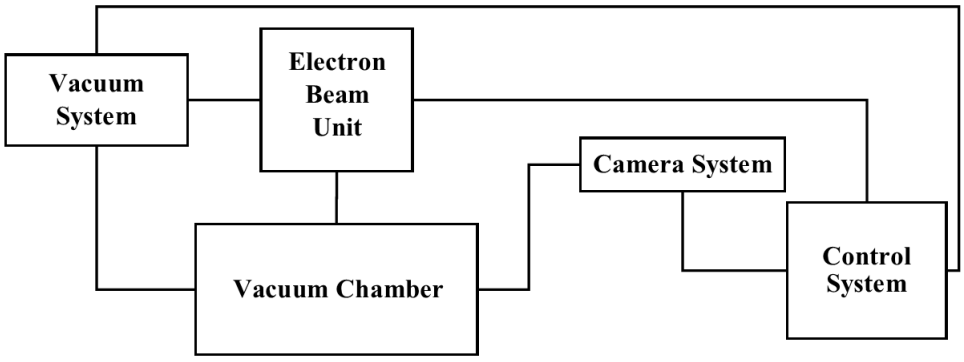

Figure 2.2. A High-level schematic diagram of the key elements of a commercial EB-PBF machine.

The electron beam unit consists of an upper and a lower section. In the upper section, the cathode emits electrons through thermionic emission. In this configuration, the electron emission relies on heating the cathode either by applying a current [25] or a laser beam [26]. In the lower section, a series of electro-magnetic lenses are used to correct and control the electron beam's shape and the spot size, and position the beam on the target area [27,28].

Prior to the fabrication process, the powder is transferred to the powder hoppers, the build platform is aligned to the powder raking system, and the removable heat shield is installed. Then, the vacuum chamber is closed and is pumped to a high-vacuum pressure range (typically 10^{-3} to 10^{-7} mbar) [28].

Once the desired vacuum pressure is achieved, the process begins by first scanning the surface of the build platform using a defocused beam to raise the temperature to a specified range; this process is known as "initial preheating". Then, the powder is spread evenly on the build platform by the powder raking system. Next, the gun is re-energized, and the powder bed is scanned to pre-heat the powder to a target temperature. Once the preheating cycle is finished, the electron beam is translated on the powder surface using a more focused spot in the pattern of the part slice being processed. The powder under the focused spot is melted/sintered to form a solid using an appropriate theme (combination of power input, spot focus, beam speed and beam pattern). Afterwards, a second heat input, referred to as "post-heat", may also be used to input more energy into the powder bed prior to adding the next powder layer, depending on the overall process heat balance at that time. The build process continues by repeating the four cycles shown in Figure 2.3 until the components are built [27].

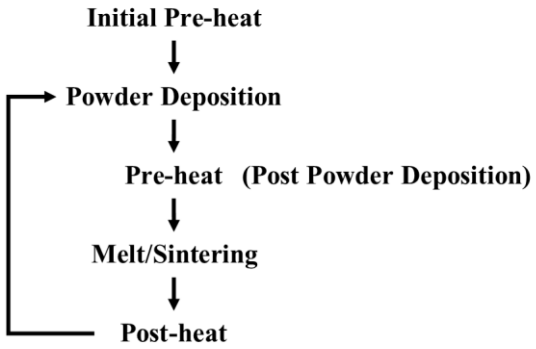

Figure 2.3. Schematic diagram of fabrication process cycle in EB-PBF process [27].

The initial preheating cycle facilitates the outgassing of the build platform or the heat shield and increases the starter plate temperature to within a specified range. The subsequent preheating cycles (i.e., post powder deposition preheating cycles) help slightly sinter the powder particles to enhance the electrical conductivity and create mechanical coherency [28]. Partial (or weak) sintering of the powder during preheating helps prevent a process instability (known as "powder smoking") during the melting process. Studies have correlated this phenomenon to the poor electrical conductivity of loose powder, which leads to powder becoming charged and electric repulsion of powder particles during the melting stages [21,29].

Once the fabrication process is completed, the accumulated heat in the build chamber requires an extended cooling time. Once it is cooled down to a specific temperature range, it can be opened. Then, the build is moved to the Powder Recovery System (PRS), where the partially sintered powders are removed from the build envelope and recovered for future use. Further details on the process principles are thoroughly presented by Gong *et al.* [30].

The EB-PBF process is carried out under a high-vacuum environment, ensuring low oxygen and nitrogen pickup [34] and a reduced pore size distribution [30]. Additionally, the high-temperature build environment results in a lower temperature gradient across the build volume compared to other metal AM processes [31]. Despite many advantages in the EB-PBF process, it faces some challenges, which are highlighted in the following section.

2.4 Defects in the EB-PBF Process

The interaction between the beam and feedstock material is complex, as is the transport of heat within the build chamber. A poor choice of process parameters can lead to powder smoking [29] or various defects in the product – e.g., lack of fusion [32], alloying element evaporation [10,33],

dimensional inaccuracy (distortion) [34], gas porosity [35,36], and layer delamination [27]. Some of these defects are dependent on the theme; however, some are also a function of the thermal environment within the build chamber. Hence, thermal management within the build envelope is also necessary to ensure a consistent part quality.

Of these defects, part distortion and layer delamination, if severe, can lead to the process being suspended [27,34]. Several studies [31,37–39] have focused on understanding the source of these defects – i.e, part distortion and layer delamination. It has been found that, in most cases, large temperature gradients within the component lead to these defects [31,38,39]. EB-PBF parts typically experience a lower temperature gradient across the build volume during the process compared to laser-based processes [31] owing to the ability to apply pre-heat and post-heat, and the absence of convective heat transport from the PB surface, which facilitates maintaining a high-temperature within the build environment [21]. This high-temperature environment may also act as a post-process heat treatment (e.g., stress-relief annealing) [40], which results in a lower residual stress accumulation in the fabricated part [6,21].

The high-temperature and high-vacuum build environment may facilitate selective evaporation of low vapour pressure elements [21]. The element loss during the build process can locally change the chemical composition, which influences corrosion resistance [10], as-built microstructure [33,41], and mechanical properties [10,33] of the product.

The following section introduces a few key process parameters in the EB-PBF process, and their effects on the formation of defects are briefly explored.

2.5 Process Parameters in EB-PBF

Studies [42–47] have shown that changing process parameters can influence the quality of final parts and the formation of several defects, as presented in Table 2.1. In the EB-PBF process, the key process parameters can be classified into four categories [44]: i) electron beam parameters (e.g., accelerating voltage, beam current and beam focus), ii) scan strategy and speed, iii) powder-dependent parameters (e.g., particle shape, size, distribution, and layer thickness), and iv) preheating and post-heating temperatures.

Table 2.1. Recommendations and guidelines to minimize defects and improve part's quality fabricated by EB-PBF

Defect/flaw to minimize	**Recommended solution**	
	Increasing	**Reducing**
Porosity and lack of fusion	Line energy [42]	Scan speed [42,43]
		Focus offset [42,43]
		Line offset [48]
Surface roughness	Scan speed [42,43]	Beam current [43]
	Particle size [46]	Layer thickness [44]
	Focus offset [42,43]	Line energy [42]
		Line offset [48]
Delamination	Energy density [47]	Focus offset [42,43]

It is suggested that a few flaws/defects, such as surface roughness [49] and enclosed smaller porosity [35,36], can be repaired by post-processing operations, as opposed to defects mentioned in **Section 2.4**.

2.6 Temperature Measurements in EB-PBF

As discussed, process parameters could significantly influence the localised thermal energy input during the EB-PBF process, leading to a larger temperature gradient across the build-volume [8]. Therefore, careful thermal management within the build chamber is necessary to ensure a consistent part quality; otherwise, various defects may appear in the product [8,31,40].

Several studies suggested that recording temperature data during the EB-PBF process could be used for process monitoring [50–54]. For example, Cordero *et al.* [50] examined the feasibility of implementing a pyrometer and an infrared (IR) camera to measure temperature. They suggested that surface temperature measurements from the build area could be used for developing process parameters and as feedback for a closed-loop control system to adjust the energy deposition during melting. Buga and Dsouza [51] developed a temperature monitoring solution using an IR camera and image processing. They demonstrated that the temperature fluctuations over the build surface could be mapped in real-time for successive layers during the build process. In addition, Boone *et al.* [52] developed a high-speed and high-resolution thermal imaging instrument for recording layer surface temperatures and monitoring the melt pool during the build process within the ARCAM A2 EB-PBF machine. They reported that the thermal images could be used to detect defects during the build process. Furthermore, Fisher *et al.* [53] used thermal imaging as an indirect means of monitoring solidification conditions in the ARCAM A2 EB-PBF system. They proposed that the temperature from the build surface could be used as feedback to control the microstructure evolution during the fabrication process – in terms of the localised heat input to the PB during the build process.

Other studies suggested that temperature measurements could be used to study the thermal characteristics of the EB-PBF processes [54–58]. For instance, Price *et al.* [54,56] measured melt pool sizes and the surface temperature with a near-infrared camera for various sets of a process parameter. They reported that changing a process parameter referred to as "speed function index", which controls the beam current and the beam speed during a build, showed a noticeable influence on the melt pool sizes, surface roughness and morphology of the fabricated parts. Rodriguez *et al.* [55] measured the surface temperature of the powder bed with an IR camera and a feedback signal

from an EB-PBF machine. The integrated instrument captured thermal images from the powder layer's surface at three stages – i.e., preheating, melting and powder deposition. They suggested that thermal imaging could be used to identify non-uniformity in the temperature distribution on the build area during the EB-PBF process. In another study, Lee *et al.* [57] investigated the role of a new scan strategy, referred to as the "ghost beam scan strategy", on the temperature gradient and local microstructural evolution for IN718 alloy. They observed that the new scan strategy had positively influenced the solidification conditions and the temperature gradient compared to the conventional spot melting and raster scan strategy.

For in-situ temperature measurements, thermocouples are the simplest and most cost-effective tools that can provide accurate temperature data at discrete points [55,58,59]. Generally, multiple thermocouples are needed to accurately measure a temperature since each thermocouple can measure temperature from a single location. For instance, Rodriguez *et al.* [55] recorded the in-situ temperature evolution on the heat shield of the ARCAM A2 EB-PBF machine with thermocouples, as shown in Figure 2.4. The temperature measurements were used to validate a numerical model that described the view factor associated with the radiative heat transfer within the machine's heat shield enclosure.

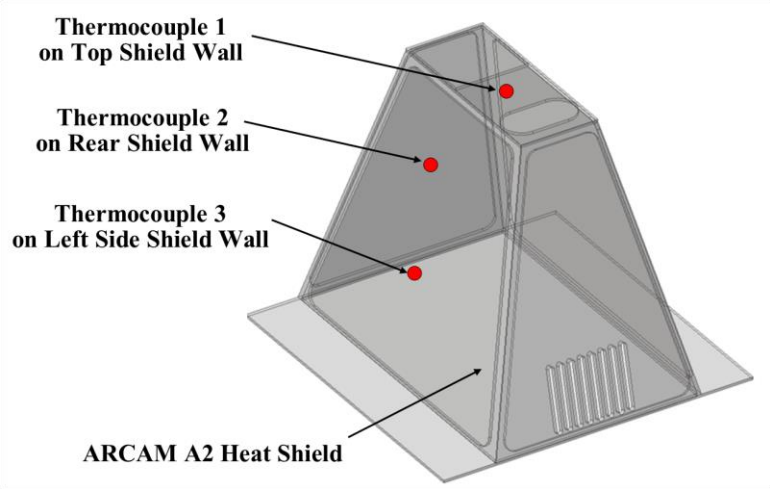

Figure 2.4. A 3D schematic of the ARCAM A2 heat shield instrumented with thermocouple [55].

In a recent study, Landau *et al.* [58] instrumented the build environment of a GE-ARCAM Q20plus EB-PBF machine with thermocouples and recorded the evolution of temperatures from multiple locations, as shown in Figure 2.5. The temperature measurements were used to validate a heat transfer model that characterises the heat transport within the build chamber.

Despite the advantages of using thermocouples for acquiring in-process temperatures, Gouge *et al.* [59] reported that measurement anomalies might occur due to the electromagnetic interference from the electron beam magnetic field. In addition, using thermocouples requires the installation of a thermocouple feedthrough on the EB-PBF machine [58].

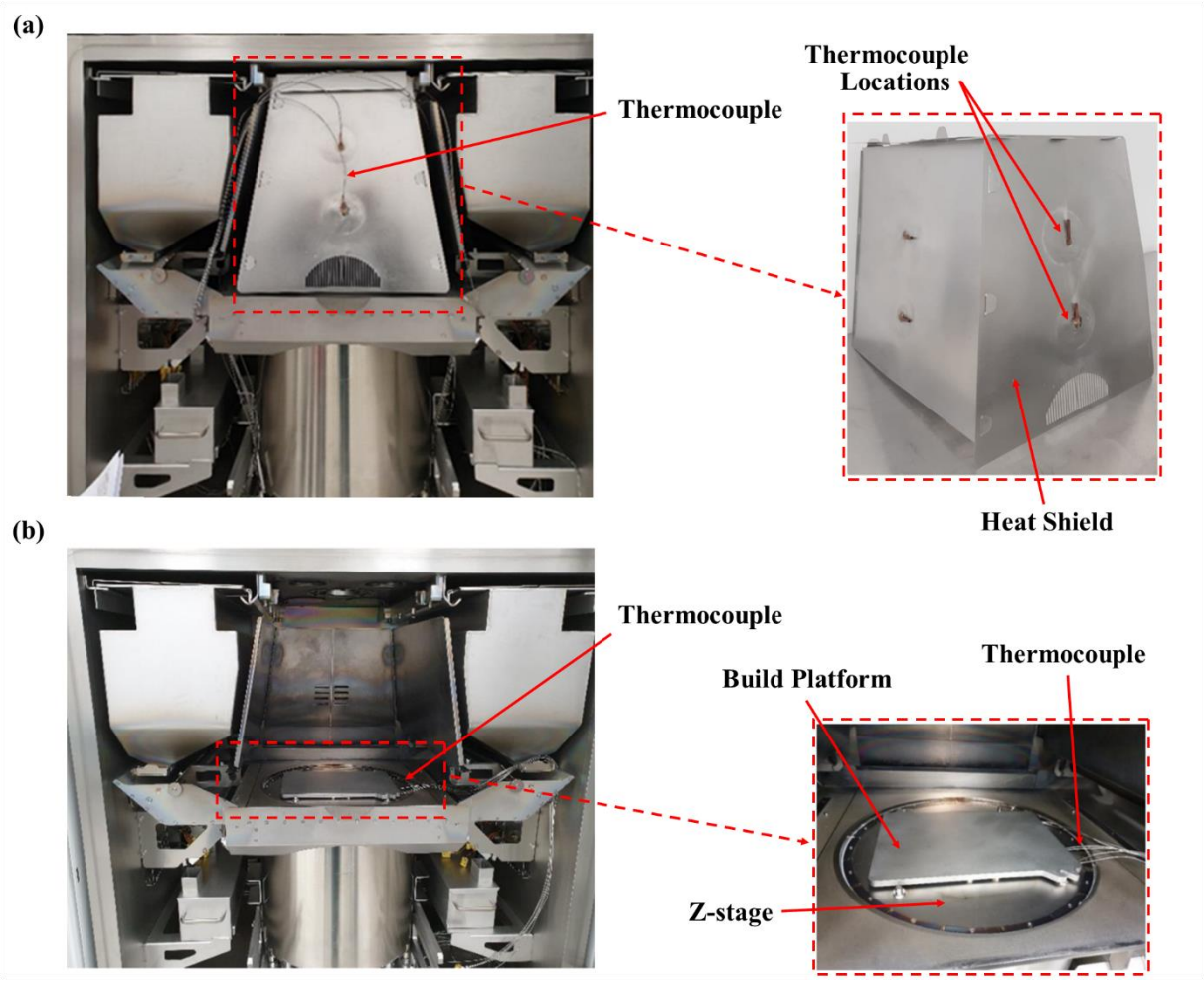

Figure 2.5. In-situ temperature measurement set-up implemented in the GE-ARCAM Q20Plus EB-PBF system; showing (a) the heat shield and (b) the build platform are instrumented with type-K thermocouples [58].

Some researchers [55,56,60–64] focused on using infrared or near-infrared cameras and pyrometers to record temperature in-situ, as shown in Figures 2.6 (a) and (b). The intensity of the emitted radiation and the emissivity of the radiating surface can be used to calculate the surface temperature [65]. Despite the advantages of using pyrometers, Cordero *et al.* [50] reported that temperature measurements with pyrometers are limited to a single spot, as shown in Figure 2.6 (c).

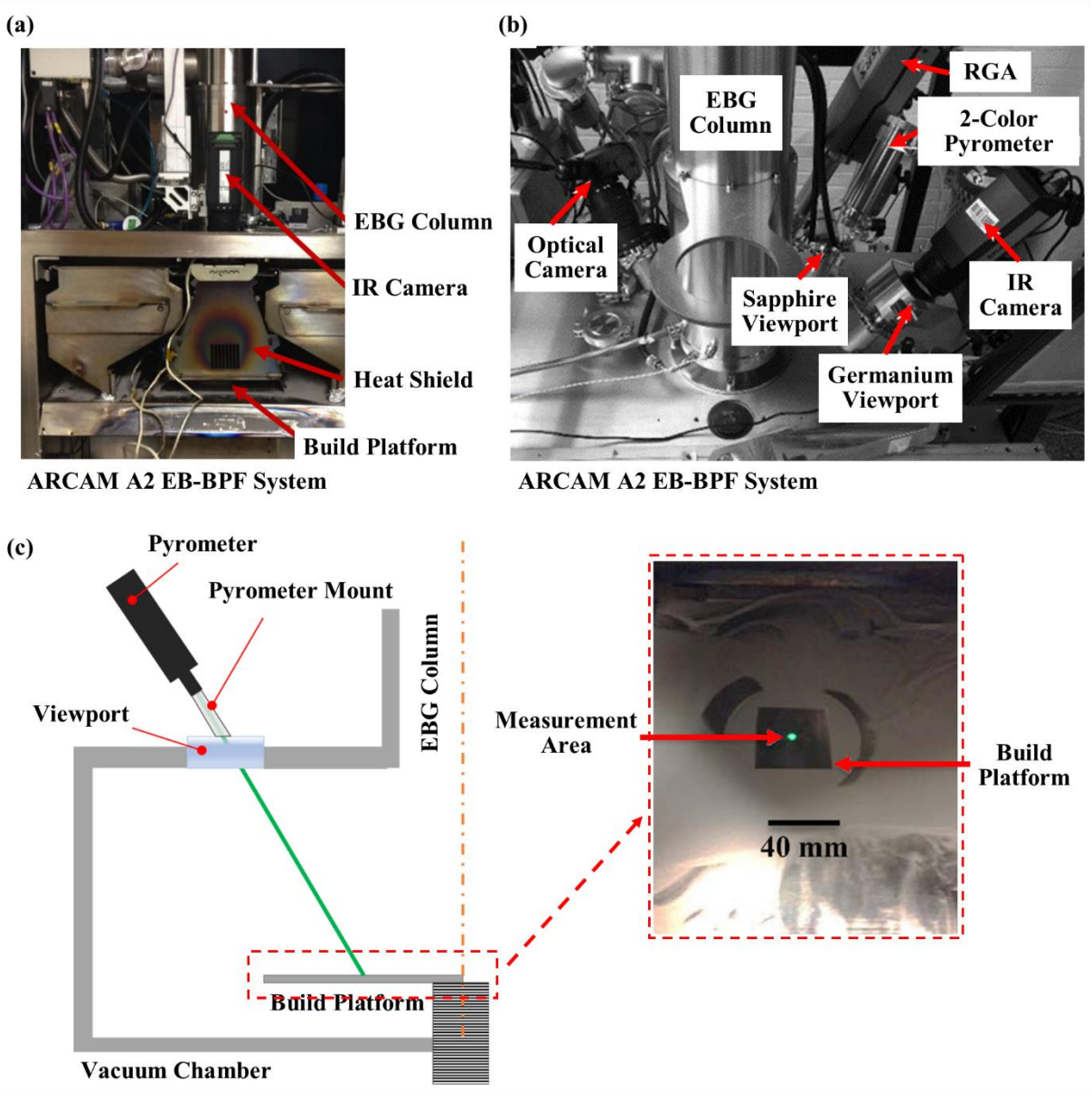

Figure 2.6. Experimental set-up for in-situ temperature measurement using (a) IR camera [66] and (b) pyrometer and IR camera [67], and (c) schematic illustration of temperature measurement set-up with a pyrometer– green spot shows the area where pyrometer records data [50].

Additionally, metallisation on the viewport optics due to the prolonged exposure to metal vapours during the EB-PBF process influences the accuracy of temperature measurements, see Figures 2.7 (a) and (b) [50,51,63]. Hence, Boone *et al.* [52] and Croset *et al.* [60] designed a complex Kapton film-feed apparatus to minimise the effect of metallisation on the accuracy of measurements, as shown in Figures 2.7 (c) and (d). However, this required modification to the EB-PBF machine's vacuum chamber. Furthermore, Gouge *et al.* [59] stated that the measurement equipment must be frequently calibrated to record accurate temperature data.

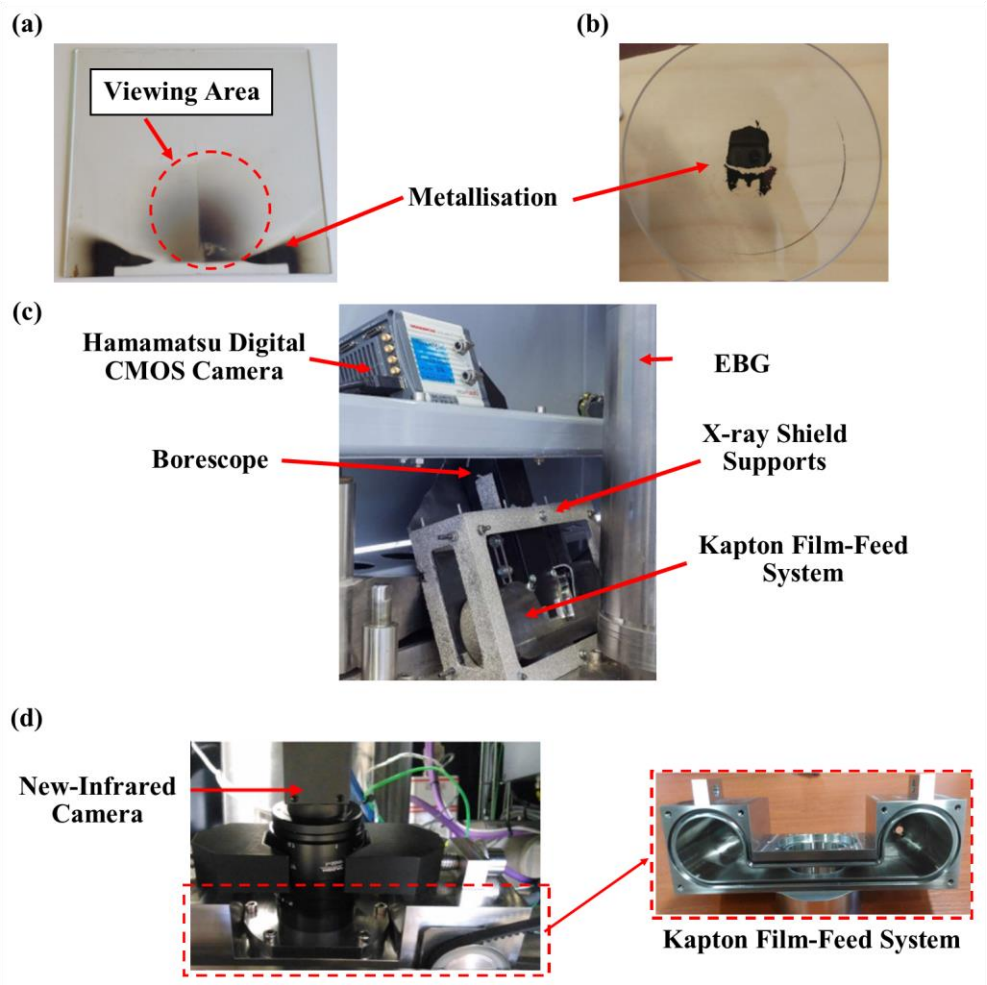

Figure 2.7. Metallisation on (a) a sacrificial glass [63] and (b) a viewport optic [51] after in-situ thermal imaging. Complex Kapton film-feed system for in-situ thermal imaging implemented to (c) ARCAM S12 [64] and (d) ARCAM A1 EB-PBF systems [68].

While the vast amount of work on the EB-PBF process has been experimental in nature and focused on process characterisation, several studies have been published on the numerical modelling of heat transfer in the EB-PBF process [54,58,69–71]. For example, Price *et al.* [54] developed a thermal model to predict the melt pool shape and size as a function of a system-specific parameter, referred to as the "speed function index". They reported that the speed function could noticeably influence the melt pool size and shape and the temperature distribution along the melt track. In another study, Alderson [69] developed a 3D heat transfer model to predict the temperature distribution for a moving heat source with respect to the scan path. It is suggested that the model results could be used to evaluate the accumulation of residual stresses with respect to the temperature gradient within the part. In a recent study, Landau *et al.* [58] developed a 3D heat transfer model to characterise the thermal behaviour of the build chamber during the preheating sequence. They used thermocouples to measure the temperature from multiple locations on the heat shield and within the build platform (see Figure 2.5), and they validated the model with respect to these measurements. They showed that the radiative heat transfer within the build chamber is more dominant than the heat conduction to the build platform. The energy balance over the build platform in this study showed that approximately 80% of the input energy from the EB is absorbed by the heat shield via radiation, while 20% was absorbed by the build platform at the steady-state condition.

According to the literature review, there is a good argument that can be made for developing validated numerical models that focus on heat transfer at both the meso and macro length scales – i.e., at the scale of the melt pool and build chamber – to characterise the thermal field within the build chamber and develop a better understanding of the key transport processes affecting build quality. This research presents the development and validation of a numerical

thermal model to predict the evolution of the macro thermal field within a simplified build environment. The model is developed in stages, with the first stage predictions validated against temperature measurements obtained from a simplified build environment constructed in an Electron Beam Button Furnace (EB-BF) during heating and cooling of a titanium disk in the absence of powder. Following model validation, several different simplified cases were simulated, examining the effect of the heating pattern size, preheating, and powder deposition sequence on the development of the thermal field within the build environment.

Chapter 3: Scope and Objectives

As discussed in Chapter 2, the selection of process parameters can influence the formation of various defects in products fabricated by the EB-PBF process, and it is impractical to adjust them by the trial and-error methodology. Therefore, developing and validating numerical models that focus on heat transfer within the build environment will aid to understand the key transport processes affecting the temperature gradients within the build environment. These models can also be used to identify the appropriate set of process parameters.

Toward this goal, the present thesis is presented in the form of two manuscripts. The first manuscript (Chapter 4) presents the development of a numerical heat transfer model describing the transport of heat within a simplified build environment with respect to an experiment conducted in a lab-scale Electron Beam Button Furnace (EB-BF). The experiment included constructing a simplified build environment within the EB-BF, generating a circular beam trajectory pattern, and heating a titanium disk in the absence of powder. The model predictions were validated against temperature measurements obtained from the simplified build environment during the heating and cooling of the titanium disk. An autonomous data acquisition system was developed and used for in-situ instrumentation inside the EB-BF to record the evolution of temperature during the experiment. The second manuscript (Chapter 5) presents the design framework for this system.

Following model validation, several numerical cases were simulated, examining the effect of preheating cycles, various heating pattern sizes and powder deposition on the evolution of the thermal field within the simplified build environment.

Chapter 4: A simplified approach to modelling the thermal balance of the build environment in electron beam additive manufacturing

While the vast amount of work on the EB-PBF process has been experimental and focused on process characterization, several studies have been published on the numerical modelling of heat transfer in the EB PBF process, as mentioned in Chapter 2. The process is so complex that it would be beneficial to develop and validate numerical models that focus on heat transfer at both the meso and macro length scales – i.e., at the scale of the melt pool and build environment (the environment between the heat shield and the build platform). These numerical models will help to better understand the key transport processes affecting build quality.

This chapter presents the development and validation of a numerical thermal model aimed at predicting the evolution of the macro thermal field within a simplified build environment constructed in the EB-BF. The model is developed in stages, with the first stage predictions validated against temperature measurements obtained from an experimental setup fabricated in the EB-BF during both heating and cooling of a titanium plate in the absence of powder. Following model validation, several simplified numerical cases are simulated, examining the effect of the heating pattern size, preheating, and powder deposition sequence on the development of the temperature and the energy balance within the simplified build environment.

4.1 Experimental Procedure

Figure 4.1 (a) shows the lab-scale EB-BF that was used in this study. This system was chosen as it provides good access to the vacuum chamber for instrumentation and a basic gun control system for prescribing simple beam trajectory patterns in comparison to a commercial EB-PBF system – e.g., GE-ARCAM Q20Plus available at the University of British Columbia.

The EB-BF was equipped with two independent, two-stage vacuum pumps (one for the EB gun column and one for the furnace chamber), a water-cooled copper mould, a Von Ardenne EB gun with a nominal power rating of 30 kW at 20 kV, and an analogue, in-house developed, beam deflection system for controlling the beam position.

The experimental set-up that represents a simplified build environment, also referred to as the "pseudo build environment", consisted of a base platform and a GE-ARCAM Q20plus heat shield, as shown in Figure 4.1 (b) and Figure 4.2. The heat shield is made from 304L stainless steel, and it was simplified by removing the top of the heat shield. This was to avoid blocking the beam as the gun on the EB-BF is located at an angle to the pseudo build environment base – i.e., not normal as is the case in the GE-ARCAM system.

The base platform consisted of a circular disk (96 mm in diameter × 13 mm in height) of commercial purity titanium (CP-Ti) placed within a hole in the centre of a plate fabricated from 304L Stainless Steel (SS). The CP-Ti disk and SS-plate were placed on a 12.5 mm thick alumina fibre blanket to provide thermal isolation from the water-cooled copper mould within the EB-BF.

It should be noted that the experimental set-up shown in Figure 4.1 (b), represents a simplified build environment within an EB-based system. Due to the simplicity of the constructed set-up, it is acknowledged that the presence of powder hoppers, the top plate of the heat shield, the secondary heat shield, and other parts within the build chamber of a commercial EB-PBF system are not included in the experimental set-up. Additionally, the dimensions and the material selected for the build platform are different from a commercial EB-PBF system. The vacuum chamber of the EB-BF is also water-cooled. Therefore, the heat transfer within the proposed experimental set-up would be different compared to an actual EB-PBF process. These factors highlight the

limitations in allowing the results from the experiments to be directly compared to commercial EBPBF system.

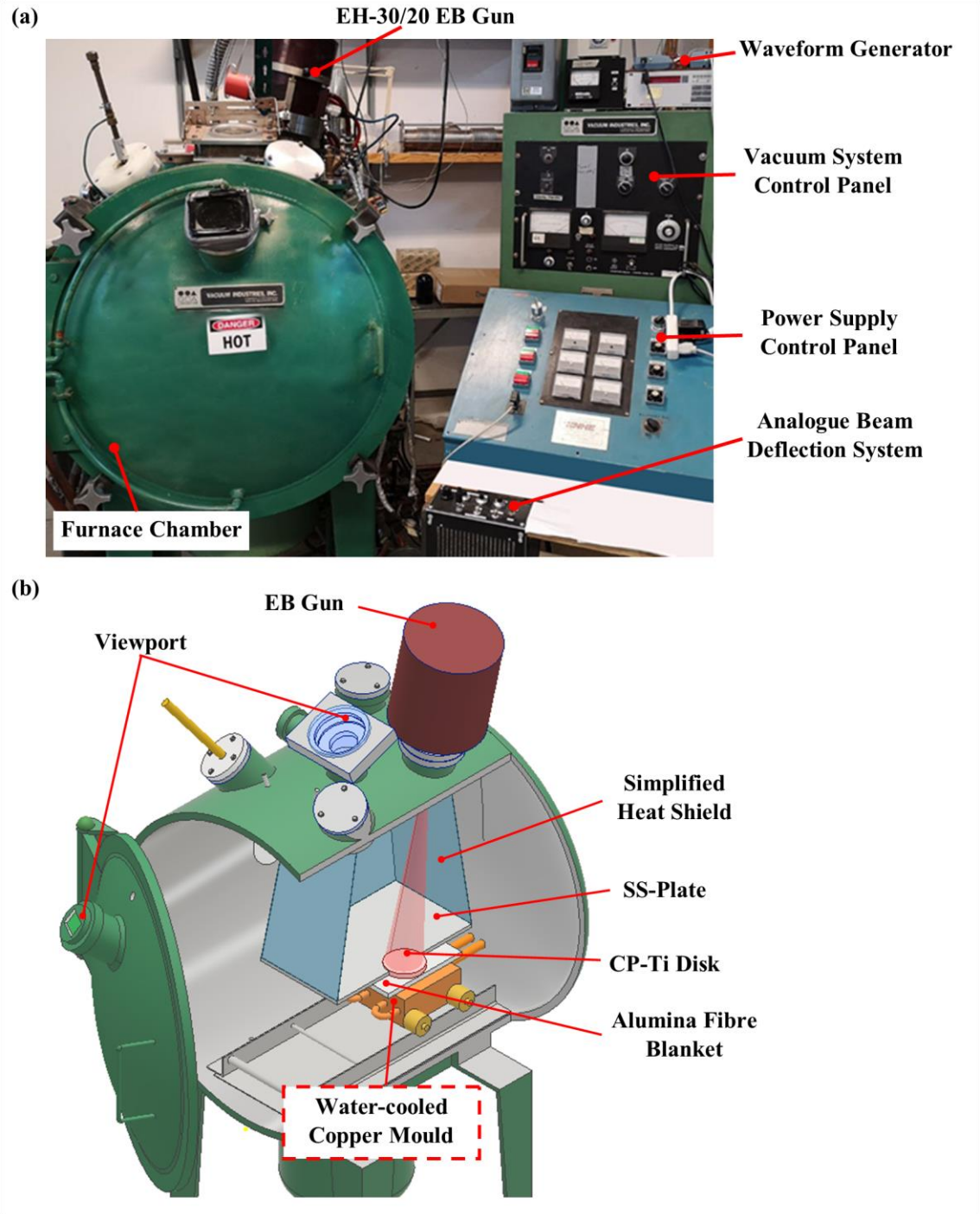

Figure 4.1. (a) The 30 kW lab-scale EB-BF, and (b) a 3D rendering cutaway view of the furnace chamber showing the experimental set-up.

The pseudo build environment was instrumented with type-K thermocouples to record the temperature evolution during the experiment. Figure 4.2 shows the thermocouple locations. TC2, TC4, and TC5 were used to record the temperature evolution close to the interfaces between the various components – i.e., the SS-plate and heat shield Face A and Face B. Similarly, TC6 and TC7 were used to measure the temperature evolution at the interface between the CP-Ti disk and the SS-plate. Since these interfaces could influence the heat transfer between each component, the temperature measurements close to these interfaces were used to adjust the interfacial heat transfer coefficient in the numerical model. TC8 was used to monitor the CP-Ti disk near-surface temperature (~2 mm beneath the top surface) for the region close to the beam trajectory pattern using an ungrounded type-K thermocouple.

Note: TCs 1 to 6 were unshielded type-K thermocouples and were spot-welded to the locations shown in Figure 4.2. On the other hand, TC7 and TC8 were shielded type-K thermocouples since the beam trajectory was positioned on the CP-Ti disk. In addition, the experimental set-up is placed on top of a layer of alumina fibre blanket, which thermally and electrically isolates the pseudo build environment from the EB-BF, as shown in Figure 4.1 (b). Therefore, all components in the experimental set-up were grounded by a Copper wire to prevent the accumulation of electrical charges during the electron beam heating experiment.

The thermocouples on the heat shield, the CP-Ti disk and the SS-plate were connected to two in-house developed in-situ data logger units that provided synchronised data logging throughout the experiments at 10 Hz per channel. Chapter 5 and Appendix A will present these in-situ data logger systems in greater detail.

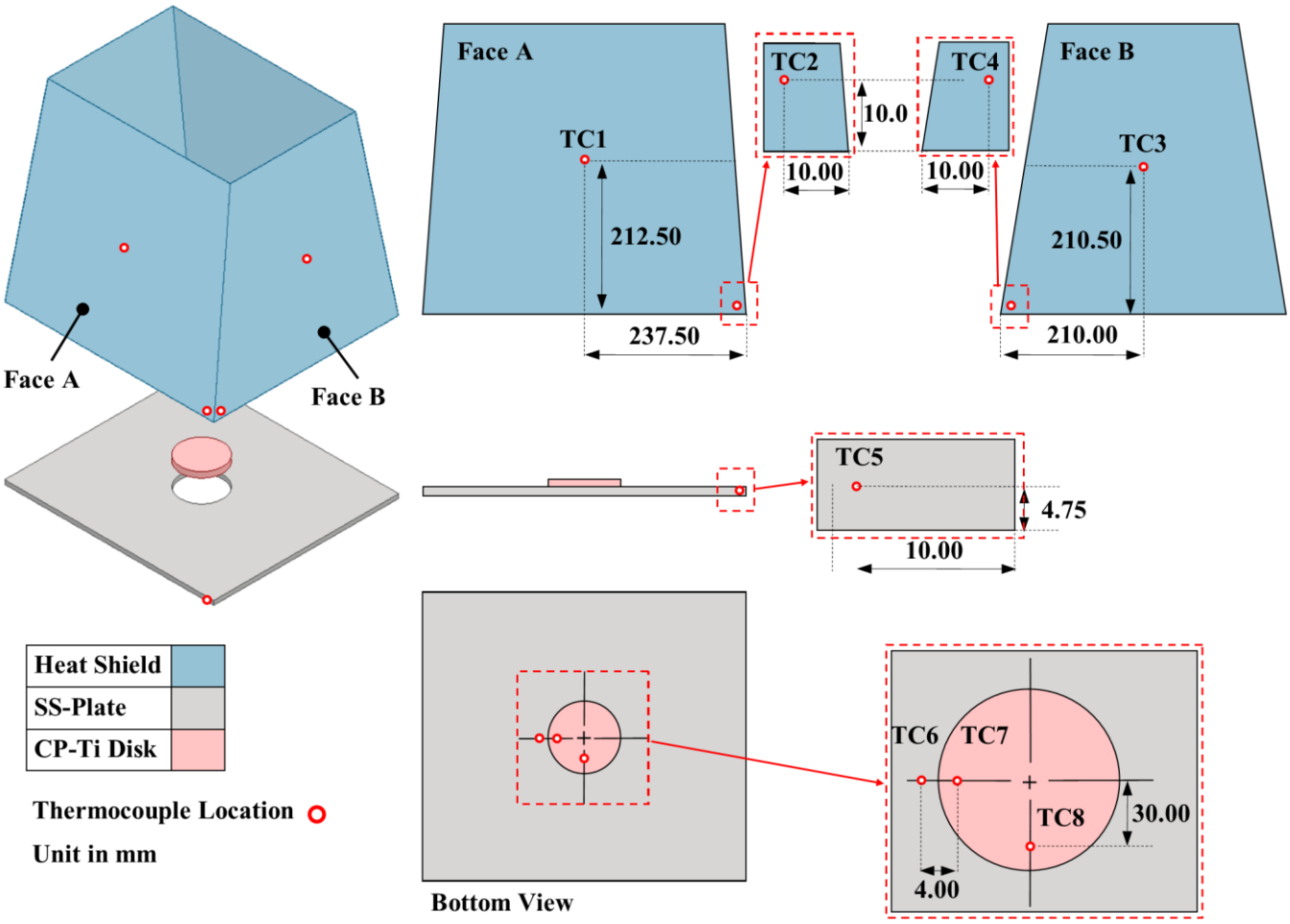

Figure 4.2. Thermocouple locations on the heat shield, the SS-plate, and the CP-Ti disk.

Once the furnace chamber reached the desired vacuum level (typically 10^{-5} to 10^{-6} mbar), the EB gun was switched on, and the power was ramped up and maintained for 50 mins, as shown in Figure 4.3 (a). The beam trajectory pattern was a circle with a radius of ~25 mm, concentric with the centre of the CP-Ti disk at a scan frequency of 20 Hz, as shown in Figure 4.3 (b). After the heating cycle, the electron beam gun was turned off, and the experimental set-up was allowed to cool down while maintaining the high-vacuum environment.

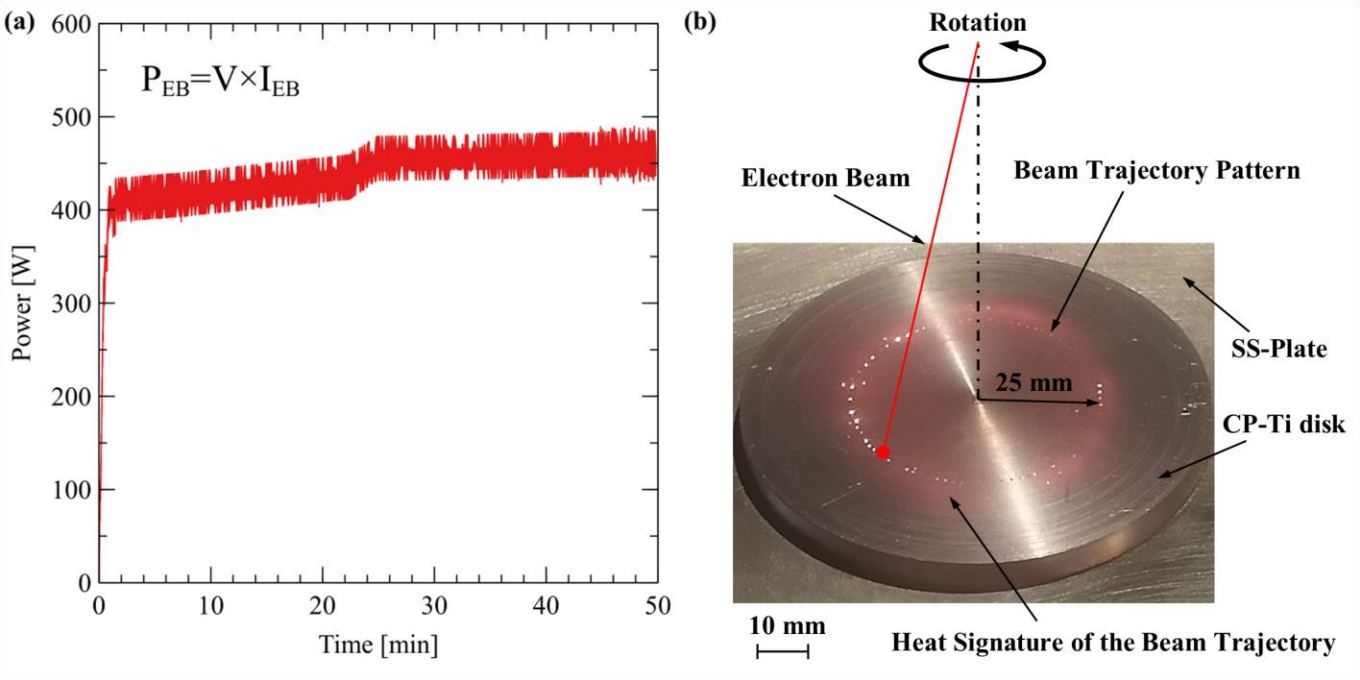

Figure 4.3. (a) The EB gun power logged from the EB-BF during the heating cycle, and (b) the beam trajectory pattern prescribed for the experiment.

4.2 Numerical Simulation

The 3D heat transfer model of the pseudo build environment within the EB-BF was developed in the commercial Finite Element (FE) package ABAQUS[1] version 2017.

4.2.1 Model Domain and Mesh

The geometries of the CP-Ti disk, the SS-plate and the heat shield were created in Inventor Pro.[2] version 2018 and imported to ABAQUS CAE. Given the symmetrical configuration of the experimental set-up, the domain size was reduced to a quarter of the pseudo build environment, as shown in Figure 4.4, to improve computational efficiency. The mesh consisted of 8-node linear heat transfer brick (DC3D8) elements. The number of elements within each component is provided in Figure 4.4.

[1] ABAQUS is the trademark for Dassault Systèmes.
[2] Inventor professional is the trademark for Autodesk Inc.

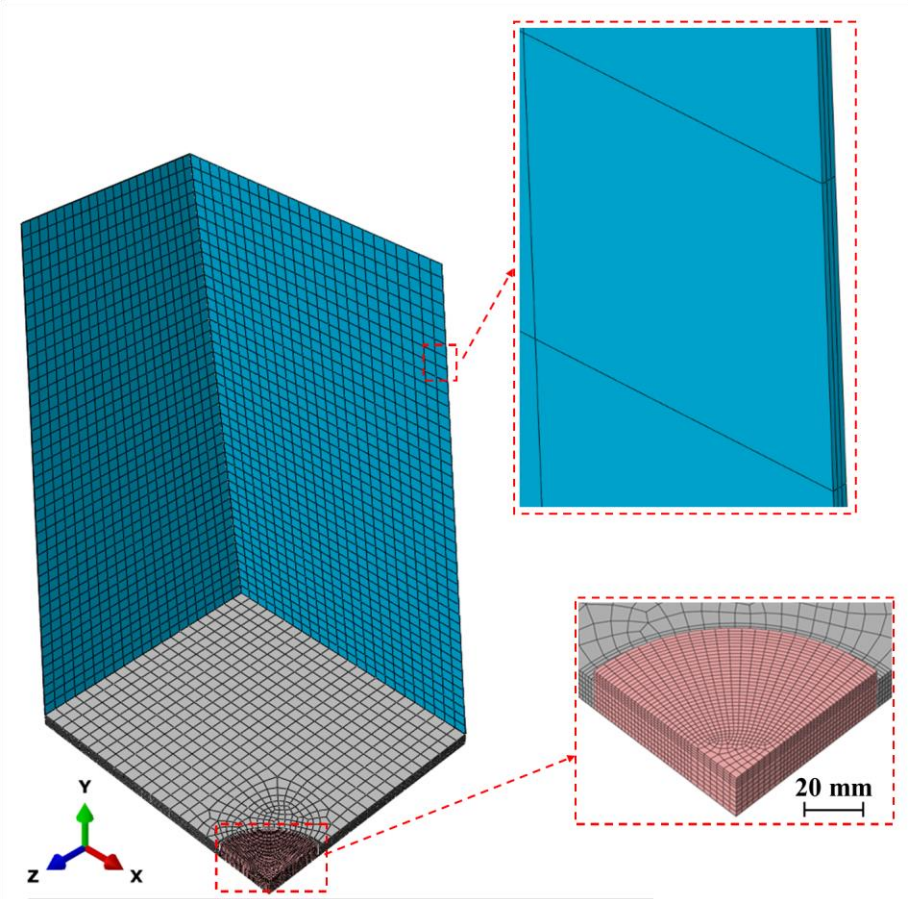

Part		Element		
		Shape	Type	Number
CP-Ti Disk		Hexahedral	DC3D8	19,215
SS-Plate				5,680
Heat Shield				6,192

Figure 4.4. Model domain meshing details.

4.2.2 Initial Conditions

The initial temperatures of the CP-Ti disk, the SS-plate and the heat shield were set to 293 K, based on the temperature measurements done at multiple locations within the pseudo build environment at the beginning of the experiment.

4.2.3 Material Properties

Figure 4.5 presents the thermophysical properties of CP-Ti and 340L SS that were implemented into the model. These materials were assumed to be isotropic and homogenous. The emissivity

values for CP-Ti and 304L SS were set to 0.6 and 0.2, respectively [72,73]. In addition, the latent heat of the α-β phase transformation was set to 87,000 J kg^{-1} at a temperature range from 1155 K to 1158 K [73]. The densities of CP-Ti and 304L SS were 4540 and 8020 kg m^{-3}, respectively, and were assumed invariant with temperature.

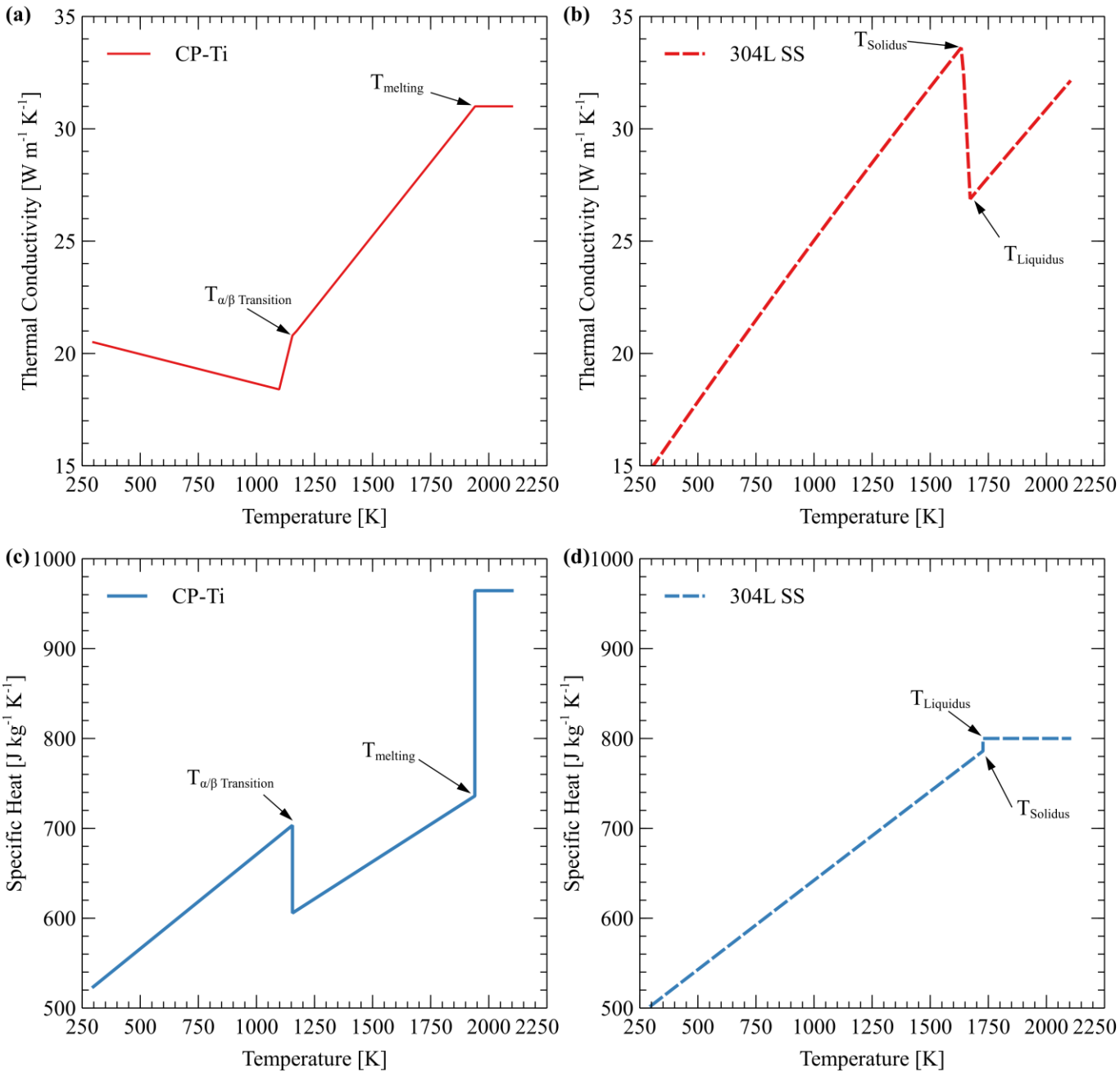

Figure 4.5. Thermophysical properties of CP-Ti and 304L Stainless Steel [72,73].

4.2.4 Thermal Boundary Conditions

4.2.4.1 Electron Beam Heating

The interaction between the EB and the surface of a material generates heat by converting the kinetic energy of electrons to thermal energy. In the numerical simulation, this heat source is defined as a surface heat flux applied to the top surface of the CP-Ti disk. A study done by Meng [74] showed that time-averaged energy input could be used for a circular beam trajectory when the scan frequency is above 10 Hz. Since the scan frequency of the beam trajectory during the experiment is 20 Hz, a time-averaged Gaussian surface heat flux can be adopted. The time-averaged Gaussian surface heat flux (presented mathematically in Eq. (4.1) and schematically shown in Figure 4.6) was implemented into the model using the DFLUX subroutine.

$$\bar{q}_{EB}(R) = \frac{\eta P_{EB}}{(2\pi R)(\sigma_{EB}\sqrt{2\pi})} e^{-\frac{(R-R_0)^2}{2\sigma_{EB}^2}} \tag{4.1}$$

In Eq. (4.1), $\bar{q}_{EB}$ (W m^{-2}) is the time-averaged Gaussian surface heat flux, P_{EB} (W) is the EB power, R (m) is the distance from the centre of the CP-Ti disk, R_0 (m) is the radius of the beam trajectory pattern, η is the EB absorption factor, and σ_{EB} (m) is the standard deviation of the Gaussian function. The implemented values for parameters in Eq. (4.1) are summarised in Table 4.1.

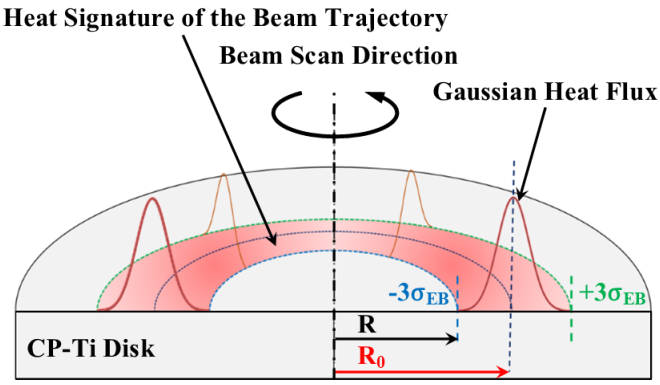

Figure 4.6. Schematic diagram of the time-averaged Gaussian heat flux distribution over the beam trajectory pattern.

Table 4.1. Beam parameters implemented in the FE model

Parameter	Unit	Value
P_{EB}	W	Figure 4.3 (a)
η	-	0.65
σ_{EB}	m	0.0025
R_0	m	0.025

4.2.4.2 Heat Losses

Figure 4.7 shows the location of the various boundary conditions defined to describe the heat transport within the build environment. These include cavity radiation (within the pseudo build environment), conduction within the base platform (i.e., CP-Ti disk and SS-plate), radiative transport from the outer heat shield walls to the furnace vacuum chamber and surface-to-surface contact heat transfer between the various components making up the heat shield walls and base platform. In addition, several boundaries were also assumed to behave adiabatically, as shown in Figure 4.7.

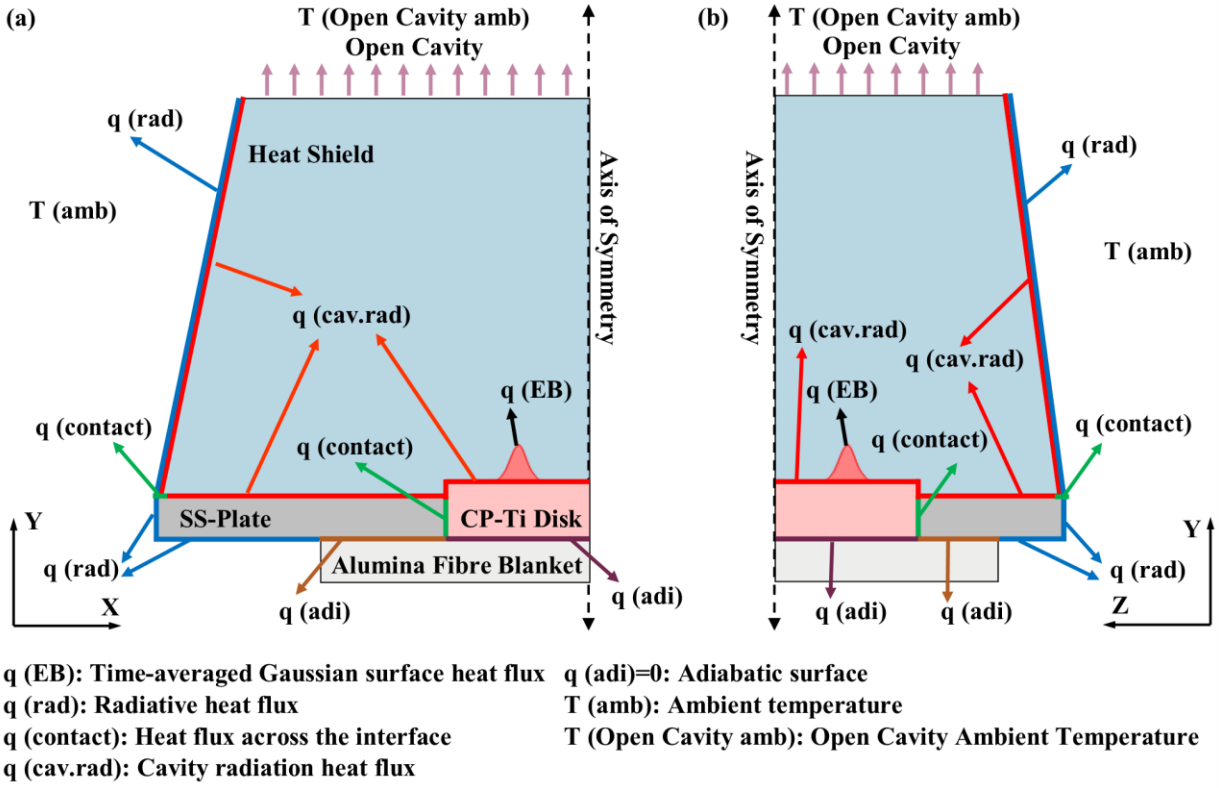

Figure 4.7. Boundary conditions of the heat transfer model along (a) XY plane and (b) ZY plane.

The surface radiation interaction assumed for the outward-facing surfaces of the heat shield walls and SS-plate, are described by Eq. (4.2):

$$q_{rad} = \varepsilon\sigma(T^4 - T_{amb}^4) \quad (4.2)$$

where q_{rad} (W m^{-2}) is the radiative heat flux, ε is the emissivity, σ (W m^{-2} K^{-4}) is the Stefan-Boltzmann constant, T (K) is the surface temperature of the radiating object, and T_{amb} (K) is the ambient temperature of the vacuum chamber walls which range from 293 to 313 K.

The temperatures measured at TC2, TC4, TC5, TC6 and TC7 (see locations in Figure 4.2) are shown in Figure 4.8 (a) and (b). The data indicated a substantial resistance to heat flow at the CP-Ti disk/SS-plate interface (see TCs 6 and 7) and similar behaviour, but to a reduced degree, at the SS-plate and the heat shield (see TCs 2, 4 and 5). The resistance to heat flow across these interfaces may be quantified using a contact Interfacial Heat Transfer Coefficient (IHTC) [75]. The mathematical relationship that describes this boundary condition is shown in Eq. (4.3):

$$q_{contact} = h_{interface}(T_A - T_B) \quad (4.3)$$

where $q_{contact}$ (W m^{-2}) is the heat flux across the interface, $h_{interface}$ (W m^{-2} K^{-1}) is the IHTC, and T_A (K) and T_B (K) are the surface temperatures at the two sides of the interface. Figure 4.8 (c) shows the temperature-dependent IHTCs applied to the SS-plate/heat shield and the CP-Ti disk/SS-plate interfaces. A trial-and-error approach was used to determine the relationship between IHTC and temperature.

Since the Alumina Fibre Blanket has a low thermal conductivity (~0.16 W m^{-1} K^{-1}), the bottom surfaces of the CP-Ti disk and the SS-plate were assumed to be adiabatic.

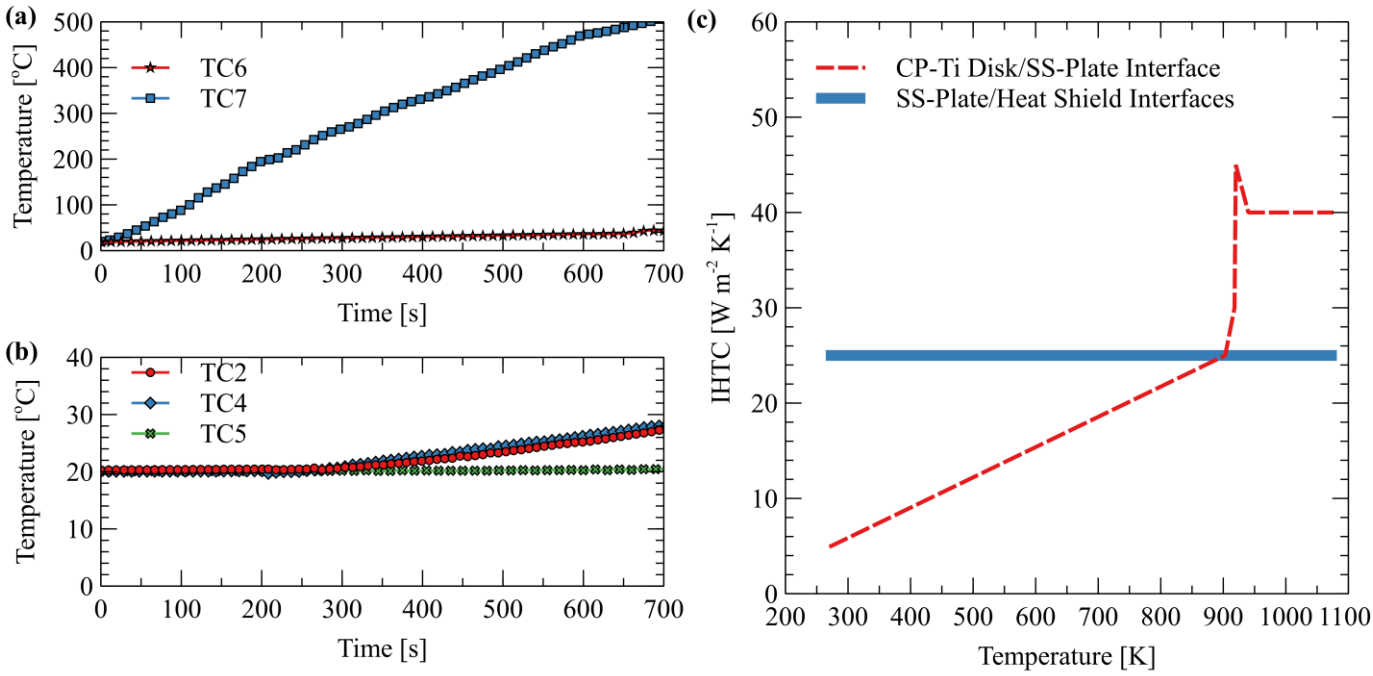

Figure 4.8. The temperature evolution in proximity to (a) the CP-Ti disk/SS-plate interface, (b) the SS-plate/heat shield interfaces, and (c) the variation of IHTC with temperature applied to the interfaces in the numerical model.

Cavity radiation interaction was applied to the top surface of the CP-Ti disk, the SS-plate, and the inner surfaces of the heat shield to describe the radiative heat exchange within the pseudo build environment. The governing equation for the cavity radiation is given in Eq. (4.4).

$$q_i = \sigma\varepsilon_i \sum_j \varepsilon_j \sum_k F_{ik} \left[\delta_{kj} - \frac{(1-\varepsilon_k)}{A_k} F_{kj}\right]^{-1} (T_j{}^4 - T_i{}^4) \quad (4.4)$$

where q_i (W m^{-2}) is the radiation flux into the facet i in a cavity, ε_i and ε_j are the emissivities of facets i and j, σ (W m^{-2} K^{-4}) is the Stefan-Boltzmann constant, F_{ij} (m^4 m^{-4}) is the view factor, T_i (K) and T_j (K) are the temperatures of facets i and j, and δ_{kj} is the Kronecker delta. The mathematical relation that describes the view factor between two facets i and j is presented in Eq. (4.5), where A_i (m^2) and A_j (m^2) are the areas of facets i and j, and r_{ij} (m) is the distance between facets i and j.

$$F_{ij} = \frac{1}{A_i} \int_{A_i} \int_{A_j} \frac{cos\theta_i \, cos\theta_j}{\pi r_{ij}^2} dA_j dA_i \quad (4.5)$$

Note: an ambient temperature is defined in the case of open cavity radiation interaction. Since the model domain in this study represents an open cavity, as the top plate of the heat shield

is not included in the experimental set-up, and the model domain, an average ambient temperature of 30 ℃ was defined with respect to the experiment.

4.3 Results and Discussion

4.3.1 Experimental Results

Figure 4.9 (a) shows the heat shield temperature evolution on Face A (TCs 1 and 2) and Face B (TCs 3 and 4) (refer to Figure 4.2 for locations of TCs 1 through 4). As shown in Figure 4.9 (a), the temperature in the centre of Face A (TC1) reaches a peak temperature of ~100 °C at 50 minutes, whereas the temperature at the centre of Face B (TC3) reaches a peak temperature of ~95 °C. Similarly, the temperature is slightly higher at TC2 on Face A (80 °C) than TC4 (~76 °C) on Face B. This temperature difference exists because the angle between Face A and the Y-axis is 6° greater than that of Face B in the heat shield. The larger angle influences the view factor (see Eq. (4.5)), resulting in a slightly higher radiation transfer to Face A than Face B.

Figure 4.9 (b) shows the temperature evolution on the SS-plate (TCs 5 and 6) and CP-Ti disk (TCs 7 and 8). The peak temperature on the SS-plate in proximity to the CP-Ti disk/SS-plate interface (TC6) is ~117 °C, whereas the temperature close to the SS-plate/heat shield interface (TC5) reaches a peak temperature of ~32 °C. The results show that the CP-Ti disk reaches a steady-state temperature of ~662 °C (TC7) and ~725 °C (TC8) when the heat shield is included in the experiments.

Note: the pseudo build environment does not reach a steady-state condition since the temperature on the heat shield walls and within the SS-plate change during the experiment.

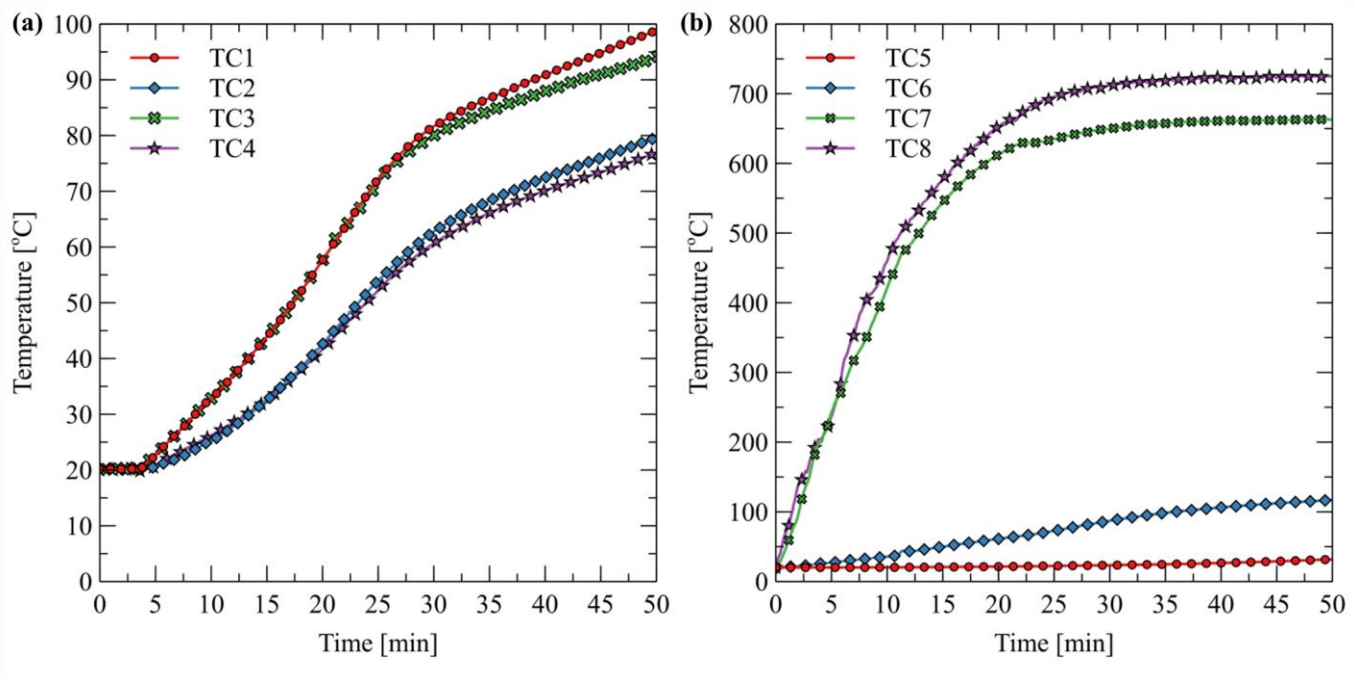

Figure 4.9. The temperature evolution on (a) the heat shield and (b) the CP-Ti disk and the SS-plate during the heating experiment.

Figure 4.10 shows the temperature evolution at TC8 in two separate experiments, one with and the other without the heat shield. The peak temperature reached in the experiment with the heat shield was ~725 °C and ~670 °C without the heat shield. Additionally, the results show that the CP-Ti disk approaches a steady-state temperature when the heat shield is included in the experiments. However, when the heat shield was absent, the CP-Ti disk's temperature continued to change over the 50-minute timeframe of the experiment.

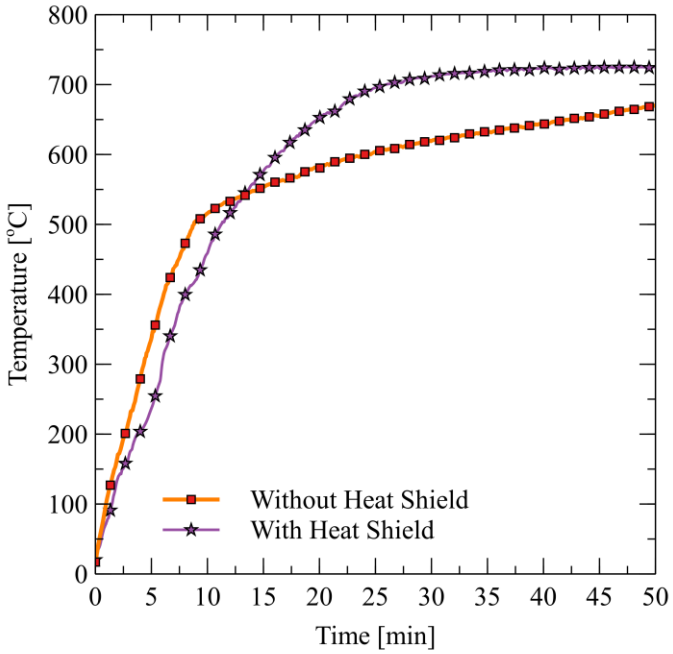

Figure 4.10. The temperature evolution on the CP-Ti disk (TC8) in two heating experiments with and without the heat shield.

4.3.2 Validation of the Heat Transfer Model

Figure 4.11 compares the experimental temperature measurements to the model predictions during the heating and cooling stages of the experiment. Overall, a satisfactory agreement between the experimental and model predictions is achieved during both heating and cooling. The difference between the temperature predictions and the experimental measurements were evaluated and generally fell within ±10 %.

A sensitivity analysis was conducted using the model to identify the key factors affecting the model results, as presented in further detail in Appendix G. One of the key parameters was the IHTC at the CP-Ti disk/SS-plate interface. Additionally, the ambient temperature within the furnace chamber was also found to significantly influence the prediction of the heat shield wall temperatures, as would be expected.

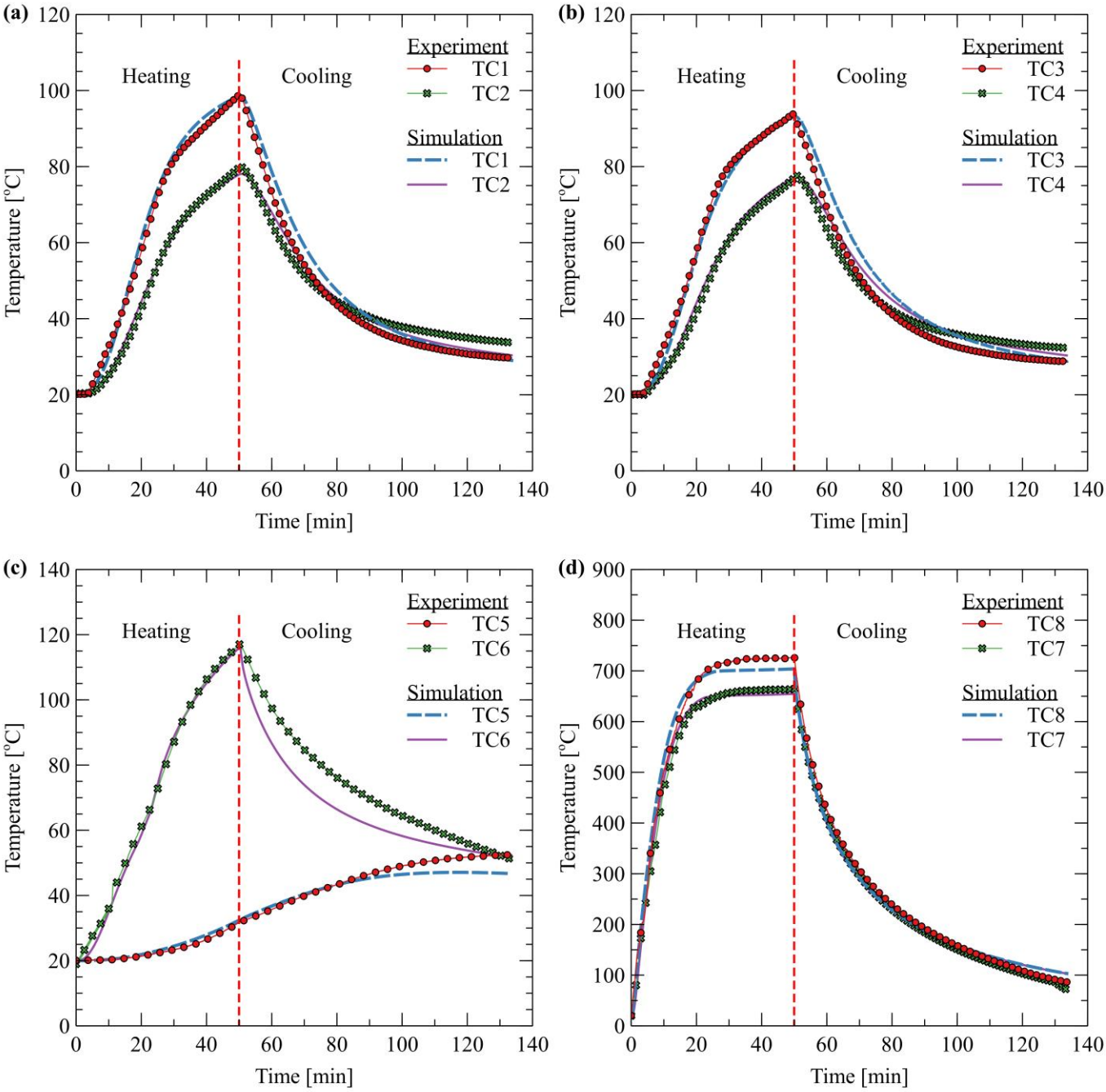

Figure 4.11. Comparison between the temperature evolution predicted by the numerical model and the experimental measurements on (a) the heat shield Face A, (b) the heat shield Face B, (c) the SS-plate, and (d) the CP-Ti disk.

4.3.3 Temperature Distribution in the Pseudo Build Environment

Having validated the model, the focus is shifted to the overall temperature distribution in the pseudo build environment. Figure 4.12 (a) shows the temperature distribution in the heat shield at the end of the heating cycle. The peak temperature is observed approximately 1/3 of the way up the heat shield walls in the centre of each face. Further, the temperature predicted on Face A is slightly higher than on Face B, for the reason discussed previously. To assess the magnitude of this difference quantitatively, two temperature profiles were evaluated along lines A-A' and B-B', as shown in Figure 4.12 (b). The minimum and maximum temperature differences on Faces A and B were ~3 °C and ~9 °C, respectively.

Figure 4.12 (c) shows the temperature contour plot of the CP-Ti disk at the end of the heating cycle. The temperature contour shows the peak temperature to be 755 °C in a circular band on the top surface of the CP-Ti disk, consistent with the beam trajectory. The outer circumference of the disk, where heat is lost to the SS-plate, is predicted to be significantly cooler at approximately 640 °C.

To determine the radial temperature distribution in the CP-Ti disk at the end of the heating cycle, two temperature profiles were evaluated along lines C-C' (on the top surface) and D-D' (on the bottom surface), as shown in Figure 4.12 (d). As can be seen, at the centre of the beam trajectory pattern, the maximum difference between the top surface and bottom surface is ~50 °C, indicating the conduction of heat out of the CP-Ti disk to the SS-plate.

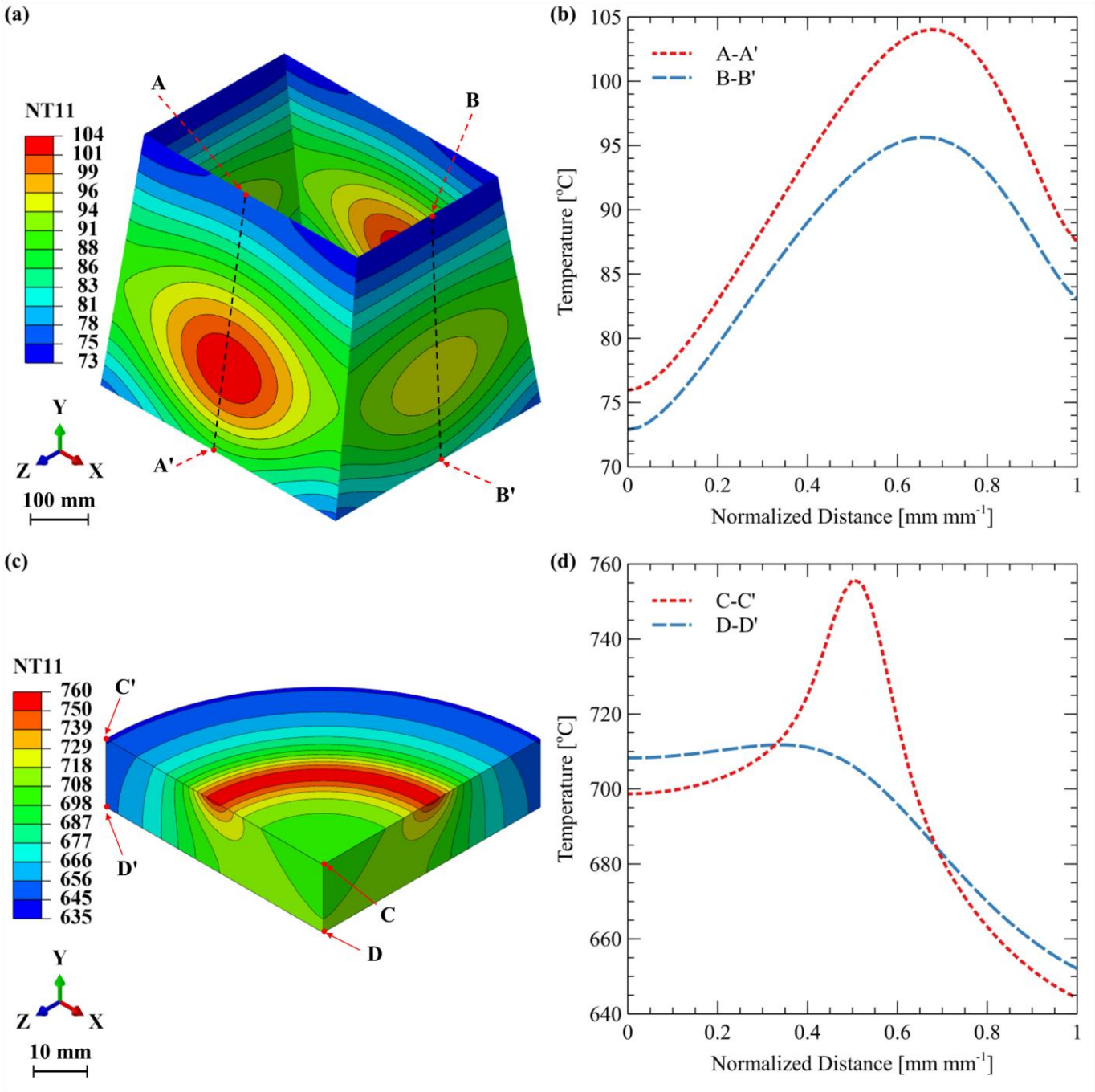

Figure 4.12. (a) The temperature contour of the heat shield, (b) the temperature profiles along lines A-A' and B-B' on the heat shield, (c) the temperature contour of the CP-Ti disk, and (d) the temperature profiles along lines C-C' and D-D' on the CP-Ti disk.

4.3.4 Power and Energy Balances

The area-integrated heat flux over the CP-Ti disk top surface was calculated in ABAQUS to understand the flow of heat in the set-up used in this study. To this end, Figure 4.13 shows the distribution between the power input to the pseudo build environment from the electron beam and the heat transferred to the combination of the CP-Ti disk, SS-plate and heat shield as a function of time. In this figure, the solid red line represents the input power, the blue line represents the power absorbed by the CP-Ti disk and the SS-plate, and the green line represents the power absorbed by the heat shield. The hatch lines are the areas under the curves that show energy.

It is observed that at the beginning of the experiment, virtually 100 % of the input power is absorbed by the CP-Ti disk and SS-plate. With increasing time, as the CP-Ti disk and SS-plate heat up and start to radiate, the amount of heat transferred to the heat shield increases. At the steady-state condition, approximately 30 % of the input power is transferred to the CP-Ti disk and SS-plate, and ~70 % to the heat shield. This is an interesting observation and points to the fact that a significant amount of energy input to the system, which is intended to heat the CP-Ti disk, is lost to the heat shield. It is important to point out that this occurs at a maximum CP-Ti disk temperature of ~755 °C. In addition, the energy balance at the end of the simulation shows that 43 % of the total input energy is absorbed by the CP-Ti disk and SS-plate, and 57 % by the heat shield.

Note: the change in the slope of the Input Power curve is due to the change in the gun power, as shown in Figure 4.3 *(a).*

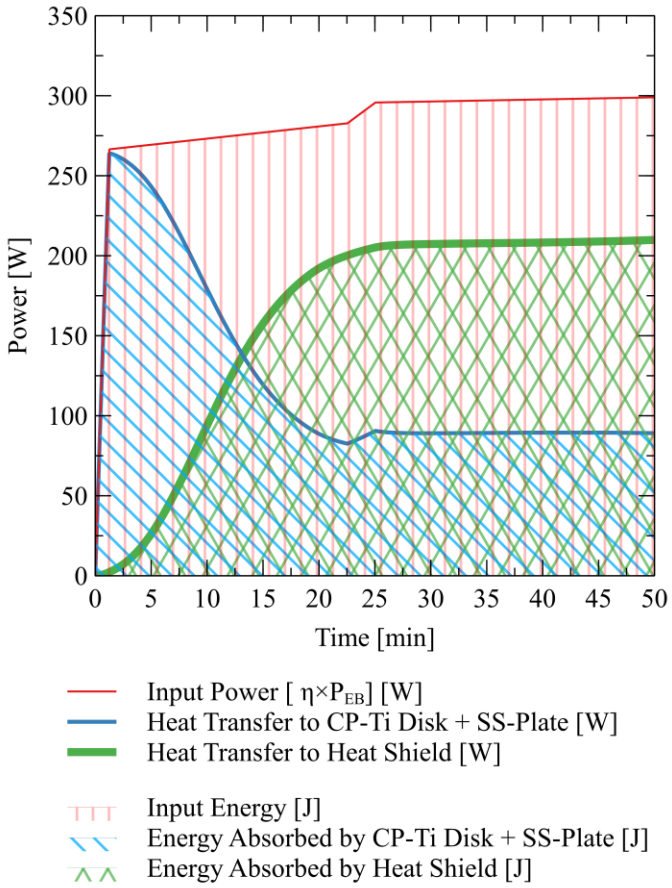

Figure 4.13. The evolution of the partitioning of power and energy between the CP-Ti disk + SS-plate and the heat shield during heating.

4.3.5 Numerical Case Studies

Four heat transfer case studies were conducted to further explore the heat balance in the EB-BF using the numerical model. The case studies were designed to assess the evolution of temperature within the pseudo build environment by adding complexities to the model, such as including heat input associated with a preheat at the beginning of the process, heat input associated with changing heating pattern size, heat loss associated with powder deposition and a short preheat after each powder deposition sequence. The results of these cases are intended to provide guidance for future model development. Figure 4.14 and Table 4.2 show the details for each case study.

A uniform surface heat flux was applied for each preheating sequence, consistent with the beam being rapidly rastered across the surface of the CP-Ti disk. PH0 indicates the initial preheating sequence for Cases 2, 3, and 4, which was 120 s in duration. Additional preheating sequences are indicated as PH1 to PH6 for Cases 3 and 4, each 10 s in duration. The value for the uniform heat flux for each preheating sequence is calculated using Eq. (4.6):

$$q_{PHi} = \frac{\eta P_{EB}}{A_{disk}} \tag{4.6}$$

where q_{PHi} (W m^{-2}) is the uniform surface heat flux of preheating sequence *i*, P_{EB} (W) is the EB power, η is the EB absorption factor, and A_{disk} (m^2) is the surface area for the CP-Ti disk.

The time-averaged Gaussian surface heat flux (refer to Eq. (4.1)) was used as the heat source for each heating pattern (P1 to P6). The surface energy density for each heating pattern was considered constant while the pattern radius decreased from R1 to R6. The mathematical relationship that describes the surface energy density for each heating pattern is presented in Eq. (4.7):

$$E_{P_i} = \frac{\eta P_{EB} t_{P_i}}{A_{P_i}} \tag{4.7}$$

where E_{P_i} (J m^{-2}) is the surface energy density for pattern P_i, t_{P_i} (s) is the beam irradiation time for pattern P_i, and A_{P_i} (m^2) is the surface area for pattern P_i. For a constant surface energy density, the irradiation time for the heating pattern P_{i+1} is calculated when the heating pattern radius changes from R_i to $R_{i+1}$with respect to the ratio between the surface area of these two patterns and the duration of the previous heating pattern (P_i), as shown in Eq. (4.8):

$$t_{P_{i+1}} = t_{P_i} \frac{A_{P_{i+1}}}{A_{P_i}} \tag{4.8}$$

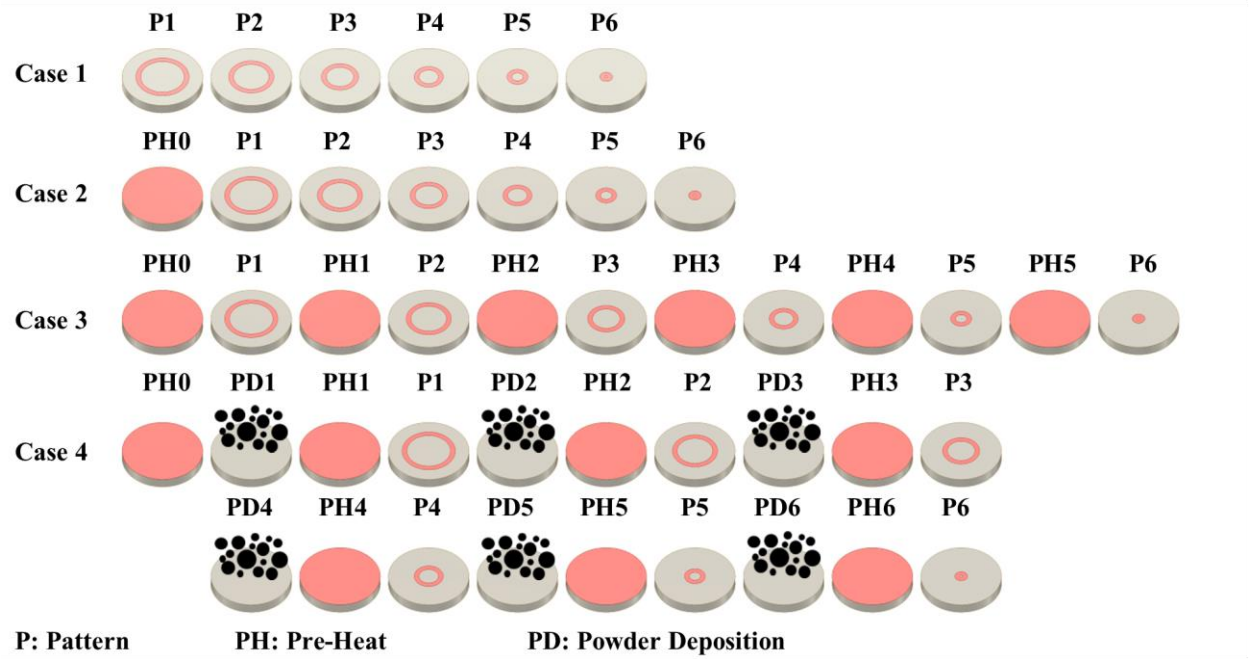

Figure 4.14. Schematic diagram of the case studies.

Table 4.2. Simulation parameters used in the case studies

Simulation Parameter Description			**Pre-Heating**		**Pattern Heating**		**Powder Deposition**	
Parameter	Unit	Value	Cycle	Time [s]	Cycle	Time [s]	Cycle	Time [s]
R1	mm	37.5	PH0	120	P1	60	PD1	5
R2	mm	32.5	PH1	10	P2	52	PD2	5
R3	mm	27.5	PH2	10	P3	44	PD3	5
R4	mm	22.5	PH3	10	P4	36	PD4	5
R5	mm	17.5	PH4	10	P5	28	PD5	5
R6	mm	12.5	PH5	10	P6	20	PD6	5
A_{P1}	mm^2	3534	PH6	10				
A_{P2}	mm^2	3063						
A_{P3}	mm^2	2592						
A_{P4}	mm^2	2121						
A_{P5}	mm^2	1649						
A_{P6}	mm^2	1178						
P_{EB}	W	1500						
η	-	0.65						
σ_{EB}	mm	2.5						
T_{amb}	K	293 to 313						
T_{PL}	K	298						

A uniform negative surface heat flux was defined on the top surface of the CP-Ti disk to implement the thermal energy absorption by the powder layer in Case 4, as presented in Eq. (4.9):

$$q_{PD} = \frac{H_{PD}}{t_{PD} A_{disk}} \tag{4.9}$$

In this equation, q_{PD} (W m^{-2}) is the surface heat flux associated with each powder deposition sequence, t_{PD} (s) is the duration of the powder deposition sequence, and A_{disk} (m^2) is the surface area for the CP-Ti disk. The heat loss associated with the powder deposition sequence (PD1 to PD6 in Case 4) was calculated assuming that each 100 µm thick powder layer of Ti6Al4V was heated up to the average surface temperature of the CP-Ti disk and is estimated using Eq. (4.10):

$$H_{PD} = \phi \rho_s h \pi R_d^2 c_p (\bar{T}_{disk} - T_{powder}) \tag{4.10}$$

where H_{PD} (J) is the enthalpy associated with powder deposition for each layer, ϕ is the powder packing factor, ρ_s (kg m^{-3}) is the density of solid Ti6Al4V, h (m) is the powder layer thickness, R_d (m) is the CP-Ti disk radius, c_p (J kg^{-1} K^{-1}) is the specific heat of solid Ti6Al4V, $\bar{T}_{disk}$ (K) is the CP-Ti disk average surface temperature, and T_{powder} (K) is the powder layer temperature. The powder layer temperature was set to 293 K, and the powder packing factor and specific heat values for Ti6Al4V were taken from previous studies – i.e., ϕ= 0.583 and c_p= 546 J kg^{-1} K^{-1} [73,76]. *Note: since the powder layer temperature was assumed to be 293 K, the density and the specific heat values for Ti6Al4V were defined as temperature invariant.* Figure 4.15 shows the heat absorption by the powder layer with respect to the temperature difference between the CP-Ti disk and the powder layer for six deposition cycles in Case 4.

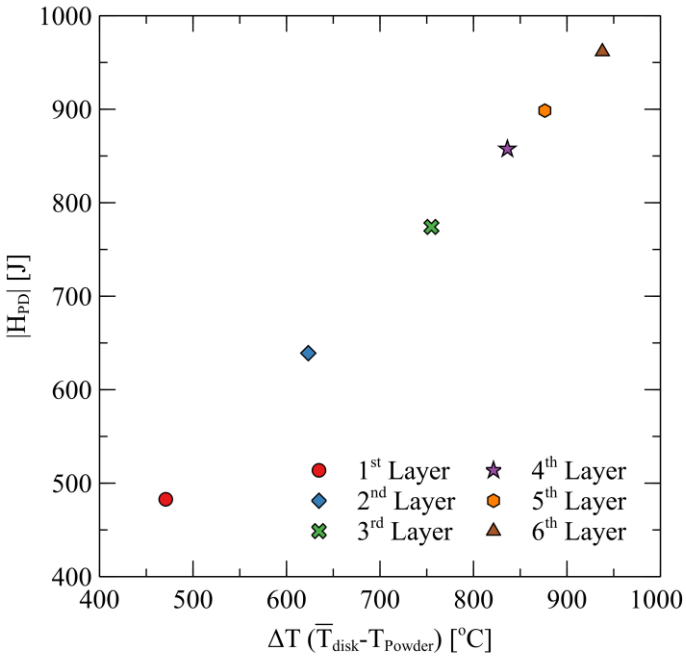

Figure 4.15. The absorbed thermal energy as a function of $\Delta T(\bar{T}_{disk} - T_{Powder})$ for each powder deposition sequence in Case 4.

4.3.5.1 Energy Balances for Different Cases

As previously discussed, one of the surprising findings of the initial look at the model results is that the net energy to the CP-Ti disk and SS-plate decreases within increasing time as they heat up and begin to radiate heat to the heat shield. To further explore this, Figure 4.16 (a) shows the total net heat input (heat input – radiation losses) on the CP-Ti disk's top surface as a function of normalized time for Cases 1 through 4. The highest net input over the duration of the simulation occurs in Case 1, as it receives the least amount of energy resulting in the lowest temperature increase and radiation losses. Adding the initial and subsequent preheating cycles to the base model led to an increase in the overall CP-Ti disk temperature, which increases the radiation heat loss to the heat shield and subsequently decreases the fraction of heat absorption by the CP-Ti disk in Cases 2 to 4. *Note: the initial preheat sequence is 120 s in duration, whereas each subsequent preheat sequence is 10 s in duration.*

The heat loss associated with the powder deposition in Case 4 (due to both "switching" the beam off and the negative flux associated with heating the powder layer) is illustrated by the large, sudden decrease in the net heat flux during each deposition sequence. Once the negative flux is removed, the net heat input rapidly recovers as a preheating sequence begins.

To further assess the energy balance for each case, the fraction of total heat input absorbed by the CP-Ti disk/SS-plate, the heat shield and the powder was calculated and reported as a percentage of the energy input, as shown in Figure 4.16 (b). It can be seen that the amount of heat absorbed by the CP-Ti disk/SS-plate decreases from 87.7 % (Case 1) to 72.4 % (Case 4), while the heat absorbed by the heat shield increases from 12.3 % (Case 1) to 26.5 % (Case 4). The amount of heat absorbed by the powder layer is relatively small and constitutes 1.1 % of the total energy input in Case 4.

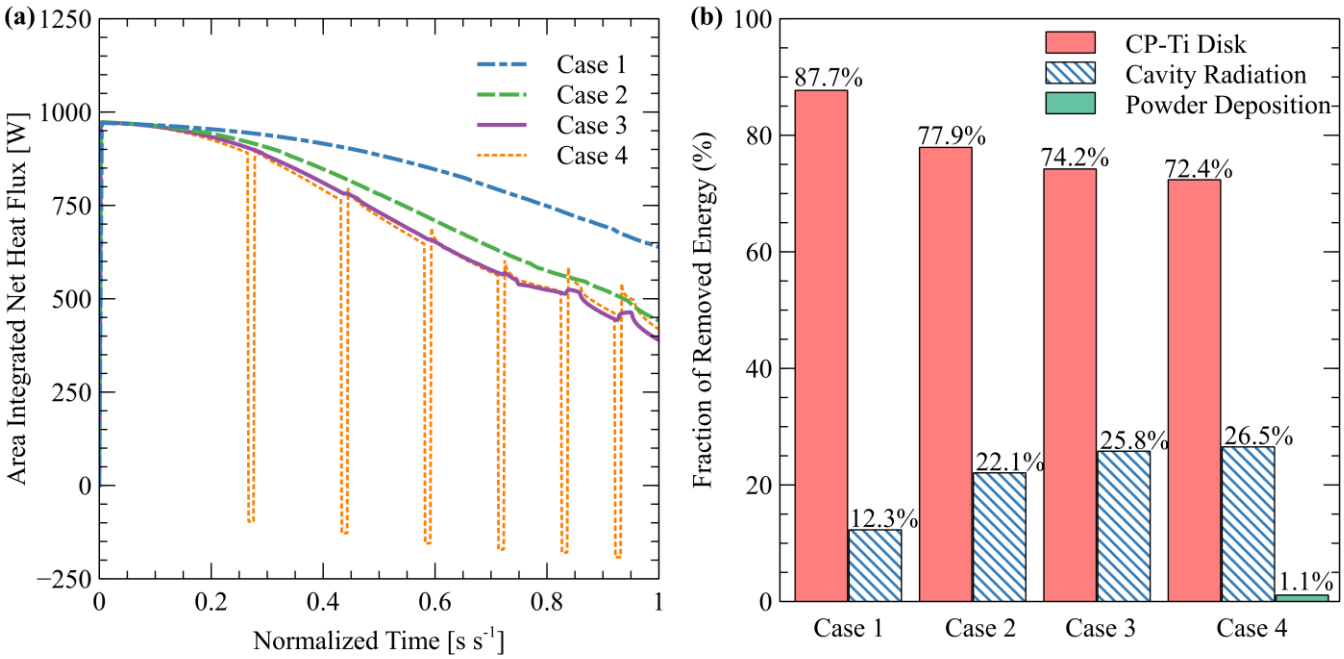

Figure 4.16. (a) The evolution of the area-integrated net heat flux on the CP-Ti disk top surface for the simulation case studies, and (b) the fraction of energy removed by the CP-Ti disk, the cavity radiation and the powder deposition cycles.

4.3.5.2 Temperature Evolution within the Build Environment

Figure 4.17 (a) shows a series of temperature contour plots on a vertical section through the CP-Ti disk at the end of the simulation for Cases 1 to 4. Figure 4.17 (b) shows a series of temperature profiles along with line C-C' at the end of the simulations. As can be seen, and as mentioned previously, implementing the preheating cycles has increased the overall CP-Ti disk temperature (Cases 2 and 3) whereas, adding the cooling effect of powder deposition in Case 4 has reduced the disk temperature in comparison to Case 3.

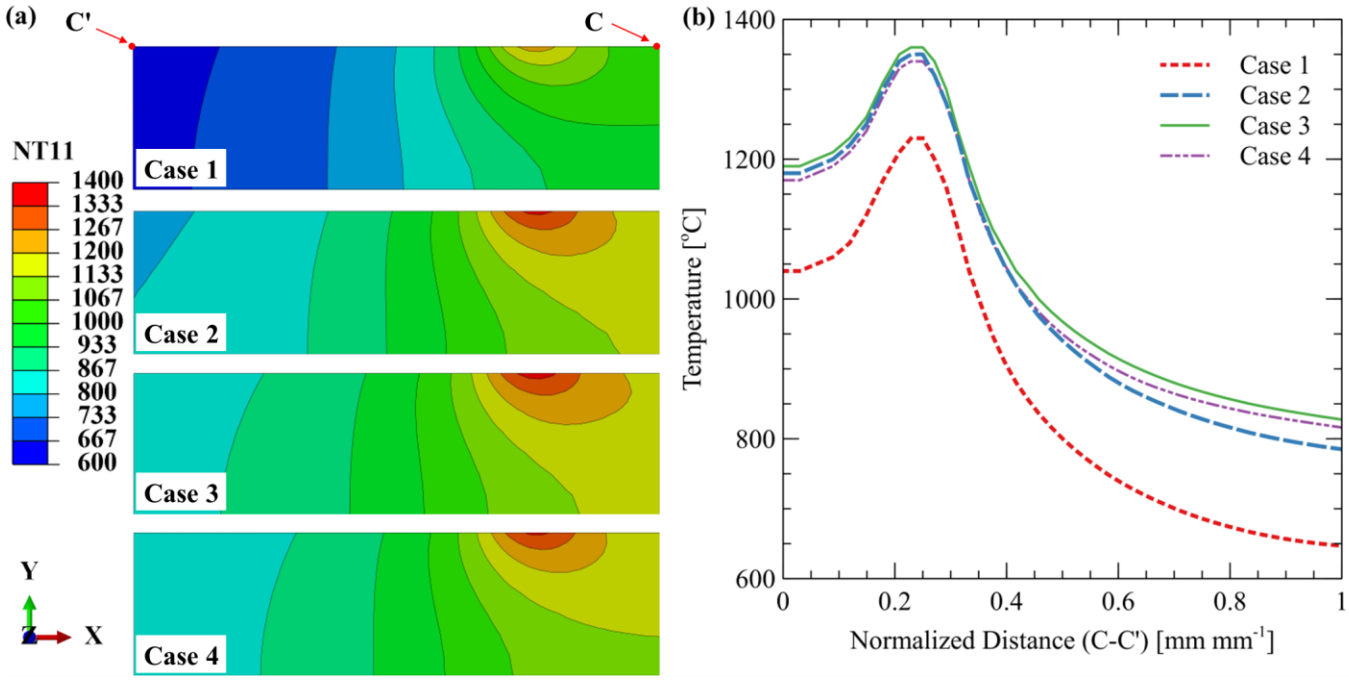

Figure 4.17. (a) The temperature contours of the CP-Ti disk at the end of simulation for Cases 1 to 4, (b) the temperature variation on the CP-Ti disk top surface along line C-C'

Figures 4.18 (a) and (b) show the temperature profiles along lines A-A' and B-B' on the heat shield at the end of the simulation for each case study – see Figure 4.12 (a) for locations of lines A-A' and B-B'. It can be observed that by implementing the preheating cycles, the overall heat shield temperature increases as a result of the higher absorption of radiation from the CP-Ti disc and the SS-Plate. On the other hand, in Case 4, the absorption of heat by the powder during

deposition has not significantly influenced the temperature evolution on the heat shield, as the difference in the temperature distribution in Cases 4 and 3 along lines A-A' and B-B' is less than 4 °C.

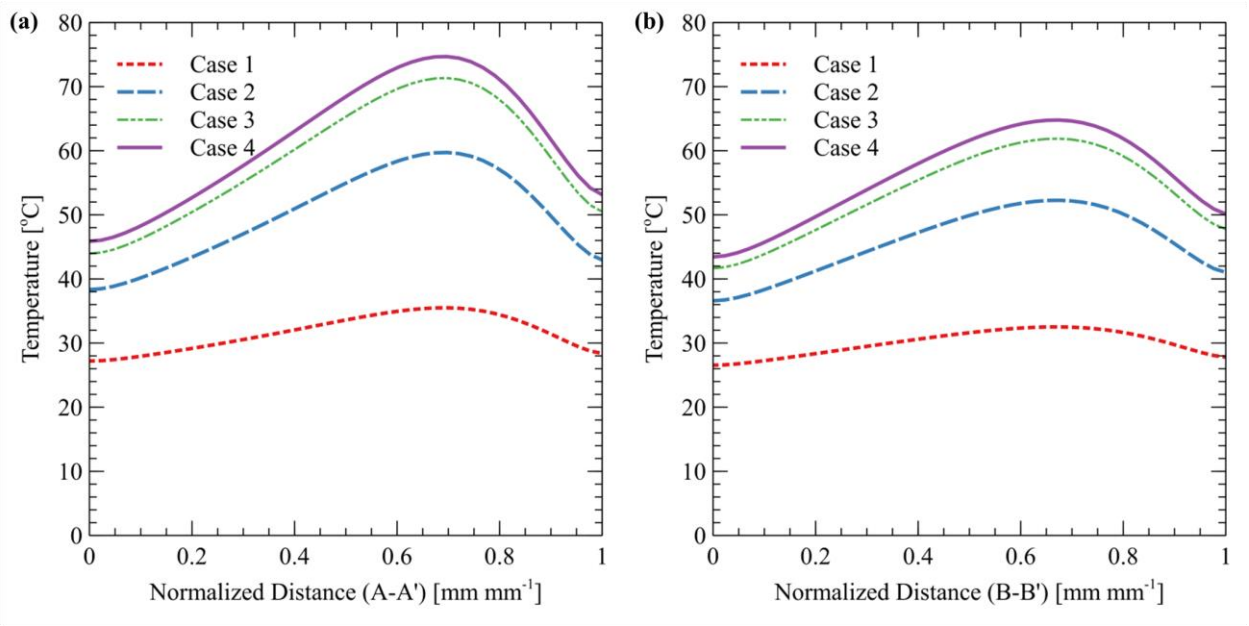

Figure 4.18. (a) The temperature variation on the heat shield along line A-A', and (b) along line B-B'.

4.4 Summary and Conclusions

In this chapter, an experimental set-up was designed and constructed inside a lab-scale EB-BF to represent a pseudo build environment during a simplified electron beam heating experiment. The set-up consisted of the walls of a GE-ARCAM Q20plus heat shield, a CP-Ti disk and SS-plate. A circular beam trajectory pattern was prescribed to heat the CP-Ti disk, while temperature data were obtained from a series of thermocouples located in the CP-Ti disk, the SS-plate, and the heat shield walls during both heating and cooling. A 3D heat transfer model based on the experimental set-up was developed in ABAQUS and was formulated to describe cavity radiation within the pseudo build environment. The model was validated with respect to the temperature data obtained from the EB-BF.

A comparison between the model predictions and the experimentally derived data indicated the model accuracy to be generally within ±10 %. The results of the heating experiment suggest that the radiative heat exchange between various surfaces within the pseudo build environment is complex, as is evident from the model energy balance predictions.

Following the model validation, four numerical case studies were developed to analyse the effect of variable heating pattern sizes, initial preheating, subsequent preheating, and hypothetical powder deposition sequence on the energy balance and the temperature evolution within the pseudo build environment. The case studies results provide a preliminary understanding of the transport of heat within the pseudo build environment, which can be used for future model development.

Chapter 5: Development of autonomous in-situ temperature measurement and logging system

This chapter presents the framework for the design and development of a modular, self-contained, Autonomous In-situ Temperature Measurement and Logging (AITML) system, which is potentially suitable for in-situ instrumentation within a high-vacuum environment. This system is developed in stages, where the system's functionality is evaluated through a series of experimentations under atmospheric conditions and a high-vacuum environment. Throughout the evaluation process, potential drawbacks to the design are identified and considered accordingly. The final design of the AITML system is placed inside the lab-scale EB-BF vacuum chamber for in-situ instrumentation to measure the temperature from the pseudo build environment during the experiment discussed in Chapter 4.

5.1 Experimental Procedure

5.1.1 Instrument Design and Development

The AITML system consists of three main elements: i) electronics, ii) a power source, and iii) a hermetic enclosure and mechanical parts. Figure 5.1 shows a high-level schematic diagram of this instrument.

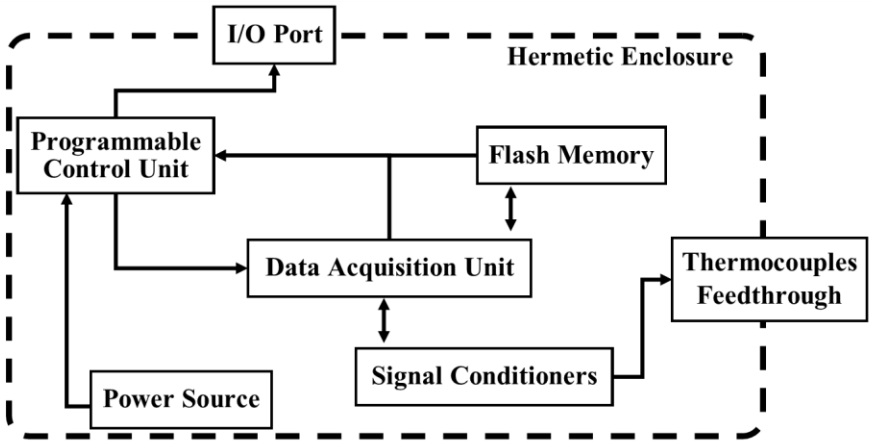

Figure 5.1. A high-level schematic diagram of the AITML system.

The AITML system is equipped with a DI-4718B data acquisition and logger unit from DATAQ INSTRUMENTS, which is an eight-channel instrument designed for data logging applications, where signal conditioning modules are required. Model DI-4718B features a 12 to 16-bit analogue-to-digital resolution as a function of sample rate – i.e., lower sampling rate results in higher resolution readings. This unit can operate in two modes:

i) Standard mode where the data is transferred to a computer via USB cable; and

ii) Stand-alone mode where the data is stored on a USB flash storage.

The maximum analogue sampling rate of this unit is 160 kHz, which depends on the mode of operation and the USB flash storage. Furthermore, it has a remote-control feature allowing a user to stop/start, record, and mark events during data acquisition. Further details about this unit can be found in the user manual published by DATAQ INSTRUMENTS [77].

Four DI-8B47K thermocouple modules from DATAQ INSTRUMENTS were chosen as the signal conditioning modules. These thermocouple modules amplify, isolate, and linearise the input from a type-K thermocouple. In addition, these units have low-pass noise filtration with automatic corner frequency selection and provide analogue voltage output of 0 V to +5 V for further signal processing. Each module has a built-in Cold Junction Compensation (CJC) to correct for the thermoelectric voltage formed at the thermocouple wire and screw terminals on the mounting panel. The signal conditioning module has electrically isolated the data acquisition unit from the thermocouple wires through optical coupling. This isolation barrier protects the data acquisition unit from electrical surges that may occur while operating the EB gun. Further details about the signal conditioning modules can be found in a datasheet published by DATAQ INSTRUMENTS [78].

Note: a preliminary temperature measurement system was developed prior to the AITML system, as presented in Appendix A. The limitations with the preliminary system led to including the signal conditioning modules and purchasing the model DI-4718B data acquisition unit with four DI-8B47K thermocouple modules from DATAQ INSTRUMENTS.

As shown in Figure 5.1, a programmable control board was designed to operate and control the AITML system functionalities. The Printed Circuit Board (PCB) for the control board was designed in KiCad. The PCB was fabricated off-campus, and all the electronic components of this board were hand soldered. The control board is based on the ATMEGA 2560 microcontroller (i.e., Arduino Mega), as schematically shown in Figure 5.2 (a). Figure 5.2 (b) shows the PCBs fabricated for the control board and the detachable remote control during testing. It is programmed through the open-source Arduino Integrated Development Environment (IDE) to perform six key tasks:

i) Connecting the internal electronics to the peripheral port for system configuration;

ii) Data retrieval;

iii) Checking the battery charge level;

iv) Starting data acquisition at a predefined time;

v) Recording and marking events during data acquisition;

vi) Stopping and switching off the data acquisition unit after a predefined duration; and

vii) Monitoring the AITML system's internal temperature and pressure during the operation.

The control board measures the internal temperature and pressure from the MPL115A1 sensor on the board (see Figure 5.2). If the temperature or pressure exceeds a defined criterion, the control board marks the event and performs an emergency shut down to protect the internal electronics.

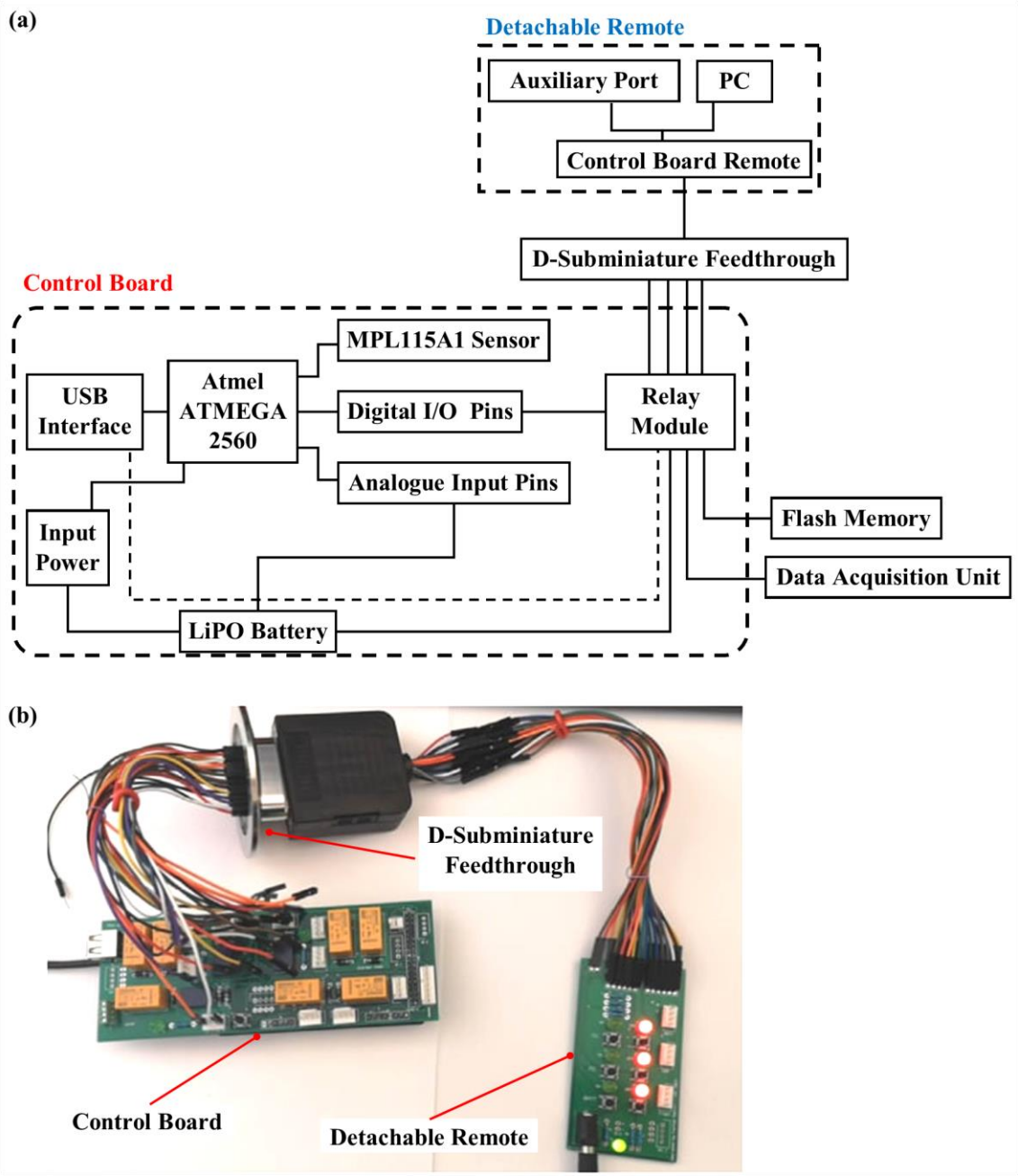

Figure 5.2. (a) A high-level schematic diagram of the control board in the AITML system, and (b) the fabricated PCBs for the control board and the detachable remote.

Since the LiPO battery and some electronic components in the AITML system can operate in an environment with specific minimum air pressure, and the issues with heat dissipation from the electronics operating in a vacuum environment, a low-profile and square-shaped hermetic enclosure was designed to protect these elements from the high-vacuum environment presents in

an EB-based machine, as shown in Figure 5.3. The enclosure was fabricated from the AA6061-T6 billet. Two ports were designed on the enclosure to connect the thermocouple feedthrough and the peripheral port to the interior electronics. The sealing mechanism in this design is based on compressing a Fluorocarbon (FKM) O-ring between the sealing interfaces. In addition, two overpressure rings were added to the assembly to improve the sealing performance at each port. The overpressure ring limits the expansion of the O-ring when the internal pressure is greater than the external or the contact pressure, leading to improved sealing at ports A and B interfaces. Finally, a 12.5 mm thick alumina fibre blanket can be fitted inside the enclosure to thermally isolate the electronics and the battery pack from the enclosure if the system is placed inside a high-temperature environment. *Note: Appendix B presents a step-by-step approach to designing the hermetic enclosure in greater detail.*

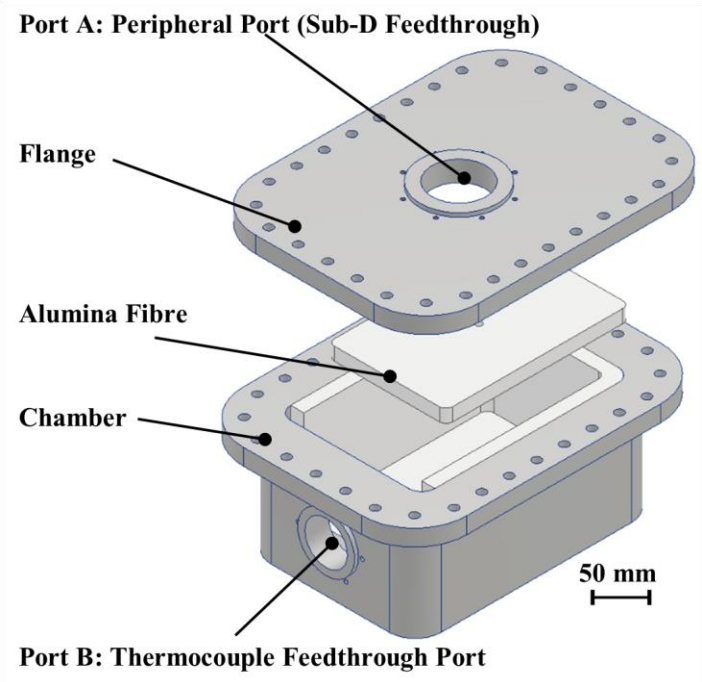

Figure 5.3. 3D CAD rendering of the square-shaped enclosure designed for the AITML system.

Figure 5.4 shows a 3D CAD rendering of the AITML system. This system can operate in a high-vacuum environment and record temperature from four type-K thermocouples in a

stand-alone mode. The recorded temperature data is stored on a USB flash memory and can be retrieved by connecting a computer to the peripheral port once the instrument is removed from the vacuum chamber of an EB-based machine.

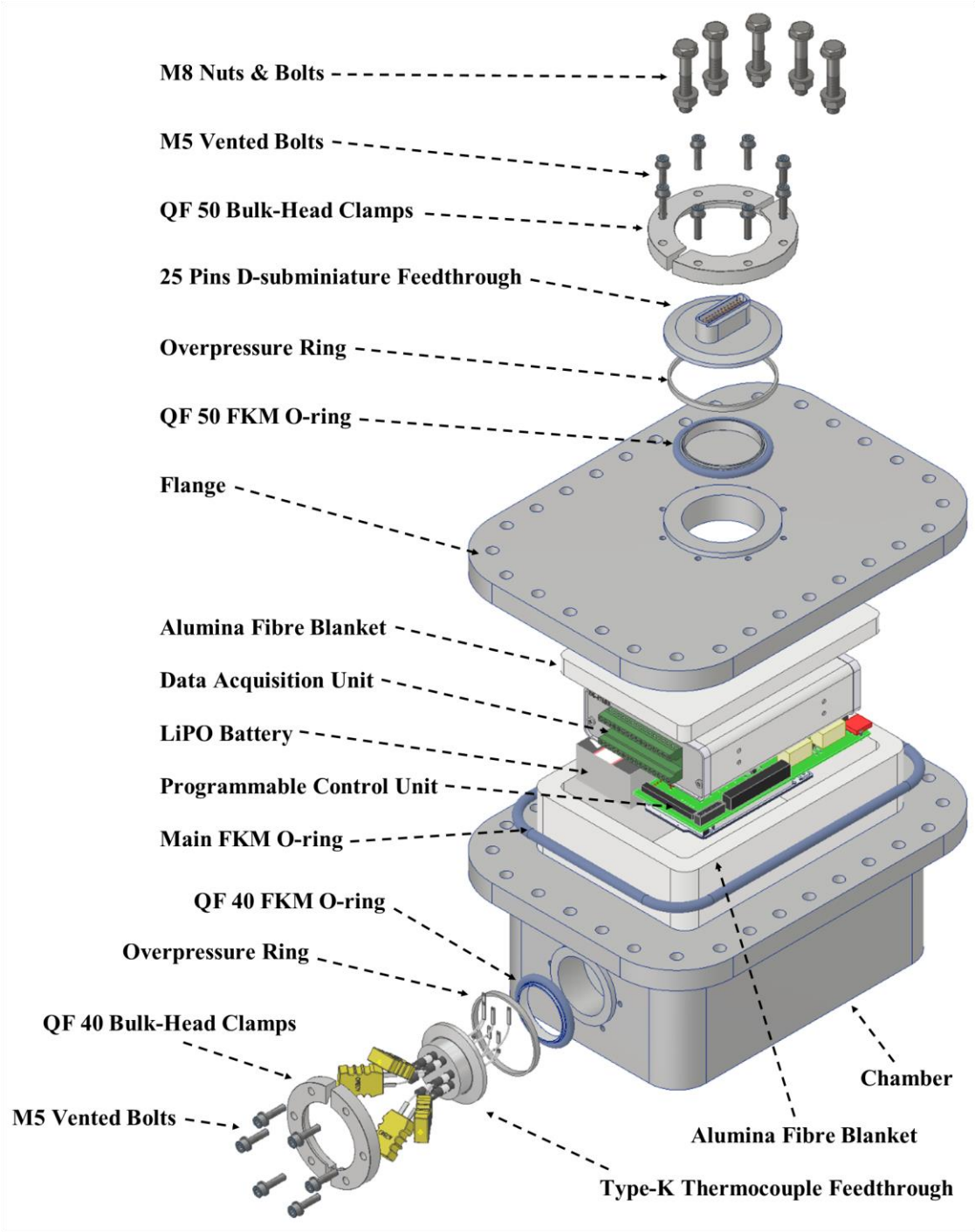

Figure 5.4. 3D CAD rendering of the AITML system's components.

5.1.2 Overpressure and Vacuum Experiments

The AITML system is designed to operate inside a vacuum chamber; therefore, the instrument's enclosure must protect the internal electronics against this environment. To evaluate the hermetic enclosure's sealing performance, the enclosure's internal pressure was tested in the three conditions presented in Table 5.1.

First, an overpressure experiment was designed to evaluate the sealing of the hermetic enclosure in atmospheric conditions, as shown in Figure 5.5 (a). In this test, the assembled enclosure (without the electronics) was filled with Argon gas with a pressure of approximately 1 bar above the atmosphere, and the change in the internal pressure was measured over 72 h.

In addition to the overpressurised condition, the enclosure's internal pressure was measured under two vacuum conditions described in Table 5.1. First, an MPL115A1 sensor (see Figure 5.2) was placed inside the enclosure and was connected to the D-subminiature feedthrough. Then the assembled enclosure was placed inside the EB-BF vacuum chamber. A wire harness from a feedthrough installed on the EB-BF was connected to the D-subminiature feedthrough on the enclosure to connect the control board outside the EB-BF to the MPL115A1 sensor within the hermetic enclosure. Finally, the vacuum chamber was pumped down to the desired vacuum range and maintained in the specified vacuum pressure range during each experiment, and the MPL115A1 sensor measured the enclosure's internal pressure with respect to time. A Python script was used to record and visualise the real-time pressure change during these experiments, as presented in Appendix E.

Note: the battery and other electronics (i.e., the data acquisition unit, signal conditioning modules and the programmable control board) were not included in the assembly during the

vacuum experiments. The reason was to protect these components against potential damage if the internal pressure was dropped significantly during the experiments.

Table 5.1. Details of the overpressure and vacuum experiments

Experiment Description	Test Duration	Code Name
1. Overpressure test:		
Initial absolute pressure in the enclosure: 2013.1 mbar	72 h	EXP-OP1
Initial absolute pressure in the enclosure: 2023.7 mbar	72 h	EXP-OP2
2. Medium-vacuum test:		
Initial absolute pressure in the enclosure: 1013.2 mbar Vacuum chamber target pressure: ~ 10^{-1} to 1 mbar	35 h	EXP-MV1
3. High-vacuum test:	4.5 h	EXP-HV1
Initial absolute pressure in the enclosure: 1013.2 mbar Vacuum chamber target pressure: ~ 10^{-6} to 10^{-5} mbar	12.5 h	EXP-HV2

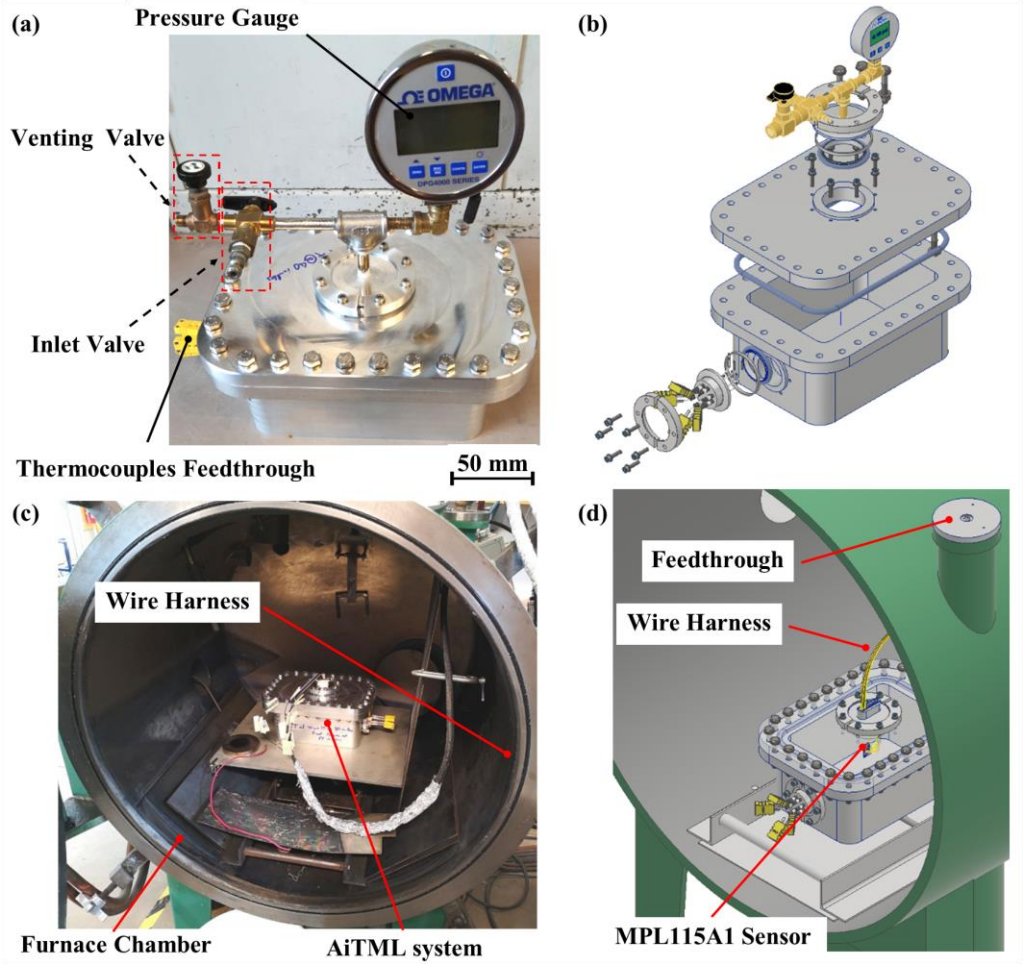

Figure 5.5. The experimental set-up for measuring pressure change during (a) the overpressure experiments and (c) the vacuum experiment. A 3D CAD rendering of (b) the exploded view of the overpressure set-up and (d) the vacuum experiments.

5.1.3 Electron Beam Heating Experiment

The functionality of the AITML system was examined through a simple heating experiment within the EB-BF, as shown in Figure 5.6 (a). The heating experiment involved generating a circular beam trajectory pattern, and heating a commercially pure titanium (CP-Ti) disk, with dimensions of 96 mm × 13 mm ($\emptyset \times H$), as shown in Figure 5.7. The alumina fibre blanket was removed from the enclosure to evaluate the influence of environment on the temperature inside the AITML system during this experiment. However, a small rectangular protective plate was placed between the instrument's enclosure and the experimental set-up (i.e., the CP-Ti disk and the SS-plate) to protect the AiTML system from direct exposure to thermal radiation.

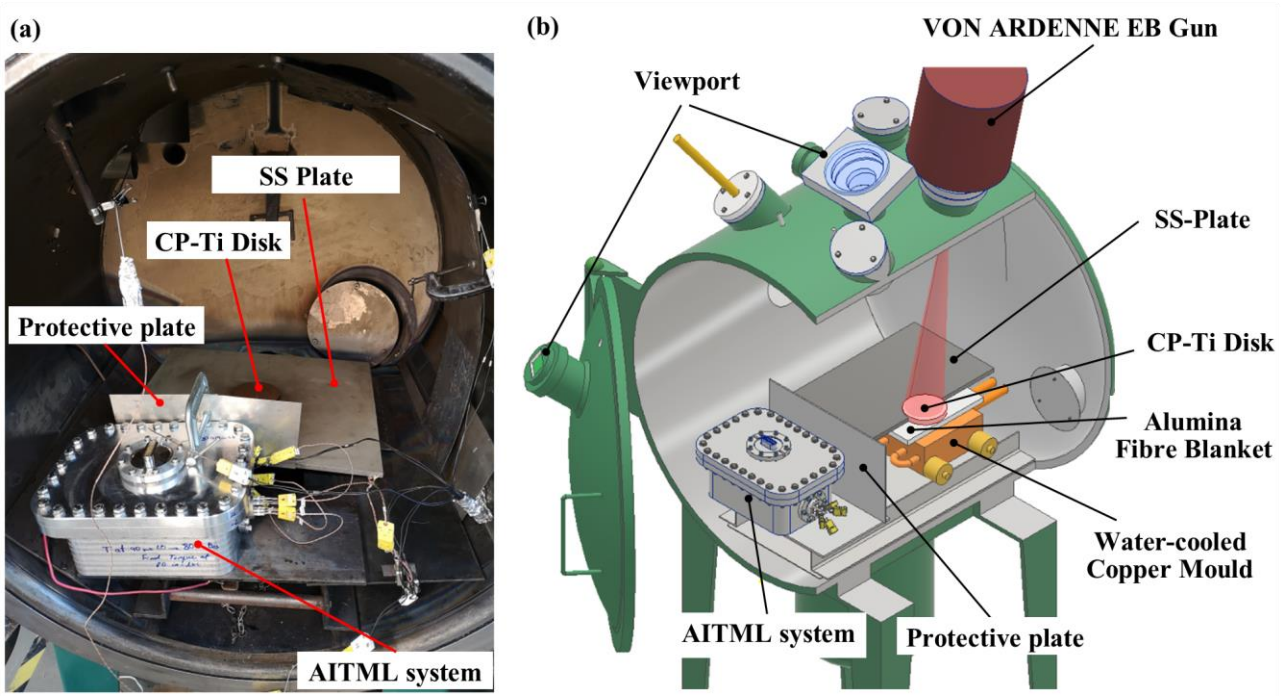

Figure 5.6. The experimental set-up for the heating experiment showing (a) the front view and (b) a 3D CAD rendering of the set-up.

The overall performance of the AITML system was evaluated in this experiment while operating the EB gun for 30 min. Figure 5.7 shows the circular beam trajectory pattern during heating. The beam scan frequency was set to 20 Hz and the power was ramped up to a maximum of 850±25 W over 25 minutes and was ramped down over 5 minutes. It should be noted that the

AITML system's control board was configured to record the enclosure's internal temperature and pressure during this experiment.

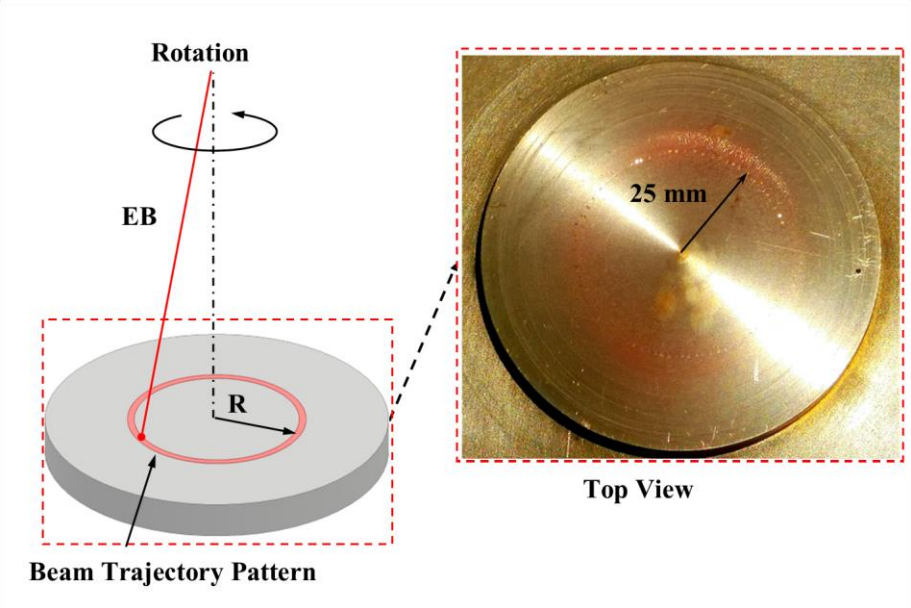

Figure 5.7. The circular beam trajectory pattern during the heating experiment.

5.2 Results and Discussion

5.2.1 The Overpressure Experiments

Figure 5.8 shows the hermetic enclosure's internal pressure during the overpressure experiments. The results show that the internal pressure decreased ~11 % and ~12 % during the EXP-OP1 and the EXP-OP2 experiments, respectively. The overpressure results show that the hermetic enclosure could withstand the pressurised condition with a maximum pressure change of ~ 122±1 mbar over 72 h.

Note: the decrease in the internal pressure is due to the total gas leak from both the hermetic enclosure and the tubing connections in the experimental set-up, as shown in Figure 5.5 *(a). Furthermore, the reported measurement error of the pressure gauge shown in Figure* 5.5 *(a) is within ±10 % of the full-scale pressure range (~1.0 mbar).*

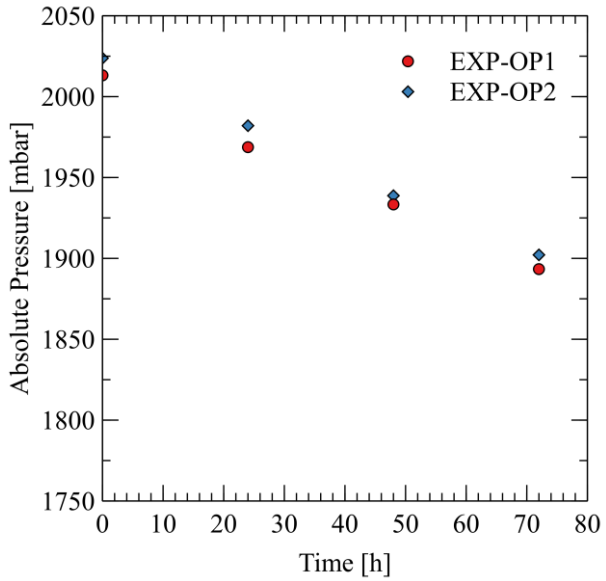

Figure 5.8. The evolution of internal pressure during the overpressure experiments.

5.2.2 Vacuum Experiments

Figure 5.9 shows the enclosure's internal pressure change during the medium-vacuum experiment (refer to Table 5.1). The control board was configured to operate for 35 h and record the internal pressure at 1 h intervals. According to this figure, the internal pressure was changed by ~39 mbar throughout the experiment. A linear extrapolation shows that the internal pressure can change up to ~80 mbar if the enclosure is held in a medium-vacuum environment for 72 h.

Note: the extrapolated pressure change in this experiment is ~40 mbar lower than the maximum pressure change evaluated in the overpressure experiment after 72 h. This is due to the total gas leak from the experimental set-up in the overpressure experiments, as discussed previously.

The result of this experiment shows that the internal pressure was above the battery's air pressure limit – i.e., air pressure above 116 mbar as specified by the manufacturer. It should be noted that the MPL115A sensor measures the absolute pressure within ~±10 mbar accuracy (for a pressure range between 500 mbar to 1150 mbar).

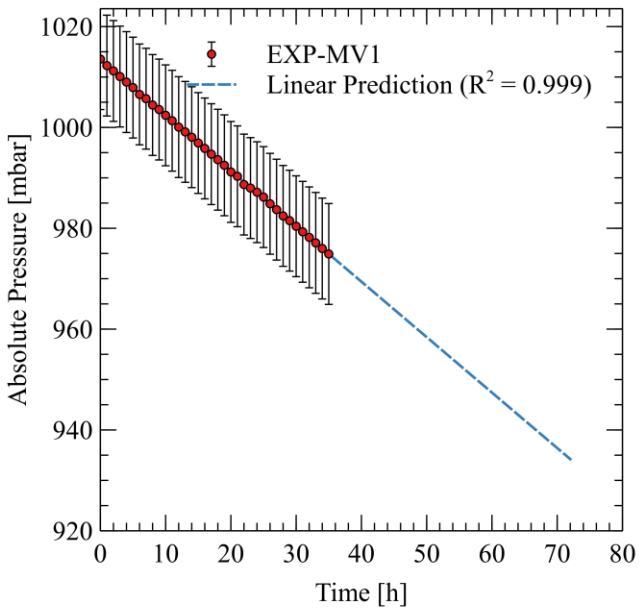

Figure 5.9. The evolution of enclosure's internal pressure during the medium-vacuum experiment.

Figure 5.10 (a) and (b) show the evolution of internal pressure during the high-vacuum experiments. It is observed that the internal pressure was changed by ~8 mbar and ~21.5 mbar throughout the EXP-HV1 and the EXP-HV2 experiments, respectively. Both results indicate that the internal pressure was above the battery's air pressure limit – i.e., ~116 mbar.

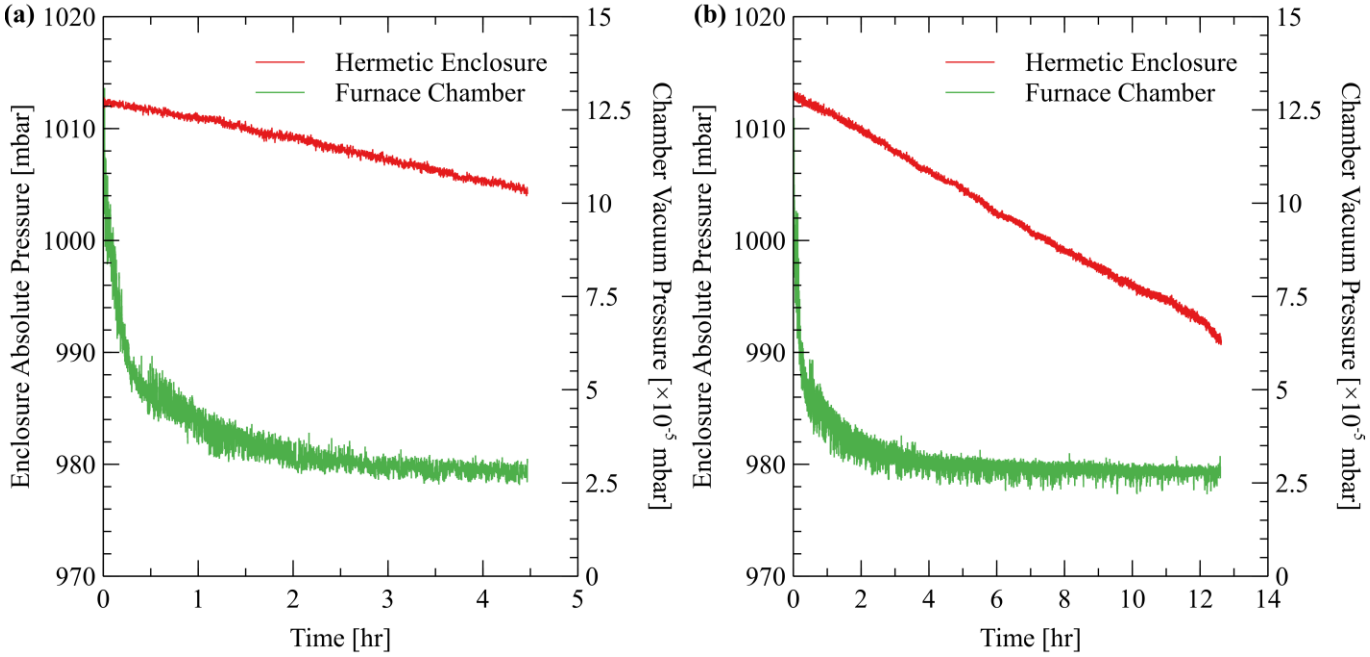

Figure 5.10. The evolution of the internal pressure during the high-vacuum experiments for (a) 4.5 h, and (b) 12.5 h

5.2.3 Heating Experiment

Figure 5.11 shows the evolution of the enclosure's internal pressure and temperature during three events in the heating experiment: i) pumping the furnace vacuum chamber (Zone I), ii) the electron beam heating (Zone II), and iii) cooling (Zone III).

In Zone I, the AITML system's internal pressure decreased ~4 mbar. *Note: The difference between the measured pressure falls within the accuracy of measurement by the MPL115A1 sensor – i.e., ~±10 mbar for a pressure range between 500 mbar to 1150 mbar.* Since the furnace vacuum chamber is water-cooled, the radiative heat transfer between the vacuum chamber's internal surfaces and the enclosure resulted in a ~0.75 °C decrease in the enclosure's internal temperature over ~150 minutes. *Note: This sensor can output temperature data from -40 ℃ to 105 ℃. However, the accuracy of the measurement is not provided by the manufacturer.*

In Zone II, the EB gun is switched on for 30 minutes to heat the CP-Ti disk using the simple beam trajectory pattern shown in Figure 5.7. At this time, the control board started the data acquisition unit to operate for 30 minutes. As a result, the internal temperature increased by ~0.6 °C as captured by the sensor, which is related to the heat generated by the signal conditioning modules and other electronics. The increase in the internal temperature led to a slight increase in the internal pressure.

In Zone III, the EB gun is switched off, and the control board turned off the data acquisition unit. Therefore, heat generated by the internal electronics was absorbed and dissipated by the enclosure, which resulted in a decrease in the internal temperature. Since the furnace vacuum chamber was under vacuum during cooling, a further decrease in the internal pressure of the enclosure was observed, as expected. *Note: Both internal pressure and temperature of the*

enclosure fall within the safe range for the battery and electronics to function – e.g., pressure > 116 mbar, temperature < 50 ℃.

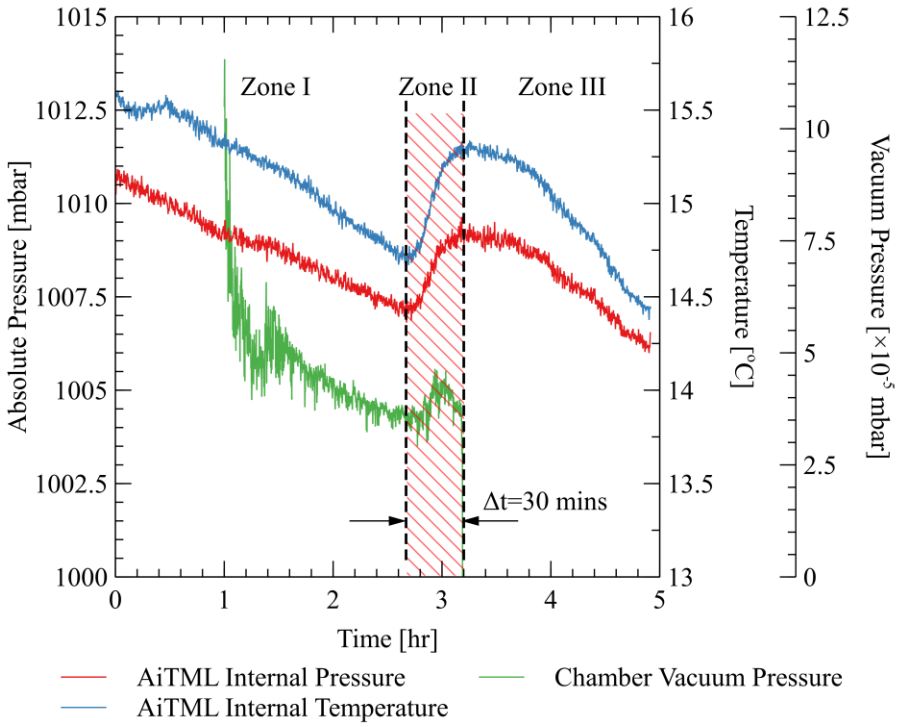

Figure 5.11. The evolution of the AITML system's internal pressure and temperature during the heating experiment in the EB-BF.

A separate experiment was performed on the AITML system to assess the evolution of internal temperature while the system operated for 30 minutes under atmospheric conditions. For this experiment, the alumina fibre blanket was included in the enclosure to thermally isolate the enclosure and capture heat generated by the electronics. Figure 5.12 shows the evolution of temperature during this experiment. Since the assessment was conducted under atmospheric conditions, the internal pressure remained constant at ~1013±10 mbar. The internal temperature (initially at ~20 °C) increased by ~4 °C over 30 minutes. At the end of the experiment, it was observed that the signal conditioning modules were relatively warmer than other electronic elements within the enclosure. *Note: The data acquisition unit can operate up to a temperature of 50 ℃, while the maximum temperature for the signal conditioning module is 85 ℃.*

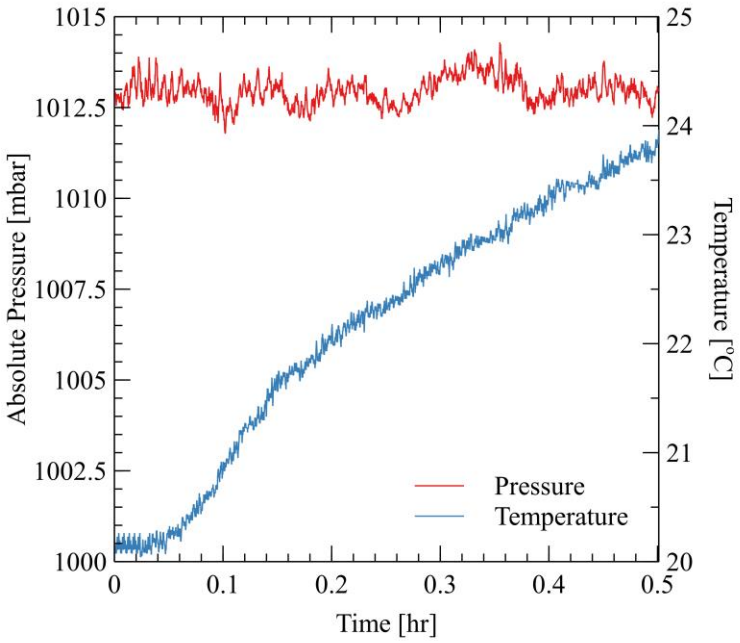

Figure 5.12. The evolution of the AITML system's internal pressure and temperature under atmospheric conditions while including the alumina fibre blanket in the enclosure.

5.3 Summary and Conclusions

In this chapter, an autonomous data acquisition system was designed and developed for in-situ instrumentation to record the in-process temperature. The design is modular, self-contained and electrically and thermally isolated, and can withstand a high-vacuum environment with a limited change in the internal pressure over time. The AITML system was evaluated functionally through a series of experiments conducted under atmospheric conditions and a vacuum environment within the EB-BF. Overall, the AITML system can operate in a stand-alone mode and has the potential to be implemented in a vacuum chamber of an EB-based machine for in-situ instrumentation.

Chapter 6: Summary, conclusions, limitations and for future work

6.1 Summary and conclusions

In this research, a 3D heat transfer model, incorporating cavity radiation, was developed in ABAQUS to characterise the thermal field within a pseudo build environment during heating and cooling of a titanium disk in the absence of powder. To validate the numerical model, an experimental set-up was constructed in a lab-scale EB-BF using a GE-ARCAM Q20Plus heat shield without the top plate, a stainless-steel plate and a titanium disk to present the pseudo build environment. The experimental set-up was instrumented with multiple type-K thermocouples to record the evolution of temperature during the experiment. In addition, a modular, self-contained, in-situ temperature measurement system was designed and developed for in-situ instrumentation within the vacuum chamber of the EB-BF. Finally, four numerical case studies were developed to evaluate the influence of changing heating pattern size, including initial and subsequent preheating cycles and heat absorption by the powder deposition sequence on the evolution of temperature within the pseudo build environment. According to work described above, it was concluded that:

1. A comparison between the model predictions and the experimentally derived data indicated the model accuracy to be generally within ±10 %.
2. The results of the heating experiment suggest that the radiative heat exchange between various surfaces within the pseudo build environment is complex, as is evident from the model energy balance predictions. The numerical model results revealed that at the end of the simulation, the total thermal energy absorbed by the CP-Ti disk + SS plate was 43% of the total energy input, whereas the heat absorbed by the heat shield constituted 57%. At a steady-state (with a peak CP-Ti disk temperature of ~755 °C), ~30 % of the input power was transferred to the CP-Ti disk and SS-plate, and ~70 % to the heat shield.

3. The numerical case studies indicate that including model complexities, such as changing the heating pattern size, including preheating cycles and considering powder deposition sequence, can influence the energy balance (input energy – heat losses) and evolution of temperature within the pseudo build environment. These case studies provide preliminary insight into future model development that can potentially characterise the thermal field within the build environment during an actual EB-PBF process.
4. The overall performance of the AITML system showed that the system could operate in a stand-alone mode under a high-vacuum environment (with a reasonable change in the internal pressure of the hermetic enclosure) and acquire temperature data. The enclosure's internal temperature and pressure are within a safe range specified for the battery and electronics – i.e., internal pressure > 116 mbar and 0 °C < T < 50 °C.
5. The modular, compact design and pressure-proof enclosure make the AITML system potentially suitable for in-situ instrumentation within a high-vacuum environment of an EB-based machine.

6.2 Limitations

It is recognised that the present research has limitations in terms of both experimental work and numerical modelling. The experimental set-up constructed in the lab-scale EB-BF presents a simplified build environment of a commercial EB-PBF system. This means that the presence of the powder hoppers, the top plate of the heat shield, the secondary heat shield, and other parts within the build chamber of a commercial EB-PBF system are not included in the experimental set-up proposed in this study, as mentioned in Chapter 4. In addition, the dimensions and the material for the build platform are different from an actual EB-PBF system. Furthermore, the vacuum chamber of the EB-BF is water-cooled, which influences the heat dissipation from the

experimental set-up. Therefore, it is anticipated that the transport of heat within this experimental set-up is different from the build environment of an EB-PBF system.

Although the numerical model predictions are in good agreement with the experimental work, similar limitations associated with the experimental set-up can be considered for the numerical model. It is expected that the energy balance (input heat to the system – heat losses) predicted by this model would be different compared to a model based on the build environment of an EB-PBF system. In addition, the numerical case studies are based on conditions that are different from an actual EB-PBF process; for instance, the heat absorption by the powder layer (in Case 4) was considered based on the enthalpy associated with the powder deposition sequence. However, these numerical cases were intended to provide preliminary insight into future model development that can potentially characterise the thermal field within the build environment during an actual EB-PBF process.

6.3 Future work

In the present research, the evolution of the macro thermal field within a pseudo build environment was evaluated using a simple beam trajectory pattern and in the absence of powder. There are limitations with the present work, as discussed in the previous section. Therefore, further work is recommended in the following areas:

1. Developing an experimental set-up considering the complexities that are missing from the current set-up.
2. Prescribing complex beam trajectory patterns during the heating experiment and evaluating the evolution of temperature within the build environment.
3. Including the powder deposition sequence in the experiment and evaluating its effect on the evolution of temperature within the build environment.

4. In support of further model development, a model based on the actual build environment of an EB-PBF system can be developed, and a powder bed with the thermophysical properties of Ti6Al4V powder should be included in the model domain. This would help characterise the thermal field and evolution of temperature within the build environment during the operation of a commercial EB-PBF system.

Bibliography

[1] 7.5% growth in AM despite pandemic, Met. Powder Rep. 76 (2021) 216. https://doi.org/10.1016/j.mprp.2021.06.024.

[2] R. Leering, 3D printing's post-pandemic potential, (2021). https://think.ing.com/reports/3d-printings-post-pandemic-potential/.

[3] W. Bonvillian, Advanced Manufacturing: A New Policy Challenge, Ann. Sci. Technol. Policy. 1 (2017) 1–131. https://doi.org/10.1561/110.00000001.

[4] S. Ford, M. Despeisse, Additive manufacturing and sustainability: an exploratory study of the advantages and challenges, J. Clean. Prod. 137 (2016) 1573–1587. https://doi.org/10.1016/j.jclepro.2016.04.150.

[5] M. Baumers, P. Dickens, C. Tuck, R. Hague, The cost of additive manufacturing: machine productivity, economies of scale and technology-push, Technol. Forecast. Soc. Change. 102 (2016) 193–201. https://doi.org/10.1016/j.techfore.2015.02.015.

[6] L.-C. Zhang, Y. Liu, S. Li, Y. Hao, Additive Manufacturing of Titanium Alloys by Electron Beam Melting: A Review, Adv. Eng. Mater. 20 (2018) 1700842. https://doi.org/10.1002/adem.201700842.

[7] R.G. Bruce, Modern materials and manufacturing processes, Prentice Hall, (2004).

[8] C. Arnold, C. Körner, In-situ electron optical measurement of thermal expansion in electron beam powder bed fusion, Addit. Manuf. 46 (2021) 102213. https://doi.org/10.1016/j.addma.2021.102213.

[9] L. Yang, K. Hsu, B. Baughman, D. Godfrey, F. Medina, M. Menon, S. Wiener, Additive Manufacturing of Metals: The Technology, Materials, Design and Production, Springer, (2017).

[10] T. DebRoy, H.L. Wei, J.S. Zuback, T. Mukherjee, J.W. Elmer, J.O. Milewski, A.M. Beese, A. Wilson-Heid, A. De, W. Zhang, Additive manufacturing of metallic components – Process, structure and properties, Prog. Mater. Sci. 92 (2018) 112–224. https://doi.org/10.1016/j.pmatsci.2017.10.001.

[11] J.O. Milewski, Additive Manufacturing of Metals, Springer International Publishing, Cham, (2017). https://doi.org/10.1007/978-3-319-58205-4.

[12] ISO/ASTM 52910: 2018 (E), Additive manufacturing–design–requirements, guidelines and recommendations, (2018).

[13] R. Dehoff, S. Babu, Characterization of interfacial microstructures in 3003 aluminum alloy blocks fabricated by ultrasonic additive manufacturing, Acta Mater. 58 (2010) 4305–4315.

[14] H. Schultz, Electron beam welding, Woodhead Publishing, (1993).

[15] K.H. Steigerwald, G. Sayegh, D. Powers, R. Bakish, O.K. Nazarenko, W. Dietrich, H. Irie, D. Wyatt, An international history of electron beam welding, Pro-beam, (2007).

[16] M.St. Węglowski, S. Błacha, A. Phillips, Electron beam welding – Techniques and trends – Review, Vacuum. 130 (2016) 72–92. https://doi.org/10.1016/j.vacuum.2016.05.004.

[17] M. Chaturvedi, Welding and joining of aerospace materials, Woodhead publishing, 2020.

[18] F. VRÁBLÍK, U. CLAUßb, P. STOLAŘ, Electron Beam Welding–A key technology to construct vehicles for road, rail, sea, air and space, in: Proc. 19th Int. Conf. Metall. Mater. Roznov Pod Radhostem TANGER Ltd, Rožnov pod Radhoštěm, Czech Republic, (2010): pp. 590–595.

[19] U. Ljungblad, Method and apparatus for additive manufacturing, US20150004045A1, (2015). https://patents.google.com/patent/US20150004045A1/en (accessed May 15, 2020).

[20] S. Stecker, P. Wollenhaupt, Process for layer manufacturing a three-dimensional work piece using scanning electron monitored with closed loop control, EP2498935B1, (2015). https://patents.google.com/patent/EP2498935B1/en (accessed May 15, 2020).
[21] C. Körner, Additive manufacturing of metallic components by selective electron beam melting — a review, Int. Mater. Rev. 61 (2016) 361–377. https://doi.org/10.1080/09506608.2016.1176289.
[22] D.N. Trushnikov, Using the wavelet analysis of secondary current signals for investigating and controlling electron beam welding, Weld. Int. 27 (2013) 460–465. https://doi.org/10.1080/09507116.2012.715932.
[23] S. Negi, A.A. Nambolan, S. Kapil, P.S. Joshi, M. R., K.P. Karunakaran, P. Bhargava, Review on electron beam based additive manufacturing, Rapid Prototyp. J. 26 (2019) 485–498. https://doi.org/10.1108/RPJ-07-2019-0182.
[24] Y. Tang, Y.F. Zhao, A survey of the design methods for additive manufacturing to improve functional performance, Rapid Prototyp. J. 22 (2016) 569–590. https://doi.org/10.1108/RPJ-01-2015-0011.
[25] M. Iqbal, Fazal-e-Aleem, Theory And Design Of Thermionic Electron Beam Guns, in: Cairo (Egypt), (2005): pp. 376–386. https://doi.org/10.1063/1.1896511.
[26] R.K. Edinger, Laser based electron beam gun, US6781300B1, (2004). https://patents.google.com/patent/US6781300B1/en?q=LASER+BASED+ELECTRON+BEAM+GUN+ralf&inventor=Ralf+Klaus+Edinger (accessed May 15, 2020).
[27] M. Galati, L. Iuliano, A literature review of powder-based electron beam melting focusing on numerical simulations, Addit. Manuf. 19 (2018) 1–20. https://doi.org/10.1016/j.addma.2017.11.001.
[28] T.R. Mahale, Electron beam melting of advanced materials and structures, Ph.D., North Carolina State University, (2009). https://search.proquest.com/docview/304967026/abstract/402C3E801D7D46C4PQ/1 (accessed May 19, 2020).
[29] Z.C. Cordero, H.M. Meyer III, P. Nandwana, R.R. Dehoff, Powder bed charging during electron-beam additive manufacturing, Acta Mater. 124 (2017) 437–445. https://doi.org/10.1016/j.actamat.2016.11.012.
[30] X. Gong, T. Anderson, K. Chou, Review on powder-based electron beam additive manufacturing technology, Manuf. Rev. 1 (2014) 2. https://doi.org/10.1051/mfreview/2014001.
[31] C. Li, Z.Y. Liu, X.Y. Fang, Y.B. Guo, Residual Stress in Metal Additive Manufacturing, Procedia CIRP. 71 (2018) 348–353. https://doi.org/10.1016/j.procir.2018.05.039.
[32] V.R. Utyaganova, A.V. Filippov, N.N. Shamarin, A.V. Vorontsov, N.L. Savchenko, S.V. Fortuna, D.A. Gurianov, A.V. Chumaevskii, V.E. Rubtsov, S.Yu. Tarasov, Controlling the porosity using exponential decay heat input regimes during electron beam wire-feed additive manufacturing of Al-Mg alloy, Int. J. Adv. Manuf. Technol. 108 (2020) 2823–2838. https://doi.org/10.1007/s00170-020-05539-9.
[33] V. Juechter, T. Scharowsky, R.F. Singer, C. Körner, Processing window and evaporation phenomena for Ti–6Al–4V produced by selective electron beam melting, Acta Mater. 76 (2014) 252–258. https://doi.org/10.1016/j.actamat.2014.05.037.
[34] S. Franchitti, R. Borrelli, C. Pirozzi, L. Carrino, W. Polini, L. Sorrentino, A. Gazzerro, Investigation on Electron Beam Melting: Dimensional accuracy and process repeatability, Vacuum. 157 (2018) 340–348. https://doi.org/10.1016/j.vacuum.2018.09.007.

[35] Y.E. Zafer, S. Goel, A. Ganvir, A. Jansson, S. Joshi, Encapsulation of Electron Beam Melting Produced Alloy 718 to Reduce Surface Connected Defects by Hot Isostatic Pressing, Materials. 13 (2020) 1226. https://doi.org/10.3390/ma13051226.
[36] S.M. Gaytan, L.E. Murr, F. Medina, E. Martinez, M.I. Lopez, R.B. Wicker, Advanced metal powder based manufacturing of complex components by electron beam melting, Mater. Technol. 24 (2009) 180–190. https://doi.org/10.1179/106678509X12475882446133.
[37] P. Prabhakar, W.J. Sames, R. Dehoff, S.S. Babu, Computational modeling of residual stress formation during the electron beam melting process for Inconel 718, Addit. Manuf. 7 (2015) 83–91. https://doi.org/10.1016/j.addma.2015.03.003.
[38] X. Zhang, F. Martina, A.K. Syed, Xueyuan Wang, Jialuo Ding, S.W. Williams, Fatigue Crack Growth in Additive Manufactured Titanium: Residual stress control and life evaluation method development, in: Nagoya, Japan, (2017). https://doi.org/10.13140/rg.2.2.29032.16643.
[39] B. Cheng, K. Chou, Thermal stresses associated with part overhang geometry in electron beam additive manufacturing: process parameter effects, in: Proc Annu Int Solid Free. Fabr Symp, Austin, TX, (2014): p. 1076.
[40] S. Liu, Y.C. Shin, Additive manufacturing of Ti6Al4V alloy: A review, Mater. Des. 164 (2019) 107552. https://doi.org/10.1016/j.matdes.2018.107552.
[41] S. Biamino, B. Kloden, T. Weibgarber, B. Kieback, U. Ackelid, Titanium aluminides for automotive applications processed by electron beam melting, in: Proc Word PM, Orlando, FL, (2014): pp. 96–103.
[42] D.H. Abdeen, B.R. Palmer, Effect of processing parameters of electron beam melting machine on properties of Ti-6Al-4V parts, Rapid Prototyp. J. 22 (2016) 609–620. https://doi.org/10.1108/RPJ-09-2014-0105.
[43] A. Safdar, H.Z. He, L. Wei, A. Snis, L.E. Chavez de Paz, Effect of process parameters settings and thickness on surface roughness of EBM produced Ti-6Al-4V, Rapid Prototyp. J. 18 (2012) 401–408. https://doi.org/10.1108/13552541211250391.
[44] I. Gibson, D.W. Rosen, B. Stucker, Additive manufacturing technologies, Springer, (2014).
[45] H. Gong, Generation and detection of defects in metallic parts fabricated by selective laser melting and electron beam melting and their effects on mechanical properties., University of Louisville, (2013). https://ir.library.louisville.edu/etd/515.
[46] J. Karlsson, A. Snis, H. Engqvist, J. Lausmaa, Characterization and comparison of materials produced by Electron Beam Melting (EBM) of two different Ti–6Al–4V powder fractions, J. Mater. Process. Technol. 213 (2013) 2109–2118. https://doi.org/10.1016/j.jmatprotec.2013.06.010.
[47] M.F. Zaeh, M. Kahnert, The effect of scanning strategies on electron beam sintering, Prod. Eng. 3 (2009) 217–224. https://doi.org/10.1007/s11740-009-0157-1.
[48] H. Gong, K. Rafi, T. Starr, B. Stucker, The Effects of Processing Parameters on Defect Regularity in Ti-6Al-4V Parts Fabricated By Selective Laser Melting and Electron Beam Melting, in: Austin, TX, (2013): p. 16.
[49] N. Sanaei, A. Fatemi, N. Phan, Defect characteristics and analysis of their variability in metal L-PBF additive manufacturing, Mater. Des. 182 (2019) 108091. https://doi.org/10.1016/j.matdes.2019.108091.
[50] P.M. Cordero, J. Mireles, S. Ridwan, R.B. Wicker, Evaluation of monitoring methods for electron beam melting powder bed fusion additive manufacturing technology, Prog. Addit. Manuf. 2 (2017) 1–10.

[51] V. Buga, R.J. Dsouza, In-process monitoring for Electron Beam Additive Manufacturing using an infrared camera system, (2018).
[52] N. Boone, C. Zhu, C. Smith, I. Todd, J.R. Willmott, Thermal near infrared monitoring system for electron beam melting with emissivity tracking, Addit. Manuf. 22 (2018) 601–605. https://doi.org/10.1016/j.addma.2018.06.004.
[53] B.A. Fisher, J. Mireles, S. Ridwan, R.B. Wicker, J. Beuth, Consequences of Part Temperature Variability in Electron Beam Melting of Ti-6Al-4V, JOM. 69 (2017) 2745–2750. https://doi.org/10.1007/s11837-017-2597-y.
[54] S. Price, B. Cheng, J. Lydon, K. Cooper, K. Chou, On process temperature in powder-bed electron beam additive manufacturing: process parameter effects, J. Manuf. Sci. Eng. 136 (2014). https://doi.org/10.1115/1.4028485.
[55] E. Rodriguez, J. Mireles, C.A. Terrazas, D. Espalin, M.A. Perez, R.B. Wicker, Approximation of absolute surface temperature measurements of powder bed fusion additive manufacturing technology using in situ infrared thermography, Addit. Manuf. 5 (2015) 31–39. https://doi.org/10.1016/j.addma.2014.12.001.
[56] S. Price, J. Lydon, K. Cooper, K. Chou, Experimental temperature analysis of powder-based electron beam additive manufacturing, in: 24th Annu. Int. Solid Free. Fabr. Symp., Austin, TX, (2013): pp. 162–173.
[57] Y.S. Lee, M.M. Kirka, R.B. Dinwiddie, N. Raghavan, J. Turner, R.R. Dehoff, S.S. Babu, Role of scan strategies on thermal gradient and solidification rate in electron beam powder bed fusion, Addit. Manuf. 22 (2018) 516–527. https://doi.org/10.1016/j.addma.2018.04.038.
[58] E. Landau, E. Tiferet, Y.I. Ganor, R.K. Ganeriwala, M.J. Matthews, D. Braun, M. Chonin, G. Ziskind, Thermal characterization of the build chamber in electron beam melting, Addit. Manuf. 36 (2020) 101535. https://doi.org/10.1016/j.addma.2020.101535.
[59] M. Gouge, P. Michaleris, E. Denlinger, J. Irwin, The Finite Element Method for the Thermo-Mechanical Modeling of Additive Manufacturing Processes, in: Thermo-Mech. Model. Addit. Manuf., Elsevier, 2018: pp. 19–38. https://doi.org/10.1016/B978-0-12-811820-7.00003-3.
[60] G. Croset, G. Martin, C. Josserond, P. Lhuissier, J.-J. Blandin, R. Dendievel, In-situ layerwise monitoring of electron beam powder bed fusion using near-infrared imaging, Addit. Manuf. 38 (2021) 101767. https://doi.org/10.1016/j.addma.2020.101767.
[61] F. Pixner, R. Buzolin, S. Schönfelder, D. Theuermann, F. Warchomicka, N. Enzinger, Contactless temperature measurement in wire-based electron beam additive manufacturing Ti-6Al-4V, Weld. World. 65 (2021) 1307–1322. https://doi.org/10.1007/s40194-021-01097-0.
[62] J. Raplee, A. Plotkowski, M.M. Kirka, R. Dinwiddie, A. Okello, R.R. Dehoff, S.S. Babu, Thermographic microstructure monitoring in electron beam additive manufacturing, Sci. Rep. 7 (2017) 43554. https://doi.org/10.1038/srep43554.
[63] S.W. Price, On temperature measurements and analysis in electron beam additive manufacturing using near infrared thermography, thesis, University of Alabama Libraries, (2014). http://ir.ua.edu/handle/123456789/3027 (accessed December 15, 2021).
[64] N. Boone, Near Infrared Thermal Imaging for Process Monitoring in Additive Manufacturing - White Rose eTheses Online, The University of Sheffield, (2020). https://etheses.whiterose.ac.uk/27219/ (accessed December 15, 2021).

[65] R.D. Murphy, E.C. Forrest, A Review of In-situ Temperature Measurements for Additive Manufacturing Technologies., Sandia National Lab.(SNL-NM), Albuquerque, NM (United States), (2016).
[66] B.A. Fisher, Part Temperature Effects in Powder Bed Fusion Additive Manufacturing of Ti-6Al-4V, thesis, Carnegie Mellon University, (2018). https://doi.org/10.1184/R1/6720995.v1.
[67] C. Ledford, Development of Processing Techniques for the Fabrication of Pure Copper Components Utilizing EB-PBF., North Carolina State University, (2021).
[68] G. Croset, Caractérisation in situ par imagerie proche infrarouge en fabrication additive fusion sur lit de poudre par faisceau d'électrons, phdthesis, Université Grenoble Alpes, (2021). https://tel.archives-ouvertes.fr/tel-03275786 (accessed December 15, 2021).
[69] N.A. Alderson, Thermal Modeling and Simulation of Electron Beam Melting for Rapid Prototyping on Ti6Al4V Alloys, N. C. State Univ. (2012).
[70] T.S. Srivatsan, T.S. Sudarshan, Additive manufacturing: innovations, advances, and applications, CRC Press, (2015).
[71] C. Ledford, C. Rock, P. Carriere, P. Frigola, D. Gamzina, T. Horn, Characteristics and Processing of Hydrogen-Treated Copper Powders for EB-PBF Additive Manufacturing, Appl. Sci. 9 (2019) 3993.
[72] ASM International, D.U. Furrer, S.L. Semiatin, ASM International, eds., Metals process simulation, ASM International, Materials Park, Ohio, (2010).
[73] K.C. Mills, Recommended values of thermophysical properties for selected commercial alloys, Woodhead Publishing, (2002).
[74] T. Meng, Factors influencing the fluid flow and heat transfer in electron beam melting of Ti-6Al-4V, Master's Thesis, University of British Columbia, (2009).
[75] F. Farhang Mehr, S. Cockcroft, D. Maijer, A fully-coupled thermal-stress model to predict the behavior of the casting-chill interface in an engine block sand casting process, Int. J. Heat Mass Transf. 152 (2020) 119490. https://doi.org/10.1016/j.ijheatmasstransfer.2020.119490.
[76] D. Riedlbauer, T. Scharowsky, R.F. Singer, P. Steinmann, C. Körner, J. Mergheim, Macroscopic simulation and experimental measurement of melt pool characteristics in selective electron beam melting of Ti-6Al-4V, Int. J. Adv. Manuf. Technol. 88 (2017) 1309–1317. https://doi.org/10.1007/s00170-016-8819-6.
[77] DI-4718B: User's Manual, DATAQ Instruments, Ohio, n.d. https://www.dataq.com/resources/pdfs/manuals/di-4718b-daq-manual.pdf (accessed March 28, 2022).
[78] DI-8B47 Linearized Thermocouple Input Modules, DATAQ Instruments, Ohio, n.d. https://www.dataq.com/resources/pdfs/datasheets/di8b47.pdf (accessed March 28, 2022).
[79] P. Hannifin, Parker o-ring handbook, Park. Hannifin Corp. Clevel. OH. (2007).

Appendix A: Preliminary Temperature Measurement System

The data acquisition/logging unit in the AITML system was developed in a step-by-step approach, starting with a Preliminary Temperature Measurement System (PTMS) and gradually considering design complexities and working condition requirements. Identifying system limitations associated with the electronics in PTMS was a crucial step since the outcome helped develop a fully isolated temperature measurement instrument suitable to implement within an EB-based machine.

A.1 Design and Development

The PTMS was designed based on the Arduino Uno development board. The Arduino Uno is a low-cost and power-efficient microcontroller board that can run a user-supplied program for a specific task. It is based on the ATmega328P microchip and offers a wide selection of expansion modules (also known as shields). The board has multiple digital and analogue input/output pins, and it can be programmed through an open-source user-interface software referred to as "Arduino Integrated Development Environment" (IDE). Figure A.1. schematically shows the Arduino Uno board pins layout.

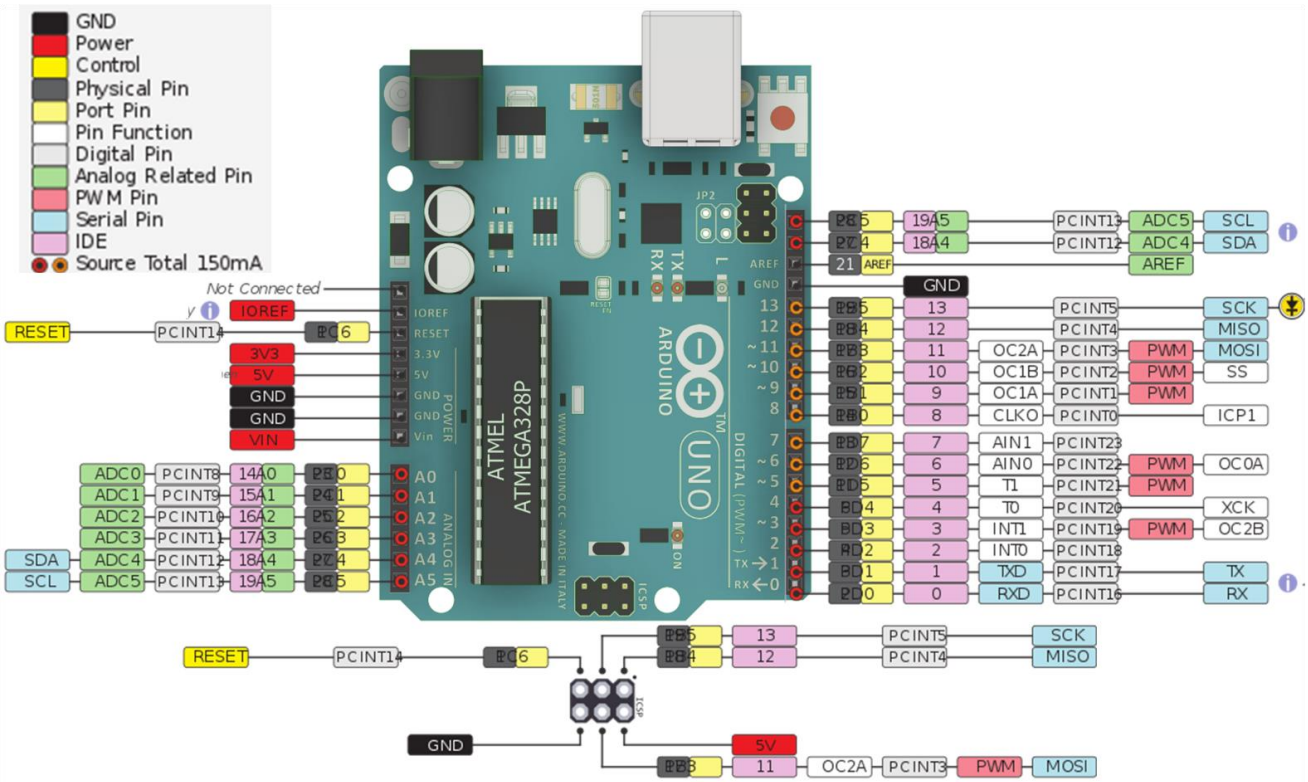

Figure A.1. Schematic illustration of the Arduino Uno board and pins layout.

Since thermocouples produce a low-level signal, an amplifier is needed to boost the signal level to a range that Arduino Uno can record. The first solution was to use MAX6675/MAX31855 amplifier, which connects to the Arduino Uno board and amplifies the analogue signal reading from the thermocouple, as shown in Figure A.2. The library to run this signal amplifier breakout board is presented in Appendix C.

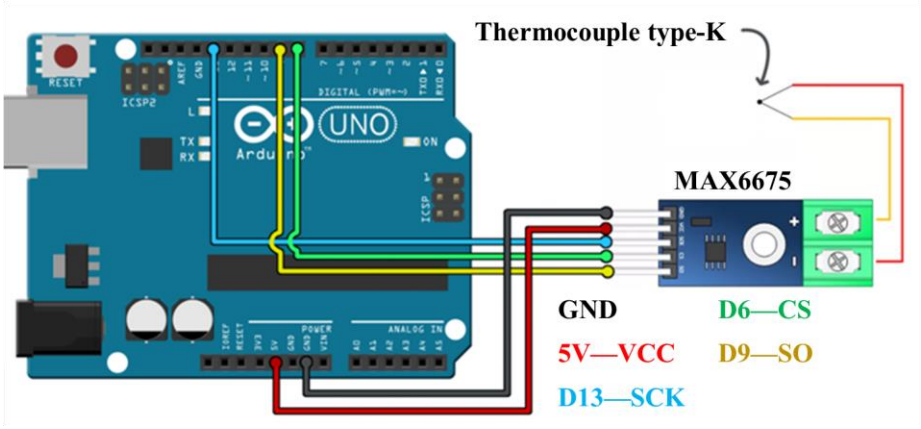

Figure A.2. Schematic of temperature measurement with MAX6675/31855 thermocouple signal amplifier.

This simple configuration allows recording the evolution of temperature from one thermocouple. Thus, it is an inefficient approach in the case of reading temperature from multiple thermocouples at the same time. A solution to this problem is to use a thermocouple expansion module, where the Arduino Uno board can read and record temperature from multiple thermocouples. For this purpose, the CN0391-ARDZ thermocouple module from ANALOG DEVICES was chosen, as shown in Figure A.3.

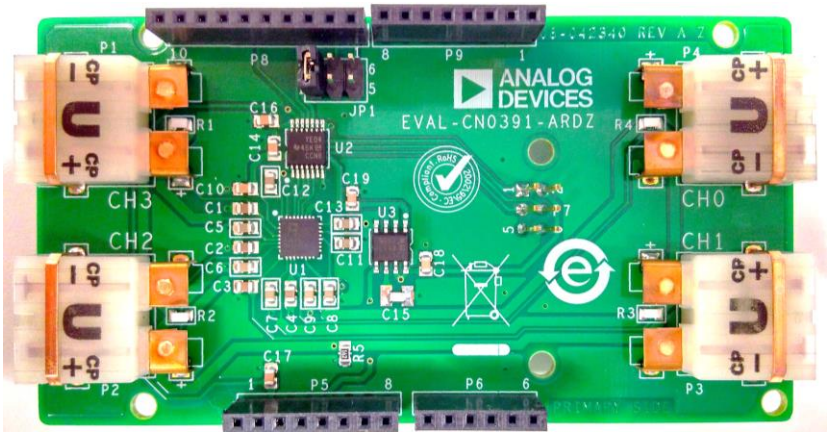

Figure A.3. EVAL-CN0391-ARDZ thermocouple shield from ANALOG DEVICES

This module is an integrated solution for multi-channel thermocouple temperature measurement with cold junction compensation. The CN0391 uses an 8-channel, low noise, low bower, 24-Bit, Sigma-Delta Analogue-to-Digital Converter (ADC). Each module can read the temperature from 4 thermocouples – any combination of type-B, E, J, K, N, R, S, T thermocouples.

As shown in Figure A.3., each channel uses a type-U Omega style connector for the thermocouple connection. There is a Resistance Temperature Detector (RTD) beneath the copper tabs for each connector (R1 to R4) to measure the temperature at the cold junction. This module utilizes voltage to temperature solution to calculate a linearized temperature. The temperature measurement formulation is discussed in greater detail in Appendix F. *Note that: three modules can be stacked on one Arduino Uno board to expand the number of channels from 4 to 12, as shown schematically in Figure A.4.*

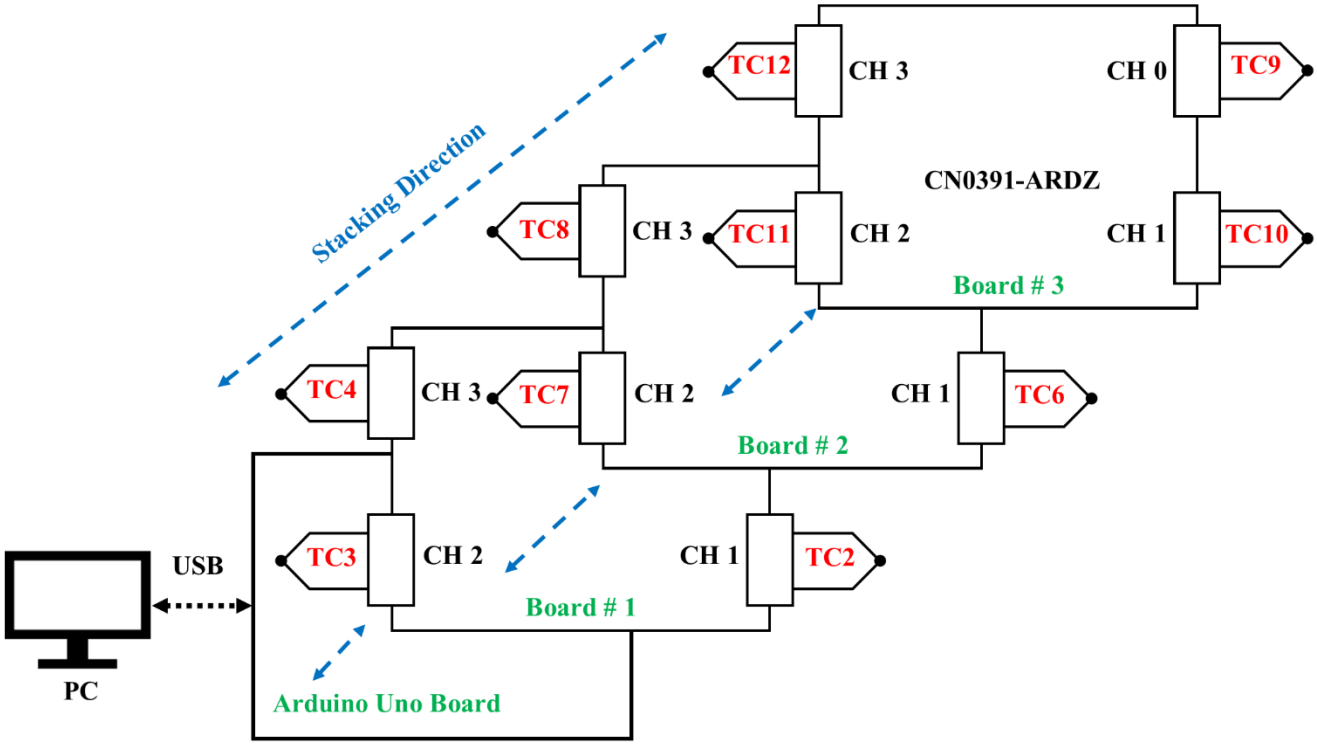

Figure A.4. A high-level schematic diagram of three CN0391-ARDZ modules stacked on one Arduino Uno board.

A.2 Hardware Configuration

The chip-select header, JP1 in Figure A.3, is used to select the chip-select pin when stacking multiple Arduino modules together. It should be noted that any change in the chip-select pin should be reflected in the code; otherwise, this would result in miscommunication between different modules connected to the Arduino Uno board. The thermocouples type should be defined in the main code, and the JP1 jumper pins should be placed across Pin 1 and 2 so that the module can communicate with the Arduino board. Then, the CN0391-ARDZ module is mounted on the Arduino Uno board, and the code is compiled through the Arduino IDE. Figure A.5. shows the configured Arduino-based PTMS.

(Top View)

(Side View)

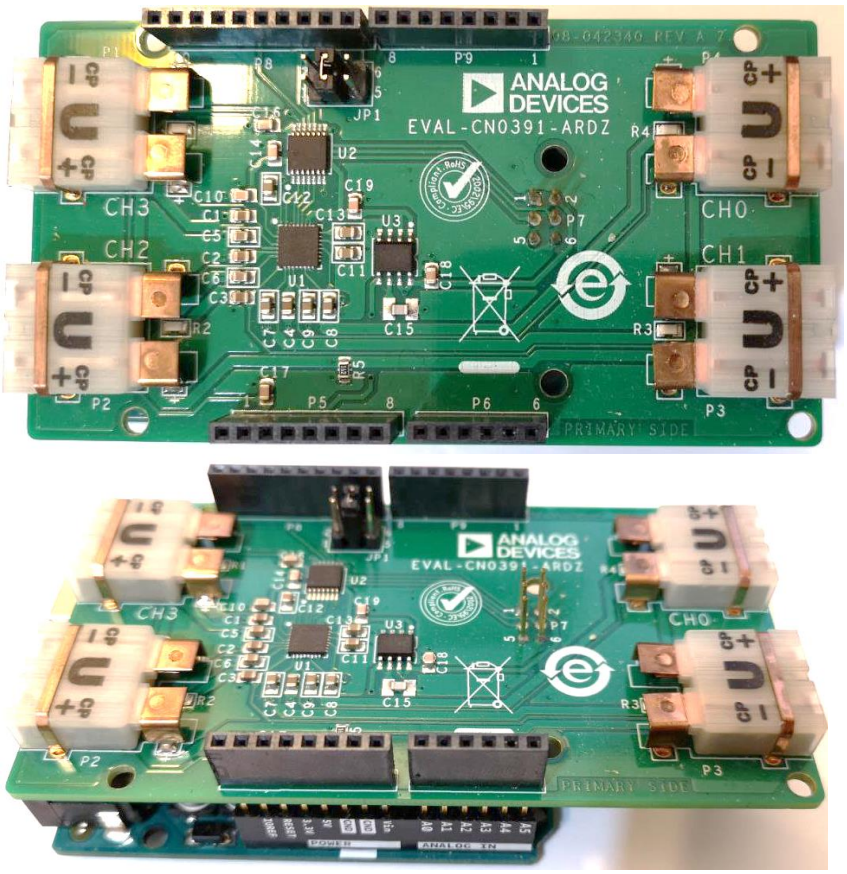

Figure A.5. Thermocouple module mounted on Arduino Uno board.

A Python script was prepared to monitor temperature evolution in real-time and log the temperature measurements in a CSV-format file. This Python script is provided in Appendix D: D. Furthermore, a data logger expansion module was used to remotely save the data on a micro SD[1] memory card, as shown in Figure A.6. The data logger has a real-time clock (RTC) on the board, which is used to timestamp activities with the current time and keeps time even when the module is unplugged. The SD card interface works with FAT16 or FAT32 formatted cards.

[1] Secure digital memory card

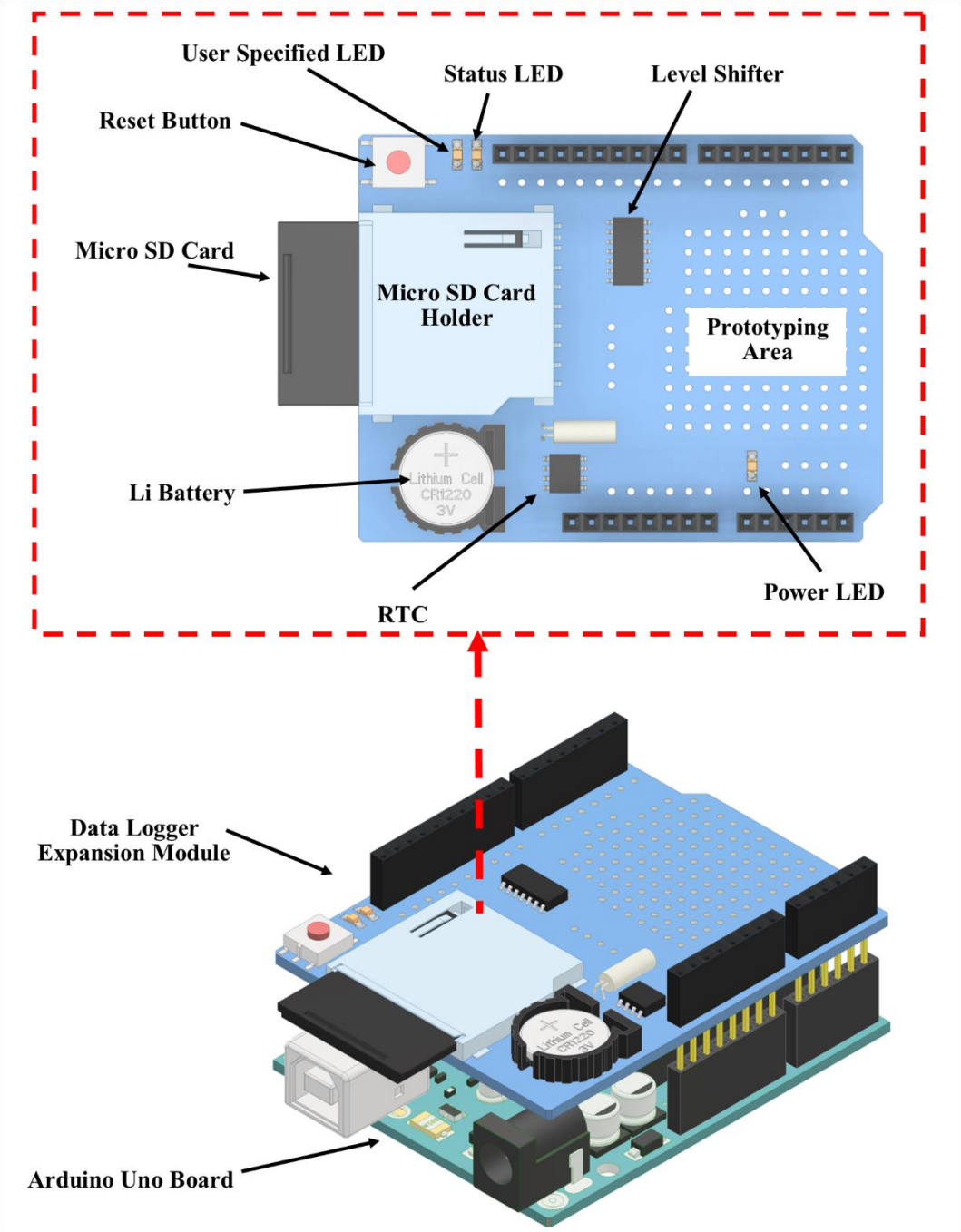

Figure A.6. A 3D CAD rendering of the Arduino data logger expansion module.

A.3 Challenges and System Limitations

The PTMS hardware configuration is relatively simple and can be easily modified. The system limitations of this design can be classified into four main categories: i) common chip-select pin between different expansion modules; ii) no built-in high-gain amplifier for boosting the

thermocouple signals for further analysis; iii) no electrical protection against electrical surges; and iv) no isolation barrier between different components – e.g., data logger, thermocouple module, Arduino Uno board, and batteries.

Sharing a common chip-select pin raises communication problems between the Arduino Uno board and other expansion modules. As a result, the microcontroller communicates randomly with each module. However, this issue can be solved by either rerouting the chip-select pin and adjusting the commands in the code for each module; or using two Arduino Uno with parallel I^2C communication (i.e., one Arduino Uno board per expansion module). *Note that: each solution has limitations, such as low data acquisition rate, low data logging rate, and higher power consumption*.

Considering the high-voltage electron beam of an EB-based machine, lack of electrical protection and isolation barrier between the electronic elements and acquiring noisy thermocouple signals are the key system limitations with the PTMS design. Therefore, another instrument was designed as a solution to these challenges with in-situ instrumentation.

Appendix B: Design of a Hermetic Enclosure

A metallic hermetic enclosure was designed to protect the electronic elements of the AITML system from the vacuum environment present within an EB-based machine. The enclosure was designed and developed step-by-step, starting with a Tee-junction chamber, and gradually considering design limitations. This approach helped design a low profile square-shaped hermetic enclosure that can withstand the high-vacuum environment of an EB-based machine. The following sections present the design procedure in greater detail.

B.1 Tee-Junction Hermetic Enclosure

The primary design was based on a Tee-junction vacuum chamber with a ConFlat flange design. Figure B.1 shows the exploded view of the assembled AITML system based on the Tee-junction enclosure. According to this figure, two ports were used to mount the thermocouples and D-subminiature feedthroughs. The thermocouple feedthrough connects four type-K thermocouples from the vacuum side to the signal conditioning modules inside the chamber. Once the measurement is finished, the AITML system can be connected to a computer via the multi-pin D-subminiature feedthrough to retrieve the recorded temperature data. *Note: the D-subminiature feedthrough is also used to configure the AITML system and retrieve data, as mentioned in Chapter 5.*

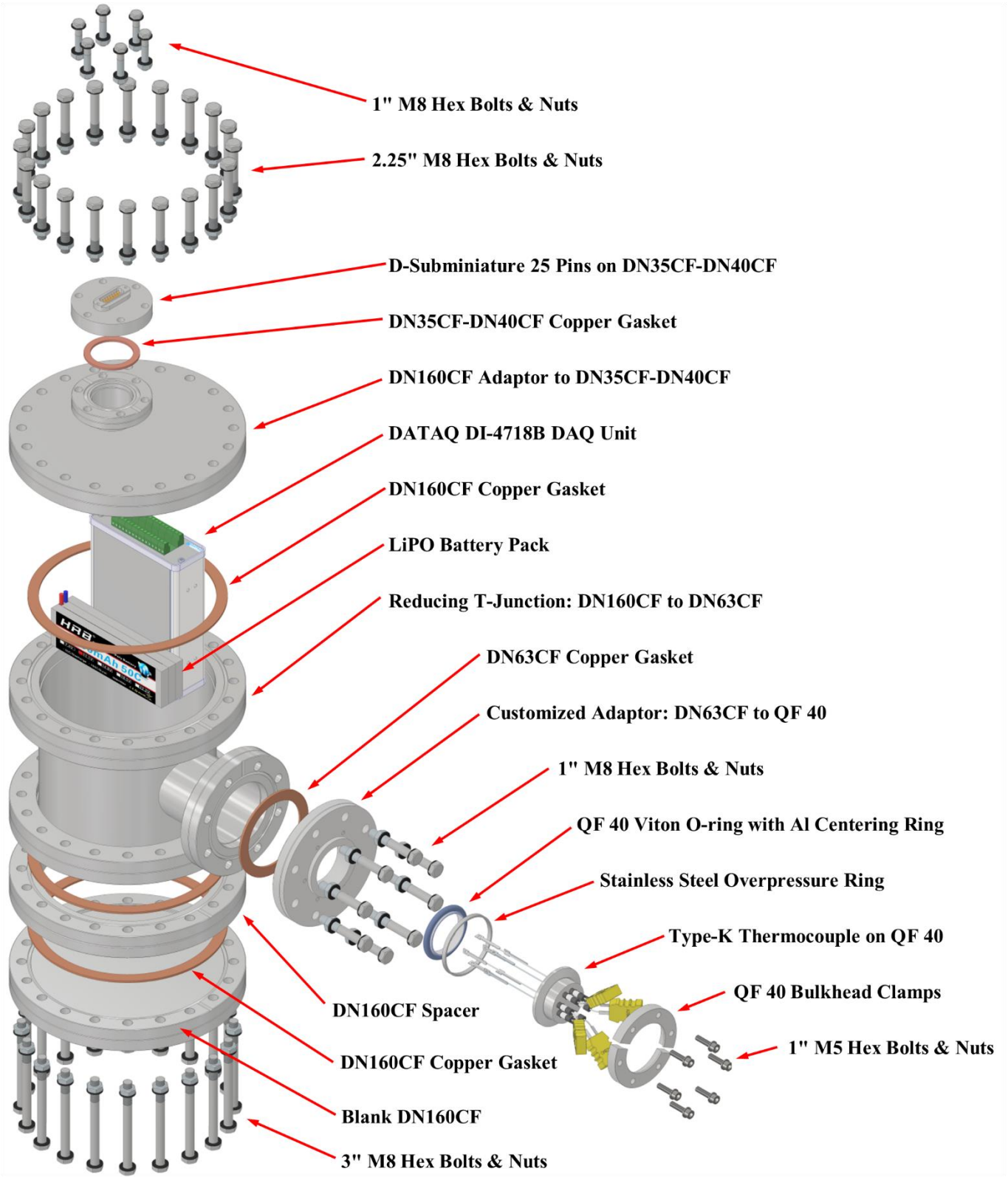

Figure B.1. A 3D CAD rendering of the assembled AITML system based on the primary hermetic enclosure prototype.

The sealing mechanism in the Tee-junction prototype is based on a knife-edge indentation into a metal gasket, as shown in Figure B.2. A knife-edge feature below the flange face bites into a metal gasket as the flange pairs are tightened together. The extruded metal fills all the surface defects and machining marks on both flange faces, providing the sealing mechanism. This sealing mechanism operates at the nominal temperature range from -196 °C to 450 °C within the pressure range of 1.01×10^{3} mbar to 1.30×10^{-13} mbar.

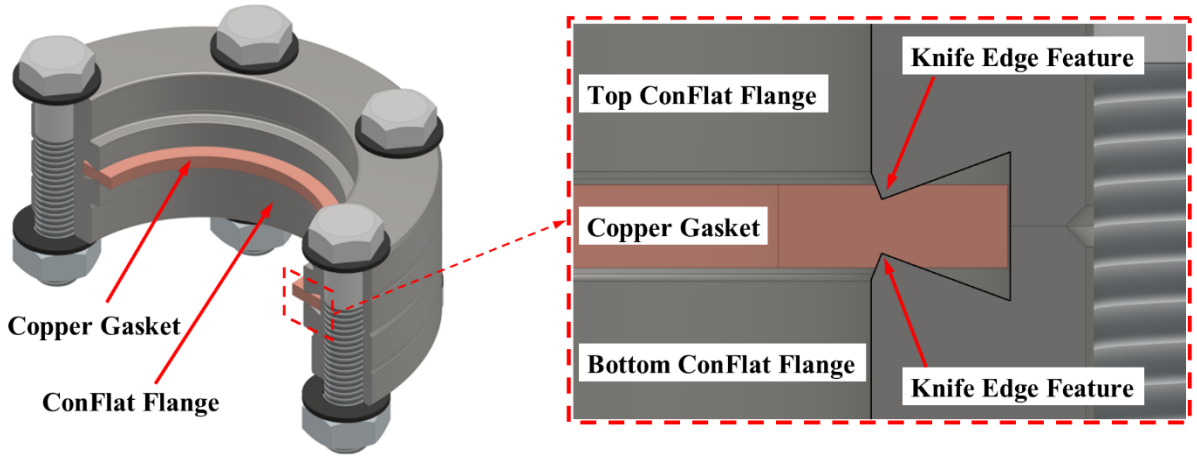

Figure B.2. 3D CAD rendering showing the Sealing mechanism for the ConFlat flange.

Despite the advantages of the Tee-junction design, there are three main challenges that could hinder further development of the AITML system, and are as follows: i) heavy-weight chamber in a complete assembly, ii) delicate knife-edge feature which could be damaged during maintenance, iii) single-time use Copper gaskets, which could result in high maintenance cost, and iv) inefficient use of space available inside the EB-based machine's vacuum chamber. These design limitations helped change the design to a compact square-shaped enclosure, as discussed in the following section.

B.2 Square-Shaped Hermetic Enclosure

The square-shaped hermetic enclosure design was the solution to the challenges with the initial prototype – i.e., the Tee-junction enclosure. Figure B.3 shows the 3D CAD rendering of this design. The thermocouple and D-subminiature feedthroughs were placed on the side and top of the enclosure to maintain a low profile and a compact design, which optimizes the space needed for the unit.

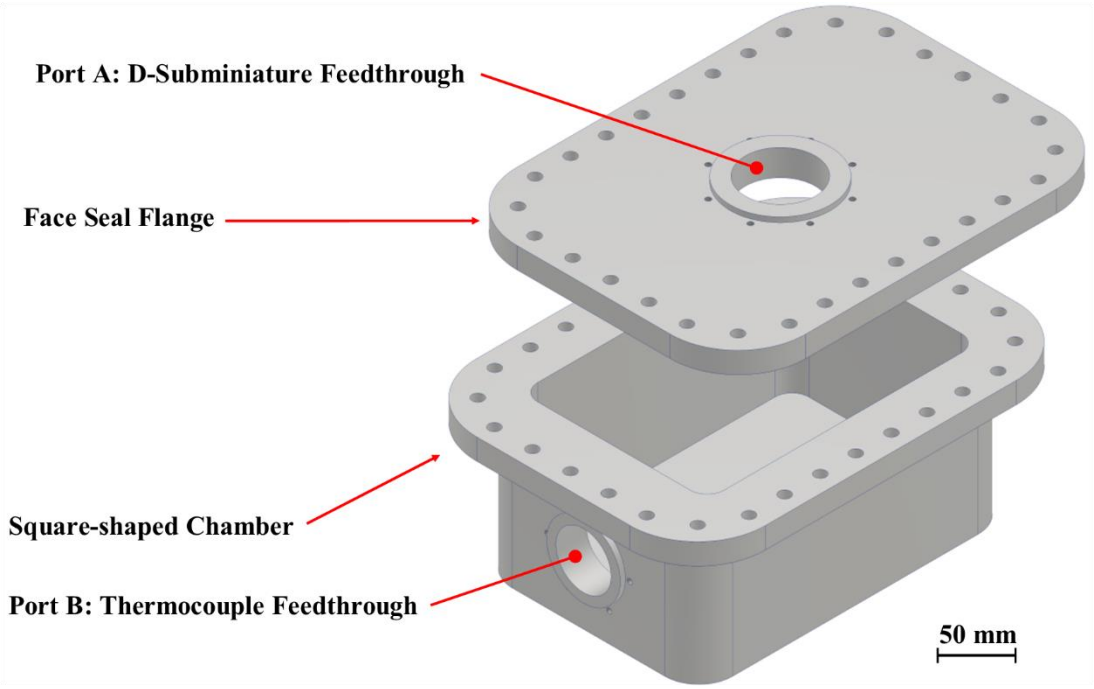

Figure B.3. Square-shaped chamber designed for AITML system to enclose the electronics and power source.

Contrary to the T-junction prototype, the sealing mechanism in this design is based on compressing a polymer O-ring, normally Fluorocarbon (FKM), between the sealing faces – e.g., the chamber/flange or the feedthrough/port interfaces. This sealing mechanism reduces the maintenance cost and the chance of damaging the sealing faces during maintenance. Under compression, the O-ring is elastically deformed, causing contact pressure on both sealing faces. *Note: the face seal mechanism functions properly if the contact pressure between the O-ring and the sealing interfaces is greater than the existing positive/negative pressure within the system.*

The contact pressure depends on the O-ring's cross-sectional diameter and the O-ring groove's design. Additionally, in the case of a non-circular O-ring groove, the inside corner radius in the O-ring's groove should be carefully designed to avoid extensive stress concentration at the turning corners. Overstressing the O-ring around the bend area may lead to a leak at the corners. Figure B.4 shows the design criteria for the non-circular face seal mechanism, used for the hermetic enclosure, according to the guideline published by Parker corporation [79]. *Not: the operating temperature of the face seal mechanism is limited to the working temperature range of the O-ring – e.g., the working temperature of the FKM O-rings is from -26 °C to +204 °C, depending on the O-ring grade* [79].

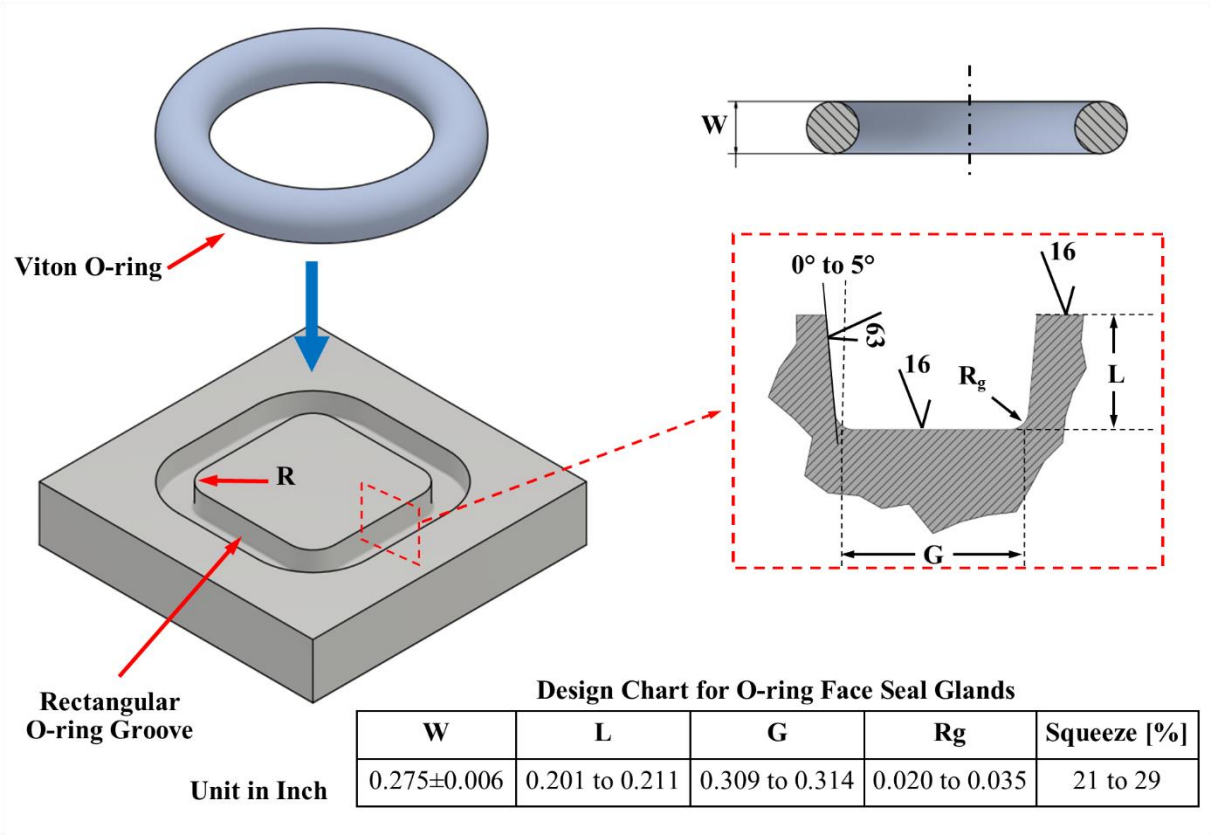

Design Chart for O-ring Face Seal Glands

W	L	G	Rg	Squeeze [%]
0.275±0.006	0.201 to 0.211	0.309 to 0.314	0.020 to 0.035	21 to 29

Unit in Inch

Figure B.4. Non-circular O-ring design in the flat face sealing configuration – ideal design: R ≥ 6 × W but not less than R ≥ 3 × W.

A prototype was printed from PLA material by a Raise3D Pro Plus FDM 3D printer, as shown in Figure B.5. The PLA prototype was used to fit test all electrical and mechanical components and identify potential design flaws. After the evaluation, a few minor adjustments (in terms of filet radii and internal dimensions) were identified, and the design was updated accordingly. Furthermore, two overpressure rings were added to the assembly to minimize the chance of leakage at ports A and B – as shown in Figure B.3. The overpressure ring limits the expansion of the O-ring if the internal pressure is greater than the external or contact pressure, leading to attain the sealability at these ports.

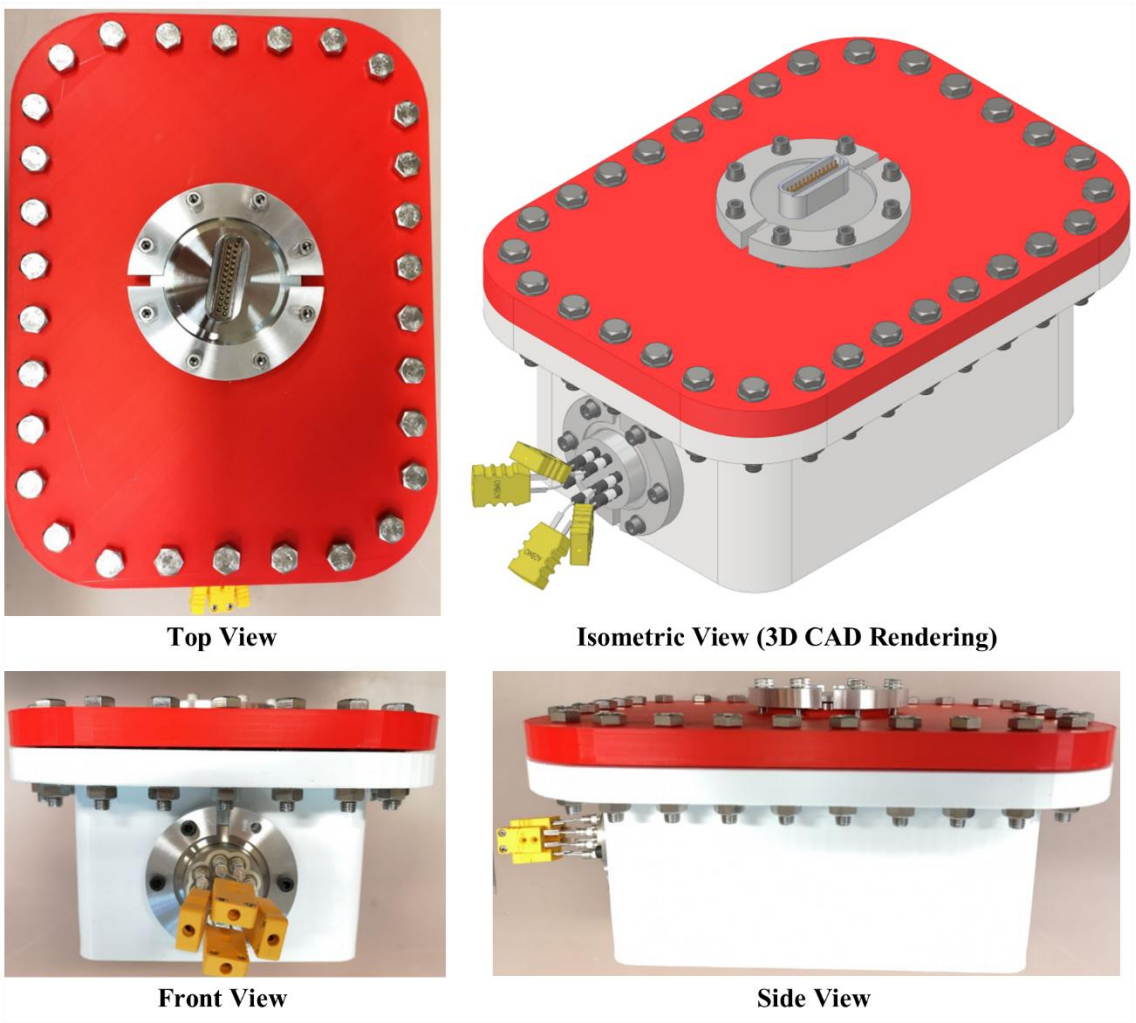

Figure B.5. The PLA prototype of the square-shaped hermetic enclosure.

As shown in Figure B.6, a 0.5 inches thick alumina fibre blanket[1] can be fitted inside the enclosure to protect the electronic elements if the system is placed inside a high-temperature environment.

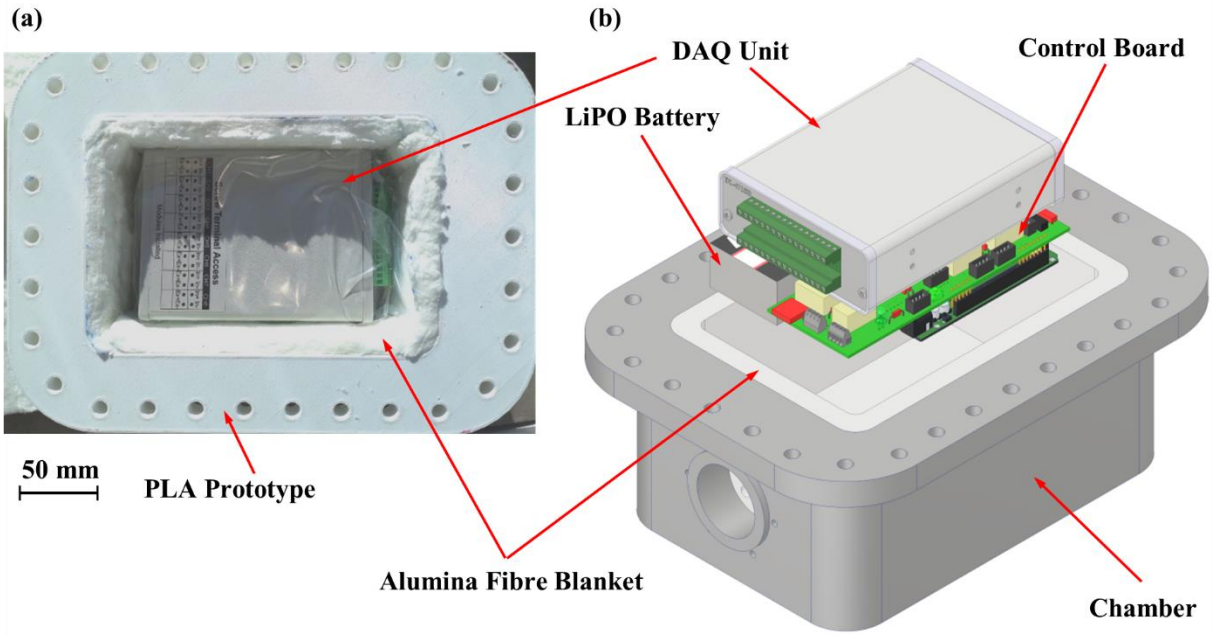

Figure B.6. Insulating the enclosure's interior space with Alumina fibre blanket, (a) top view of PLA prototype, and (b) the isometric view of the 3D CAD rendering.

The hermetic enclosure was made out of a 6061-T6 Aluminum alloy. The flange and chamber were machined out using the LiTZ Hitech LV-800 CNC machine, as shown in Figure B.7. Once the machining process was finished, the sealing faces were polished with sanding paper starting from grit 400 up to 1200 to remove the rough machining marks at the sealing interfaces.

[1] Chemical composition: Al2O3 (45%), SiO2 (53.5%), Fe2O3 (<1.2%), Na2O+K2O (<0.5%)

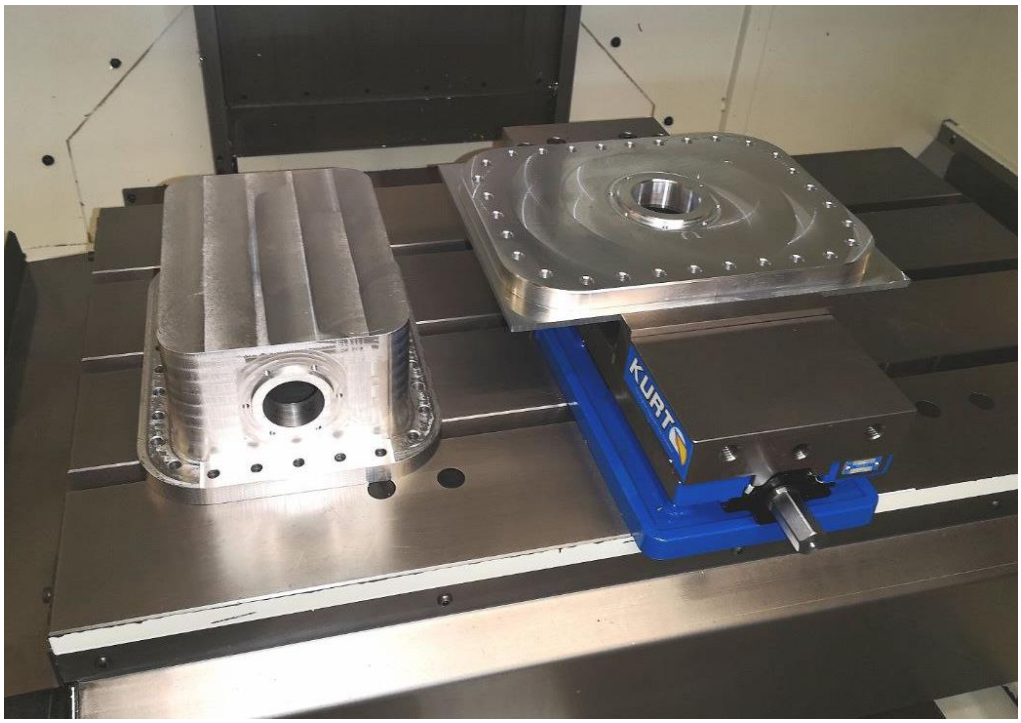

Figure B.7. CNC machining of the flange and chamber out of a bulk Aluminum 6061-T6.

Appendix C: The library to set-up MAX6675 on Arduino Uno

```
//MAX6675 Library:
#include <avr/pgmspace.h>
#include <util/delay.h>
#include <stdlib.h>
#include "max6675.h"
MAX6675::MAX6675(int8_t SCLK, int8_t CS, int8_t MISO)
{
	sclk = SCLK;
	cs = CS;
	miso = MISO;
//define pin modes
	pinMode(cs, OUTPUT);
	pinMode(sclk, OUTPUT);
	pinMode(miso, INPUT);
	digitalWrite(cs, HIGH);
}
double MAX6675::readCelsius(void)
{
	uint16_t v;
	digitalWrite(cs, LOW);
	_delay_ms(1);
	v = spiread();
	v <<= 8;
	v |= spiread();
	digitalWrite(cs, HIGH);
	if (v & 0x4) {
		//thermocouple attached!
		return NAN;
		//return -100;
	}
	v >>= 3;
	return v*0.25;
}
double MAX6675::readFahrenheit(void)
{
	return readCelsius() * 9.0/5.0 + 32;
}
byte MAX6675::spiread(void)
{
	int i;
	byte d = 0;
	for (i=7; i>=0; i--)
	{
		digitalWrite(sclk, LOW);
		_delay_ms(1);
```

```
                if (digitalRead(miso)) {
                        //set the bit to 0 no matter what
                        d |= (1 << i);
                }
                digitalWrite(sclk, HIGH);
                _delay_ms(1);
        }
        return d;
}
//Arduino Uno code to work with MAX6675
#include "max6675.h"       //INCLUDE THE LIBRARY
int thermoDO = 9;
int thermoCS = 8;
int thermoCLK = 13;
MAX6675 thermocouple(thermoCLK, thermoCS, thermoDO);
void setup()
{
        Serial.begin(9600);
        Serial.println("MAX6675 test");
        // wait for MAX chip to stabilize
        delay(500);
}
void loop()
{
        // basic readout test, just print the current temp
        Serial.print("C = ");
        Serial.println(thermocouple.readCelsius());
        Serial.print("F = ");
        Serial.println(thermocouple.readFahrenheit());
        delay(1000);
}
```

Appendix D: Python Script – Temperature Logging and Real-Time Plotter

```
import serial
import time, datetime
import matplotlib.pyplot as plt
import csv
import os
import sys
import string
#_____________________Define Variables_____________________________#
xs = [] #store trials here (n)
ys1 = [] #store relative frequency here
ys2 = [] #store relative frequency here
ys3 = [] #store relative frequency here
ys4 = [] #store relative frequency here
relativeTime = [] # store relative time from start
tempresult = [0]*30
#_____________________Time Stamp_____________________________#
def Timestamp():
        date_now = time.strftime('%d/%m/%y')
        time_now = time.strftime('%H:%M:%S')
        return [date_now,time_now]
#First we create a name for the CSV file that is going to be date and time
name=time.strftime("%Y_%m_%d_%H_%M_%S", time.gmtime())
# Ask how long want to log data:
v1 = input("How long would you like to log [in minutes]: ")
v2 = float (v1) * 60
# Define Serial communication:
sert = serial.Serial ('COM4', 9600)
time.sleep(0.1)
countert = 0    #First Counter
#Read and record the data
for i in range (2):
        sert.flush()
        countert += 1
        bt = sert.readline()
        string_nt = bt.decode()
        cct = string_nt.rstrip()
        at = cct.rsplit(" ")
        row1t = at
        if countert == 1:
                row1t = at
                timeRefresh = (float (row1t[1]))/1000
#print (timeRefresh)    #Printdelay time
sert.close()
va3 = float (v2)/float (timeRefresh)
va3 = int (va3)
```

```
time.sleep(1)
print ("With ",v1," minutes, there will be ",va3," data points!")
# Opening Serial for data logging:
ser = serial.Serial ('COM4', 9600)
time.sleep(0.5)
#_____Define Variable for reading from Serial_____#
counter = 0
data =[]
# Open csv file:
f = open(name+'.csv','w+');
result = csv.writer(f, delimiter= ',', lineterminator='\n')
result_statement = ("Relative time","Channel","init Temp","CJ [mv]","TC reading [mv]","TC [mv]","Temperature","Unit");
result.writerow(result_statement)
f.close()
#_____Opening Serial and Reading data_____#
#while True:
        for i in range(va3):
        counter += 1
        ser.flush()
        b = ser.readline()
        string_n = b.decode()
        cc = string_n.rstrip()
        print (counter)
        a = cc.rsplit(" ") #fixed the problem with \r\n at the end of the string
        row1 = a
                if counter == 1:
                row1 = a
        relativeTime = (timeRefresh * i)
        tempresult[0] = float (relativeTime)
# Channel 1
        tempresult[1] = str (row1[3])
        tempresult[2] = float (row1[4])
        tempresult[3] = float (row1[5])
        tempresult[4] = float (row1[6])
        tempresult[5] = float (row1[7])
        tempresult[6] = float (row1[8])
        tempresult[7] = str (row1[9])
# Channel 2
        tempresult[8] = str (row1[13])
        tempresult[9] = float (row1[14])
        tempresult[10] = float (row1[15])
        tempresult[11] = float (row1[16])
        tempresult[12] = float (row1[17])
        tempresult[13] = float (row1[18])
        tempresult[14] = str (row1[19])
```

```
# Channel 3
            tempresult[15] = str (row1[23])
            tempresult[16] = float (row1[24])
            tempresult[17] = float (row1[25])
            tempresult[18] = float (row1[26])
            tempresult[19] = float (row1[27])
            tempresult[20] = float (row1[28])
            tempresult[21] = str (row1[29])
# Channel 4
            tempresult[22] = str (row1[34])
            tempresult[23] = float (row1[35])
            tempresult[24] = float (row1[36])
            tempresult[25] = float (row1[37])
            tempresult[26] = float (row1[38])
            tempresult[27] = float (row1[39])
            tempresult[28] = str (row1[40])
#print (relativeTime) # to check the output
            print (row1)
            print (tempresult)
            f = open(name+'.csv','a');
            result = csv.writer(f, delimiter= ',', lineterminator='\n')
            result.writerow(tempresult)
            xss = float (relativeTime)
            yss1 = float (row1[8])
            yss2 = float (row1[18])
            yss3 = float (row1[28])
            yss4 = float (row1[39])
            xs.append(xss)
            ys1.append(yss1)
            ys2.append(yss2)
            ys3.append(yss3)
            ys4.append(yss4)
            data.append(row1)
            f.close()
ser.close()
#_____________________Plot data_____________________#
print (xs)
print (ys1, ys2, ys3, ys4)
plt.plot(xs, ys1)
plt.plot(xs, ys2)
plt.plot(xs, ys3)
plt.plot(xs, ys4)
plt.xlabel('Time [s]')
plt.ylabel('Temperature [C]')
plt.show()
#_____________________ END of Script_____________________#
```

Appendix E: Python Script – Pressure Logging and Real Time Plotter

```
#_____________________Headers Definition_____________________________#

import serial
import matplotlib.pyplot as plt
import numpy as np
import time, datetime
import csv
import os
import sys
import string
plt.ion()
fig=plt.figure()
#_____________________Define Variables_____________________________#
t =[]
p =[]
T = []
counter = 0
#_____________________Time Stamp_____________________________#
tempdata = [0]*3
def Timestamp():
        date_now = time.strftime('%d/%m/%y')
        time_now = time.strftime('%H:%M:%S')
        return [date_now,time_now]
#First we create a name for the CSV file that is going to be date and time
name=time.strftime("%Y_%m_%d_%H_%M_%S", time.gmtime())
f = open(name+'.csv','w+');
result = csv.writer(f, delimiter= ',', lineterminator='\n')
result_statement = ("Relative time","Pressure","Temperature");
result.writerow(result_statement)
f.close()
#_____________Opening Serial to read data from Arduino_____________#
# Opening Serial to read data from Arduino
ser = serial.Serial('COM5',9600)
ser.close()
ser.open()
while True:
        counter += 1
        ser.flush()
        b = ser.readline()
        string_n = b.decode()
        cc = string_n.rstrip()
        print (counter)
        a = cc.rsplit(" ") #fixed the problem with \r\n at the end of the string
        row1 = a
        if counter == 1:
```

```
                row1 = a
            t = float (row1[0])
            p = float (row1[1])
            T = float (row1[2])
            tempdata[0] = float (row1[0])
            tempdata[1] = float (row1[1])
            tempdata[2] = float (row1[2])
#print (relativeTime) # to check the output
            print (row1)
#data = ser.readline()
#print(data.decode())
#_____________________Plot data_____________________#
# Plot Pressure and Temp
plt.figure(1)
plt.scatter(t, p)
plt.xlabel('Time [s]')
plt.ylabel('Pressure [kPa]')
plt.grid(True)
plt.show()
plt.pause(0.0001)
plt.figure(2)
plt.scatter(t, T)
plt.xlabel('Time [s]')
plt.ylabel('Temperature [C]')
plt.grid(True)
plt.show()
plt.pause(0.0001) # Note this correction
# Open csv file:
f = open(name+'.csv','a');
result = csv.writer(f, delimiter= ',', lineterminator='\n')
result.writerow(tempdata)
f.close()
#_____________________ END of Script_____________________#
```

Appendix F: Temperature Measurement Formulation used CN0391-ARDZ Module

The CN0391-ARDZ thermocouple module calculates a linearised temperature using voltage to temperature solution according to the National Institute of Standards and Technology (NIST). The linearisation algorithm is based on the cold junction temperature compensation and the voltage signal generated by the thermocouple. The calculation and linearization process includes the following steps: i) cold junction temperature measurement and ii) thermocouple measurement.

For the cold junction temperature measurement, the reading from each RTD channel is used to calculate RTD resistance. The RTD is ideally 1000 Ω at 0 °C. Depending on the calculated resistance, the linearisation algorithm can be calculated using the Eqs. (F.1) to (F.3):

$$R_{RTD} = R_5 \times \frac{(O_{ADC} - 2^{N-1})}{(G \times 2^{N-1})} \quad \text{(F.1)}$$

$$\{R_5 = 1.6\ k\Omega\ ;\ G = 1\ ;\ N = 24\}$$

i) RTD resistance > 1000 Ω:

$$R_{RTD} = R_0[1 + AT + BT^2] \quad \text{(F.2)}$$

$$\{A = 3.9083 \times 10^{-3}\ ;\ B = -5.775 \times 10^{-7}\}$$

ii) RTD resistance ≤ 1000 Ω:

$$R_{RTD} = R_0[1 + AT + BT^2 + CT^3(T - 100)] \quad \text{(F.3)}$$

$$\{A = 3.9083 \times 10^{-3}\ °C^{-1}; B = -5.775 \times 10^{-7}\ °C^{-2}; C = -4.183 \times 10^{-12}\ °C^{-4}\}$$

where O_{ADC} is the ADC output, R_5 (Ω) is the reference resistor, G is the gain value; T_{RTD} is the cold junction temperature, R_{RTD} (Ω) is the RTD resistance at any temperature, R_{RTD0} (Ω) is the

RTD resistance at 0 °C (in this case 1000 Ω), r (Ω) is the RTD resistance when the temperature is less than 0 °C, and A, B, C are constant parameters.

The standard NIST equations are used for thermocouple temperature linearisation. First, the cold junction temperature is converted to a cold junction voltage using Eq. (F.4):

$$V_{CJ} = a_0 + a_1 T + a_2 T^2 + \cdots + a_n T^n \quad \text{(F.4)}$$

where V_{CJ} (μV) is the thermoelectric cold junction voltage, a_n is the thermocouple type-dependent polynomial coefficient, T °C is the cold junction temperature, and n is the order of the polynomial function.

The final thermocouple voltage at each channel is calculated using Eq. (F.5), where V_{TC} (μV), $V_{TC.read}(\mu V)$, and $V_{CJ}(\mu V)$ are the final voltage value for the thermocouple channel, voltage value measured at the thermocouple channel and calculated cold junction voltage, respectively.

$$V_{TC} = V_{TC.read} + V_{CJ} \quad \text{(F.5)}$$

The final step in the linearisation is to use the value calculated from Eq. (F.5) and calculate the temperature T (°C), as described in Eq. (F.6):

$$T = a_0 + a_1 V_{TC} + a_2 {V_{TC}}^2 + a_3 {V_{TC}}^3 + \cdots + a_n {V_{TC}}^n \quad \text{(F.6)}$$

Appendix G: Sensitivity Analysis

A sensitivity analysis was conducted to further evaluate the effect of changing a number of model parameters on the evolution of temperature within the pseudo build environment. This helps to identify and delineate the key model parameters – i.e., the parameters that have the largest effect on the model predictions. The base model values were found to give the best fit to the experimental measurements, as discussed in Chapter 5.

G.1 Mesh sensitivity

Choosing the mesh size often represents a trade-off between the computational time and the accuracy of the model predictions. Using fine meshes results in higher accuracy but for a longer simulation time. The sensitivity cases were run with a series of mesh sizes as presented in Table G.1. The sensitivity analysis results to the mesh size are presented as temperature contours of the CP-Ti disk and the heat shield captured at the last step of the heating cycle, as shown in Figure G.1.

Table G.1. Mesh statistics for the sensitivity analysis

Mesh Parameter	Part	Coarse	Base Model	Fine
Maximum Edge Length [mm]	CP- Ti Disk	1.25	1.00	0.75
	SS-Plate	12.50	10.00	7.50
	Heat Shield	12.50	10.00	7.50
Number of Nodes	CP- Ti Disk	11,216	22,060	50,700
	SS-Plate	4,020	7,278	16,464
	Heat Shield	5,740	8,800	15,080
Number of Elements	CP- Ti Disk	9,422	19,215	45,660
	SS-Plate	2,964	5,680	13,685
	Heat Shield	3,978	6,192	10,773

According to Figure G.1 (a), the temperature contours on a vertical section through the CP-Ti disk at the end of the heating cycle appear to be very similar. However, upon close

examination, there is a slight variation in the position of the isotherms. In Addition, the temperature contour plots of the heat shield show a similar trend, as illustrated in Figure G.1 (b). Since the mesh size did not significantly influence the temperature distribution within the pseudo build environment, the base model was found to be a reasonable compromise between the simulation time and the accuracy – considering the moderate resolution for the predicted isotherms.

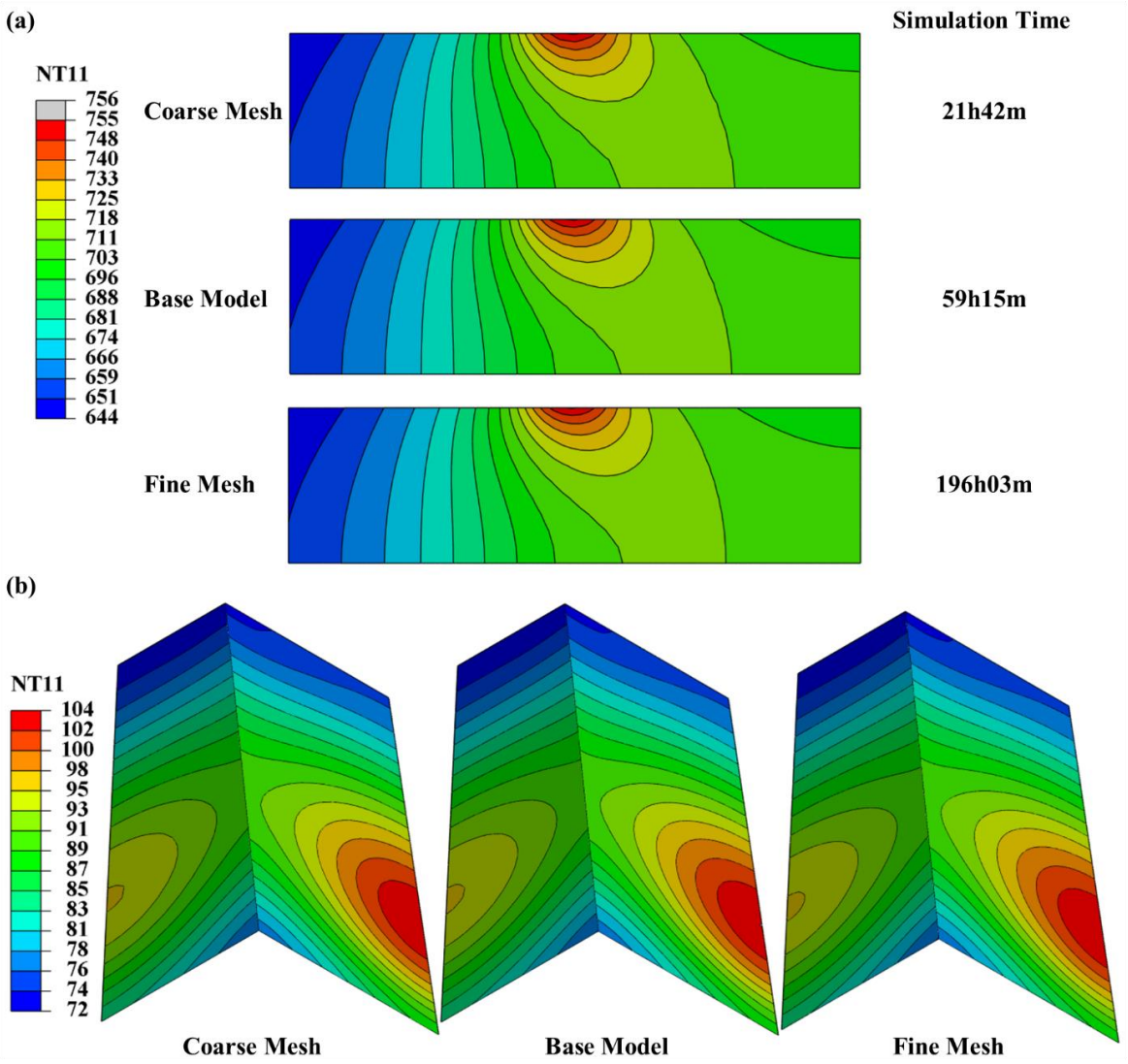

Figure G.1. Mesh sensitivity analysis results showing the temperature contours on (a) a vertical section through the CP-Ti disk, and (b) the heat shield captured at the end of the heating cycle.

G.2 Model Parameters

This section evaluates the effect of changing a few model input parameters on the thermal field within the pseudo build environment. To conduct the sensitivity analysis, only one parameter was changed at a time, and the change varied from 75 % to 125 % of the base model values. The parameters and range of values used in the sensitivity analysis cases are presented in Table G.2 and Figure G.2.

The results of the analysis are presented as precent of relative change in the temperature with respect to the base model predictions, as mathematically represented in Eq. (G.1), at the last step of the heating and cooling cycles.

$$R_T = \frac{T_c - T_{BM}}{T_{BM}} \times 100 \qquad \text{(G.1)}$$

where R_T (%) is the percent of relative change in the temperature, and T_c (°C) and T_{BM} (°C) are the temperature data for each sensitivity case study and the base model, respectively. The R_T was evaluated along with lines, A-A', B-B', and C-C' – refer to Figure 4.12 in Chapter 4 for the location of these lines.

Table G.2. Model input parameters used for the sensitivity analysis

Model Input Parameter	Unit	Base Model	Variations	Code
EB Absorption Factor (η)	-	0.6500	0.8125	125 η
			0.4875	75 η
Standard Deviation of the Gaussian Function (σ_{EB})	mm	2.500	3.125	125 σ_{EB}
			1.875	75 σ_{EB}
Open Cavity Ambient Temperature (T_{cav})	°C	30.0	37.5	125 T_{cav}
			22.5	75 T_{cav}
Ambient Temperature inside the EBBF Vacuum Chamber (T_{amb})	°C	Refer to Figure G.1 (a)		125 T_{amb}
				75 T_{amb}
Interfacial Heat Transfer Coefficient ($IHTC$)	W m^{-2} K^{-1}	Refer to Figure G.2 (b).		125 $IHTC$
				75 $IHTC$

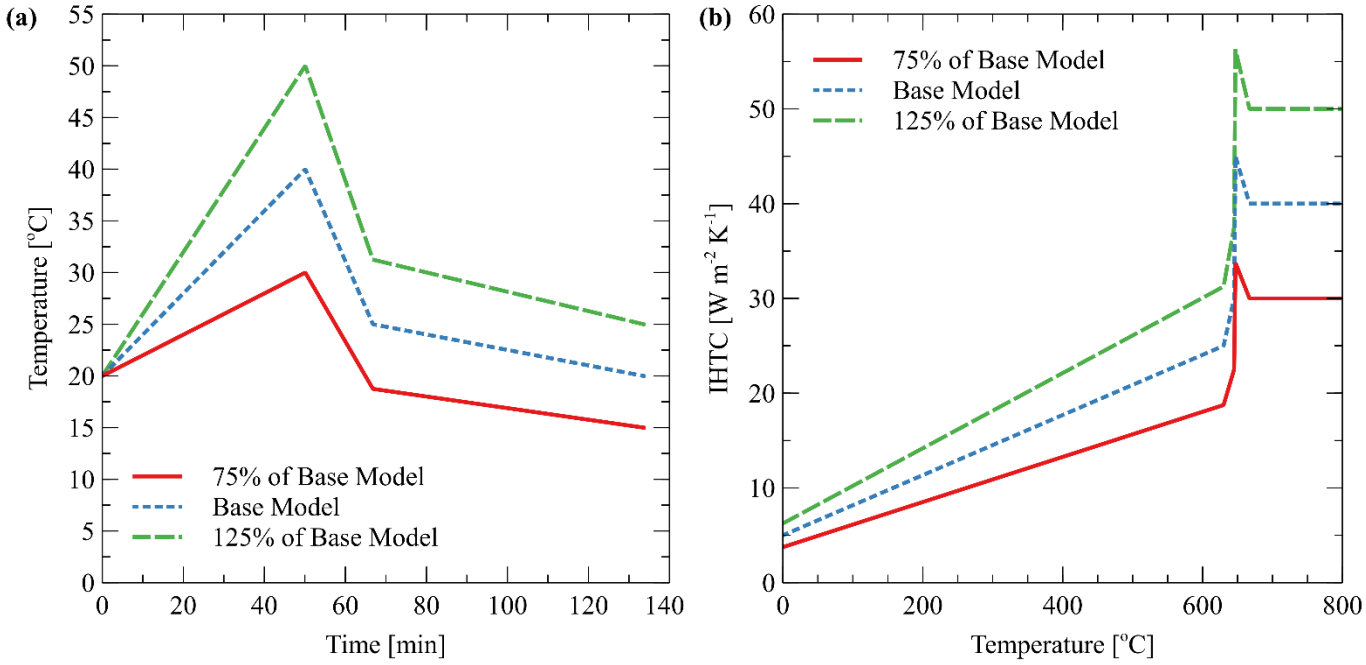

Figure G.2. Model input parameters used for sensitivity analysis; (a) the ambient temperature inside the EB-BF's vacuum chamber, and (b) the interfacial heat transfer coefficient at the CP-Ti disk/SS-plate interface.

Figures G.3 (a) and (b) show the relative change in the temperature distribution on the top surface of the CP-Ti disk along with line C-C' at the end of the heating and cooling cycles, respectively. The sensitivity analysis shows that the EB absorption factor (η) and the IHTC have the most impact on the temperature distribution on the top surface of CP-Ti disk during heating, as shown in Figure G.3 (a). In addition, changing the EB spreading – i.e., the standard deviation of the Gaussian function, changes the width of the beam pattern on the top surface of the CP-Ti disk resulting in a slight influence on the temperature distribution as expected. On the other hand, Figure G.3 (b) shows that the model is more sensitive to a change in the open cavity ambient temperature, the IHTC, and the EB-BF ambient temperature during cooling as the accumulated heat in the CP-Ti disk is transferred to the SS-plate and the heat shield.

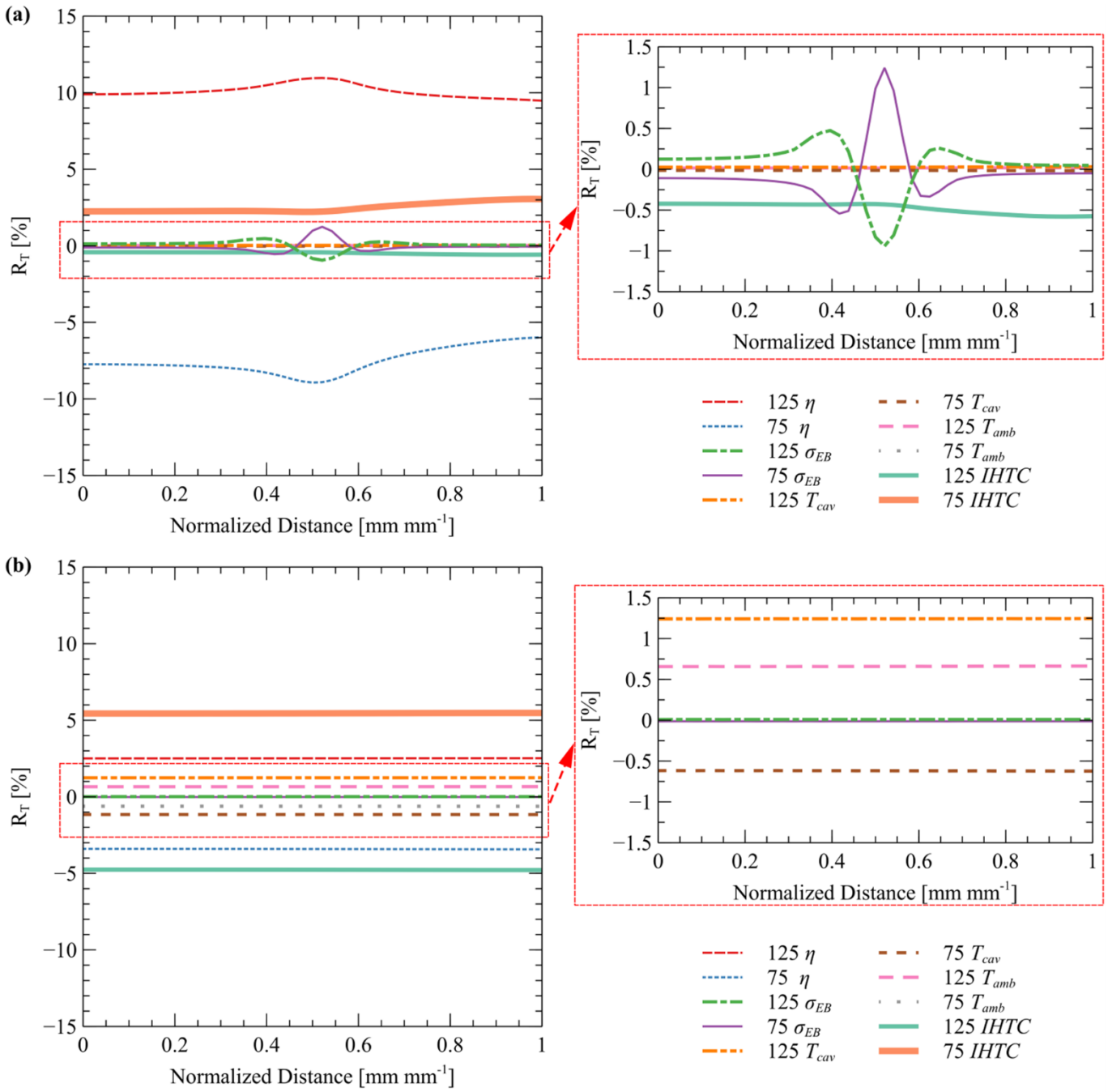

Figure G.3. The relative change in the temperature distribution on the top surface of the CP-Ti disk and line C-C' at the end of (a) the heating and (b) the cooling cycle.

Figures G.4 (a) and (b) show the relative change in the temperature distribution on the heat shield along lines A-A' and B-B', respectively, at the end of the heating cycles. The sensitivity analysis results show that the EB absorption factor (η), the IHTC, and the ambient temperature

inside the EB-BF vacuum chamber have the most impact on the temperature distribution on the heat shield during heating. This is due to thermal energy absorbed by the heat shield and the heat loss to the EB-BF vacuum chamber inner walls. In addition, changing the EB spreading and the open cavity ambient temperature resulted in a slight influence on the temperature distribution on the heat shield.

Note: the parameters that change the temperature distribution on the top surface of the CP-Ti disk directly influence the thermal radiation within the build environment cavity.

Figures G.4 (c) and (d) show that the model temperature predictions are more sensitive to a change in the open cavity ambient temperature and the EB-BF ambient temperature during cooling, as the radiative heat transfer is strongly dependent on the temperature difference.

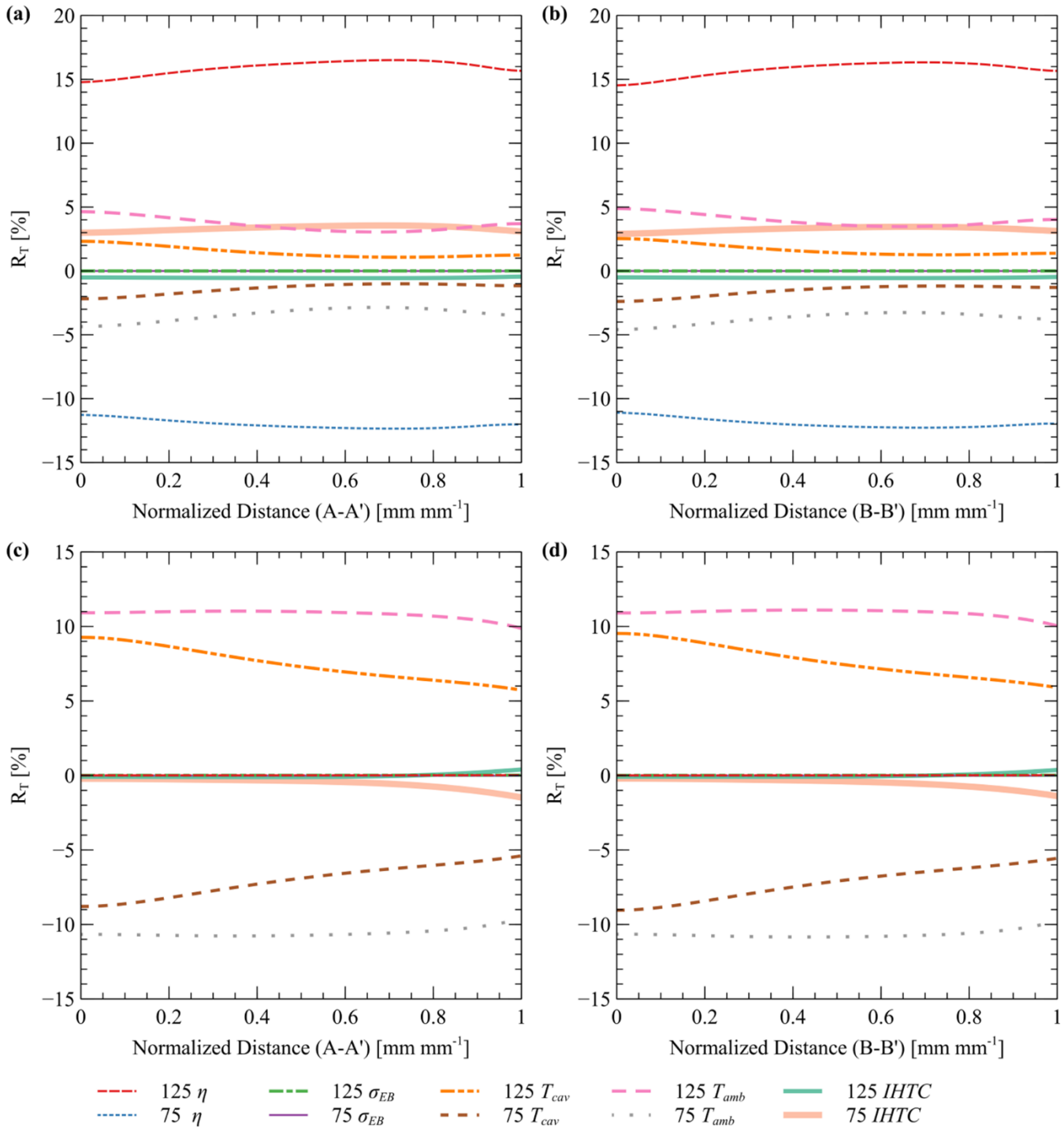

Figure G.4. The relative change in the temperature distribution on the heat shield at the end of the heating cycle along lines (a) A-A', and (b) B-B', and at the end of the cooling cycle along with line (c) A-A' and (d) B-B'.